Multiphysical dislocation dynamics models for high strain rate plastic deformation

by

Oxana Skiba

A thesis
presented to the University of Waterloo
in fulfillment of the
thesis requirement for the degree of
Doctor of Philosophy
in
Civil Engineering

Waterloo, Ontario, Canada, 2015

I hereby declare that I am the sole author of this thesis. This is a true copy of the thesis, including any required final revisions, as accepted by my examiners.

I understand that my thesis may be made electronically available to the public.

Abstract

Discrete Dislocation Dynamics (DD) models provide a framework to advance the understanding of plasticity. However, existing DD models currently do not account for multiphysical effects. Multiphysical phenomena are often present during plastic deformation. Two particular examples are the electromechanical behavior of plastically deformed piezoelectric materials and the thermomechanical behavior of metals under high strain rate plastic deformation. Thus, I present two new DD models, that take these behaviors into account.

The basic carriers of plastic deformation are dislocations, which are crystallographic defects. Therefore, in the two new DD models, dislocations are directly modeled as crystallographic line defects in an elastic continuum. These models are based on the Extended Finite Element Method (XFEM), which is a versatile tool used to analyze discontinuities, singularities, localized deformations, and complex geometries. The XFEM captures the slip from edge dislocations by way of Heaviside step enrichment function.

This paper starts with the first fully coupled two-dimensional electromechanical Discrete Dislocation Dynamics model (EM–XFEM–DD) for anisotropic piezoelectric crystalline solids undergoing plastic deformation. The strong, weak, and discrete forms of the boundary value problem for the coupled system are presented. The computation of the Peach–Koehler force, the force driving dislocation motion, using the J–integral is discussed. The EM–XFEM–DD model for a domain with a single edge dislocation was verified

by comparison with the solution obtained using the Finite Element Method (FEM) with Lagrange Multipliers. The piezoelectrical effect on the Peach-Koehler force on a single dislocation in a finite domain is evaluated. This effect is significant and can affect both the direction and magnitude of the force. The motion of a network of dislocations under different electrical and mechanical loads is simulated. The simulations demonstrate that for piezoelectric materials, the plastic response differs considerably when various electric potential differences are applied. In addition, the simulations illustrate that the physics of plasticity under electromechanical loads are more complex than in purely mechanical systems.

Next, the first fully coupled two–dimensional thermomechanical Discrete Dislocation Dynamics model (TM–XFEM–DD) is developed. Since high strain rate plastic deformation leads to significant temperature rises due to the rapid rate of heat generation by dislocation motion, each dislocation is considered as a moving heat source. The strength of each heat source is the work done by the Peach–Koehler force on each dislocation. The TM–XFEM–DD model also accounts for the temperature dependence of dislocation drag. Parametric studies show that the temperature dependence of dislocation drag does not significantly impact the observed stress-strain response at low loading rates, but it is significant at higher loading rates. The simulations using TM–XFEM–DD qualitatively capture the salient properties of high strain rate plastic deformation, such as the increased importance of thermal effects with increased strain rate. Higher temperature increase is observed in

specimens deformed at higher strain rates. In addition, the predicted stress–strain response of the TM–XFEM–DD model is softer than that predicted by a purely mechanical DD model. This softening effect is found to be stronger in the case of the adiabatic heating versus fixed temperature change on the boundary of the domain. Overall, the development of these two models that incorporate electro- and thermomechanical coupling will allow for a more accurate and comprehensive analysis of plastic deformation at the mesoscale.

Acknowledgements

I would like to express my special appreciation and thanks to my supervisors Dr. Robert Gracie and Dr. Stanislav Potapenko for their support and guidance over these years of Ph.D.. I am grateful to Dr. Robert Gracie for encouraging my research and for allowing me to grow as a research scientist. Without my supervisors this work would not be possible. I would like to express my gratitude to the members of the reading committee Dr. Liying Jiang, Dr. James Craig, Dr. Wayne Brodland and Dr. Kaan Inal for their patience in reading this manuscript and for the comments and suggestions they provided to improve it. I also thank them for letting my defense be an enjoyable moment.

I express the warm appreciation to my beloved husband Kris Nichols who was always my support in every moment. A special thanks to my family-in-law. Your prayers for me were very appreciated. I would also like to thank all of my friends who have become family to me.

And last but not least, I would like to thank my parents Yakov and Yelena Skiba for their unconditional love and help they have surrounded me with.

Dedication

To my parents.

Table of Contents

List of Tables

List of Figures

Nomenclature

α	dislocation
$\bar{N}_I$	standard finite element shape functions for electric potential
$\boldsymbol{\epsilon}$	dielectric tensor
$\boldsymbol{\sigma}$	Cauchy stress
$\boldsymbol{\varepsilon}$	strain
$\boldsymbol{\gamma}$	tensor of the coefficients of thermal expansion
$\boldsymbol{\phi}_I$	nodal electric potentials
Γ	boundary of the domain Ω
Γ_c^α	any closed contour about the dislocation α
$\hat{q}$	surface charge
Λ	Lagrangian

ρ body charge density

φ electrical potential

$\mathbf{B}$ tensor of the dislocation drag, or the inverse of the dislocation mobility tensor

$\mathbf{b}^{\alpha}$ Burgers vector of dislocation α

$\mathbf{C}$ tensor of the elastic moduli

$\mathbf{D}$ electric displacement

$\mathbf{d}_I$ nodal displacement degrees of freedom

$\mathbf{E}$ electric field

$\mathbf{e}$ piezoelectric tensor

$\mathbf{F}^{\alpha}$ Peach–Koehler force

$\mathbf{H}^{m}$ Sobolev space

$\mathbf{k}$ tensor of the coefficients of thermal conductivity

$\mathbf{q}$ heat flux density

$\mathbf{t}$ surface traction

$\mathbf{u}$ displacement

$\mathbf{v}^{\alpha}$ velocity of the dislocation α

$\mathbf{x}^{\alpha}_{cur}$ position of the dislocation α at the current moment

$\mathbf{x}^{\alpha}_{next}$ next position of the dislocation α

ν Poisson's ratio

Ω domain

ρ mass density

ρ_{obs} obstacles density

ρ_{src} Frank–Read source density

τ_{nuc},τ^{FR}_{nuc} nucleation strength

τ_{obs} strength of the obstacle

$\mathbf{g}$ body force

Θ absolute temperature change from the stress free reference temperature

Θ_0 stress free reference temperature

$\Theta_I(t)$ nodal temperature change

B^{α} drag coefficient of dislocation α

C_p specific heat capacity

dt the increment in time

E Young's modulus

F_k Peach–Koehler force k component

F_{obs} pinning force of the obstacle

G functional of constraints

h heat flux

h_e element size

L_2 Lebesgue space

L_{an} annihilation distance

L_{nuc}, L_{nuc}^{FR} diameter of the dislocation loop

n_d number of dislocations

N_I, N_I^u standard finite element shape functions for displacement

S set of all mesh nodes

$S(\mathbf{x}, t)$ body heat source

S^α set of enriched nodes

$s_\alpha(t)$ heat generated by the motion of dislocation α

t time

T_0 initial change in temperature

t_{nuc} time to form a dislocation loop

N_I^{Θ} standard finite element shape functions for temperature change

Chapter 1

Introduction

Investigating different material properties for the purposes of improving their use is one of the continuing goals of material science and engineering. Thus, it is advantageous to predict and control, as accurately as possible, material behavior. Material properties arise from phenomena that occur at different spatial and temporal scales, and understanding these materials' behaviors can be achieved by modeling them at different scales, see Fig. 1.1. This figure illustrates the spacial and temporal boundaries for different modeling methods that are used to analyze materials. In addition, the interactions of those scale intrinsic phenomena should be taken into consideration when modeling material behaviors in order to accurately predict their responses. The findings, concepts, and techniques associated with each scale (atomic, dislocation, micro, and marco) can be studied in unison to generate a more comprehensive understanding of material behaviors.

Orowan highlights the difficulty of modeling materials with imprecise models or improper scaling [1]:*"The macroscopic behavior we observe is built up of the intricate, com-*

plex interactions between mechanisms operating on a wide range of length and time scales. Studying a material from only the largest of scales is like studying a pocket watch with only a hammer; neither method will likely show us why things behave as they do. Instead, we need to approach the problem from variety of observational and modeling perspectives and scales [2].”

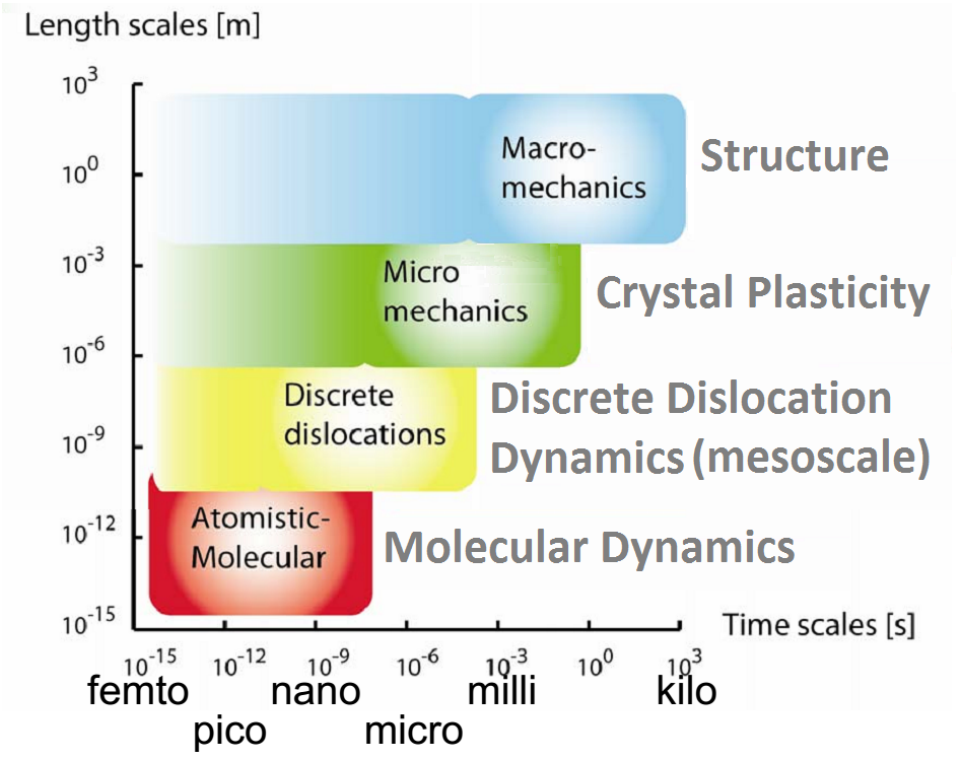

Figure 1.1: Multiscale modeling. Modified from [3].

Even though plastic deformation of crystalline solids has received considerable attention, especially in small structures, there is still significant work that needs to be done in terms of developing more precise models. When Erik van der Giessen outlined the theory

of plasticity in 21st century, dislocations were identified as the basic carrier of plastic deformation [4]. Discrete dislocation dynamics provides a framework for developing models that directly simulate the motion and interactions of dislocations at the mesoscale, the length scale between crystal plasticity models and molecular dynamics models. Developing models at the mesoscale opens up several new possibilities [5]: first, the simulations of dislocation dynamics bridge the fundamental nature of the microstructure with realistic material deformation and failure by providing quantitative input for phenomenological constitutive rules in crystal plasticity. Second, and perhaps more importantly, is that such simulations are expected to become a major tool in the analysis of plasticity problems at the scale of micron and less. Analyzing plasticity problems at such a scale is increasingly important as we see the ongoing progress of component miniaturization in this century [4]. Furthermore, multiphysical phenomena are often present during plastic deformation. Such phenomena involve multiple simultaneous physical processes, see Fig. 1.2, which should be accounted for when modeling plastic material behavior. Therefore, developing methods to model dislocation dynamics contributes significantly to the field of plasticity.

My thesis focuses on improving two main areas within existing discrete dislocation models. The rationale being that existing models do not account for multiphysical effects, and therefore, do not accurately bridge the gap between molecular dynamics and crystal plasticity. The benefit of bridging this gap is that it provides a more accurate representation of materials at the mesoscale.

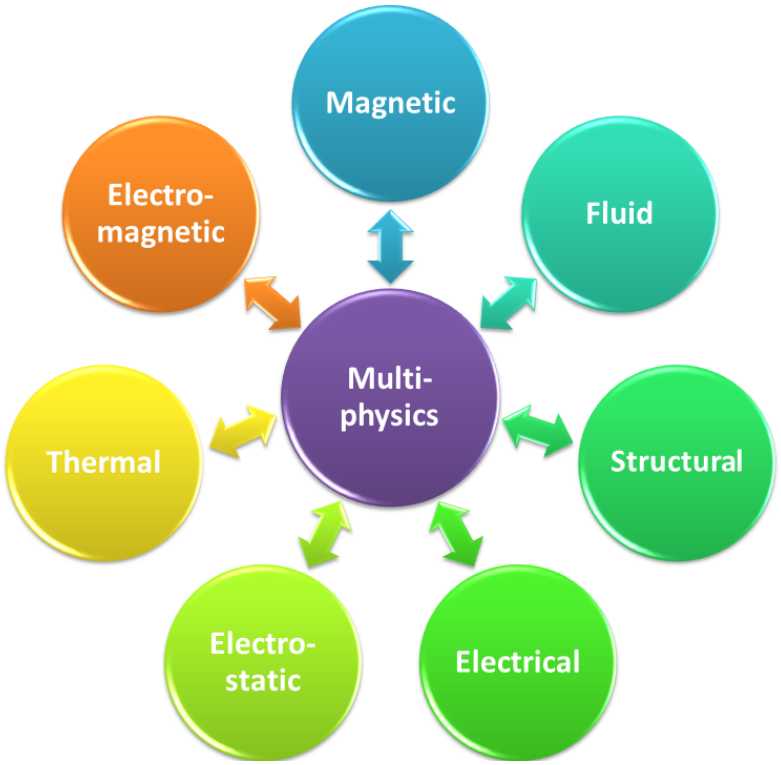

Figure 1.2: Physical phenomena of a Multiphysics model.

The first contribution lies in modeling the plastic piezoelectric material behavior at the dislocation level. Due to the characteristic multiphysical effects that take place between electric and mechanical fields, piezoelectric materials play a key role in the development of micro-electro-mechanical systems (MEMS): the technology of very small devices. It has been observed that dislocations degrade the performance of electronic devices, including components used in MEMS [6]. The deformations and electrical fields produced by dislocations affect the conductivity and other electrical properties of materials, causing them to degrade [7]. Current discrete dislocation dynamics models do not incorporate electrome-

chanical effects when modeling plastic behavior of piezoelectric materials, and thus, I have constructed a model that includes electromechanical effects.

The second contribution lies in the accurate modeling of high strain rate plastic deformation of crystalline solids. High strain rate plastic deformation is known to cause significant local temperature rise and thermal softening [8], due to the fact that a large number of dislocations generate a significant amount of heat when they move under high strain rates deformation. It is not uncommon to observe temperatures rise more than 800 K in shear bands during localization [9, 10]. Empirical continuum plasticity models (e.g., Johnson-Cook [11]) often incorporate softening terms into the flow stress definition based on the assumption of adiabatic heating. Crystal plasticity models with thermal softening have also been developed on the basis of adiabatic heating [10]. It is important for high strain plasticity models to incorporate thermal softening in some way. At the nanoscale, molecular dynamics simulations inherently incorporate thermomechanical coupling by explicitly modeling the lattice vibrations and the motion of individual atoms. However, unlike models at both larger and smaller length scales, current discrete dislocation dynamics models do not incorporate thermomechanical effects of high strain rate plastic deformations.

Therefore, the goal of this research project is to bridge the gap between two scales, molecular dynamics and crystal plasticity, incorporating the effect of multiphysics during plastic deformation of piezoelectric materials and high strain rate plastic deformation of

any crystalline solids. Bridging the gap between the two scales is achieved by means of the discrete dislocation dynamics framework. Two new discrete dislocation dynamics model variants are developed based on eXtended Finite Element Method. The models are implemented in Matlab. One is the first fully coupled electromechanical discrete dislocation dynamics model for plastic deformation of anisotropic piezoelectric crystalline solids. The second one is the first fully coupled thermomechanical discrete dislocation dynamics model for high strain rate crystalline solids plastic deformation. Thus, the main objectives of the current research for the first model are:

- Develop the strong, weak, and discrete forms of the boundary value problem for the coupled electromechanical system in the presence of dislocations.
- Solve the coupled electromechanical boundary value problem using eXtended Finite Element method.
- Take the electromechanical effect into account when calculating the driving force on each dislocation in a piezoelectric media.
- Simulate the nucleation and motion of a network of the dislocations using the developed fully coupled electromechanical dislocation dynamics model.
- Study the effect of electromechanical coupling on plastic deformation of anisotropic piezoelectric crystalline solids.

The main objectives of the current research for the second model are:

- Develop the strong, weak, and discrete forms of the boundary value problem for the coupled thermomechanical system in the presence of dislocations.
- Solve the coupled thermomechanical system using eXtended Finite Element method.
- Take the thermal effects into account when calculating the driving force on each dislocation, heat generated by dislocation motion under the high strain rate plastic deformation, and temperature dependence of dislocation drag.
- Simulate the nucleation and motion of a network of the dislocations using the developed coupled thermomechanical dislocation dynamics model.
- Study the effect of thermomechanical coupling on high strain rate plastic deformation of crystalline solids.

The thesis has the following structure: in Chapter 2, the basic elements of dislocation theory are explained, which includes discussion of two types of dislocations, different mechanisms of dislocation motion and nucleation, and driving force on a dislocation. Then the literature review of the methods to describe a dislocation is given. After that, the main classes of discrete dislocation dynamics models with their major advantages and difficulties are reviewed. Particular attention is given to the eXtended Finite Element Method, since this is the method used in the two new discrete dislocation dynamics models proposed within this current work. The unique properties of piezoelectric materials and the effect of dislocations on electric field in such materials are discussed in the following section. The

chapter ends with a description of thermal effects due to dislocation motion under high strain rate deformation.

In Chapter 3, the first fully coupled electromechanical discrete dislocation dynamics model, based on the eXtended Finite Element Method, is developed for plastic deformation of anisotropic piezoelectric crystalline solids. Derivation of the theoretical formulation, including strong, weak, and discrete form of the coupled electromechanical system is presented. Then, verification of the model is presented, for a single edge dislocation in the middle of a domain, by comparing it with the solution obtained using Finite Element Method with Lagrange multipliers. The verification of the numerical calculation for Peach–Koehler force on a dislocation, using J–integral, is presented in the following section. After that, the phenomenological rules for the dislocation dynamics are presented. The Chapter ends with a numerical example, that illustrates the motion of many edge dislocations in a small anisotropic piezoelectric domain under mechanical and electrical loads and demonstrates the effects of electromechanical coupling on material behavior.

In Chapter 4, the first fully coupled thermomechanical discrete dislocation dynamics model, based on the eXtended Finite Element Method, is developed for high strain rate plastic deformation of crystalline solids. Derivation of the theoretical formulation, including strong, weak, and discrete form of the coupled thermomechanical system is presented. Then, the time integration scheme is discussed. Different thermal effects associated with dislocation dynamics, such as calculation of the heat generated by dislocations motion,

a Peach–Koehler force calculation in the presence of thermal field, and dislocation drag temperature dependency are described in the following section. Lastly, the simulation results and parametric studies are used to demonstrate the effects of boundary conditions, dislocation drag, and loading rate.

Finally, conclusions and recommendation for future work are presented in Chapter 5 and Chapter 6 respectively.

Chapter 2

Literature Review

This chapter provides an overview of dislocation modeling. I will start with a brief introduction to the basic concept of dislocation theory, followed by an in-depth exploration of those theories used in this work. After which, I will provide an overview of current dislocation modeling methods. Next, the strength and limitations of various discrete dislocation dynamics models are presented. The eXtended Finite Element Method, used to model the discrete dislocation dynamics, is presented in greater detail, since this is the preferred method used in this work, due to it's ability to model dislocations dynamics without having to refine or reconstruct the finite element mesh. In addition, this chapter provides a literature review on modeling the plastic deformation of the piezoelectric materials at the mesoscale, the length scale between crystal plasticity models and molecular dynamics models. Lastly, I will explain the thermal effects of dislocation motion under high strain rate deformation in order to show the importance of including these thermal effects when modeling the plastic behavior of material at the mesoscale. This chapter provides an overview

of the modeling of dislocations. It starts with a brief introduction to the basic concept of dislocation theory with an emphasis on those used in the current work. Then, an overview of current dislocation modeling methods is presented. Next, the strength and limitations of various discrete dislocation dynamics models are presented. The eXtended Finite Element Method to model the discrete dislocation dynamics is presented in greater detail, since this is the preferred method used in this work. In addition, the chapter provides a literature review on modeling the plastic deformation of the piezoelectric materials at the mesoscale. Lastly, the explanations of thermal effects due to dislocation motion under high strain rate deformation are presented.

2.1 Elements of dislocation theory

Dislocations are crucial in determining the mechanical behavior and properties of crystalline solids. A crystalline solid (crystal) is a solid material whose elements, such as atoms, molecules or ions, are arranged in a highly ordered microscopic structure, forming a crystal lattice that extends in all directions [12]. Most metals are polycrystals, i.e. a blend of microscopic crystals. An ideal crystal has every atom in a perfect and exact repeating pattern. However, in reality, most crystals are not perfect and have crystallographic defects. The lattice dislocations are one of these crystallographic defects. In 1934, Taylor[13], Polanyi[14] and Orowan[15, 16, 17]presented independent papers, exposing lattice dislocation (or just dislocation) as the crystallographic unit responsible for the plastic

deformation of crystalline solids. Since this discovery, it has been a key goal of materials research to understand the role dislocation nucleation and dynamics have in understanding the plastic behavior and strength of crystalline solids [18]. Without such an understanding, the design and optimization of new metals with tailored properties is is extremely limited [19, 20]. Detailed description of the dislocations and their properties can be found in many introductory books, for example, [21, 22, 23, 24]. However, I will discuss only the most relevant concepts related to my thesis.

2.1.1 Types of dislocations and Burgers vector

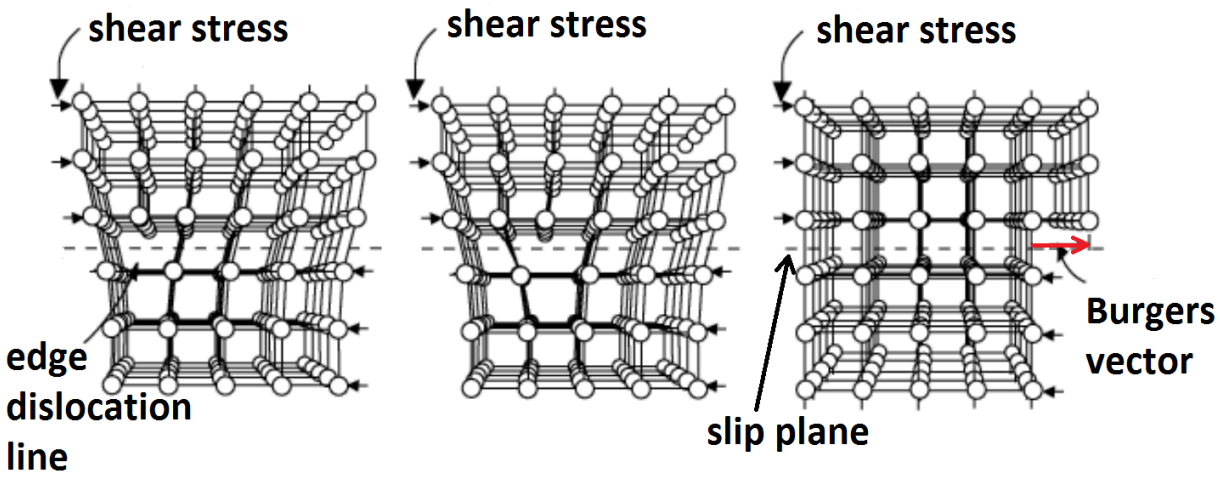

Figure 2.1: An edge dislocation in a single crystal. Modified from [19].

The illustration of an edge dislocation in a single crystal is given in Fig.2.1. The location of the dislocation core is where the distortion of the perfect lattice is the greatest, see Fig.2.2. A screw dislocation is more complex and is demonstrated in Fig.2.3. A

dislocation can be seen as a line discontinuity in the crystal structure. An edge dislocation is an the insertion (or removal) of an extra half plane of atoms in the crystal structure. Whereas, a screw dislocation changes the character of the atom planes. The atoms form a surface that spirals from one end to the other end of the crystal[19].

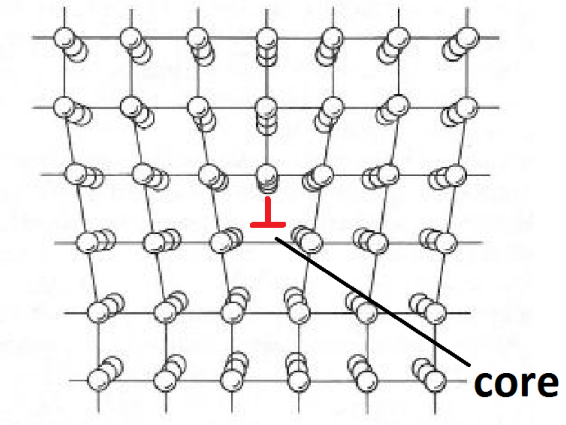

Figure 2.2: The core region of an edge dislocation in a single crystal. [19].

Burgers vector is used to characterize a dislocation. It represents the magnitude and direction of a lattice distortion, see Fig.2.1 for an edge dislocation and Fig.2.3 for a screw dislocation. In order to help provide a visual example, consider a circuit A-B around an edge dislocation, see the left side of the Fig.2.4. If we put a circuit with the same atom-to-atom sequence in a perfect crystal, the starting point A and the ending point B are not the same atom, see the right side of the Fig.2.4. The vector needed to close this circuit is the Burgers vector of this dislocation. The Burgers vector is usually labeled with **b**. The direction of the Burgers vector depends on the slip plane of dislocation, which will be

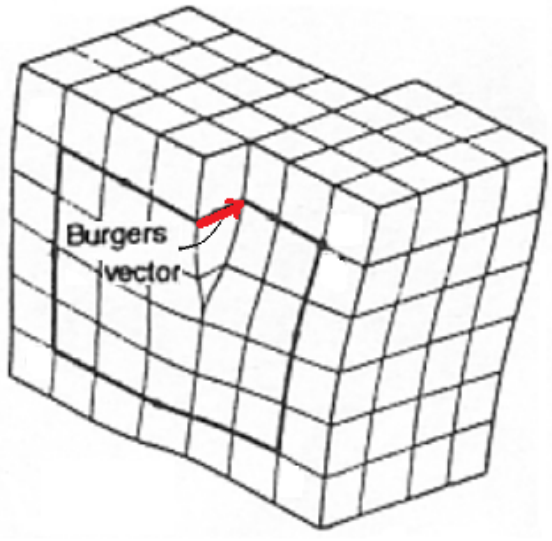

Figure 2.3: A screw dislocation in a single crystal [19].

defined in the next section.

2.1.2 Dislocation movements

Dislocation motion along a crystallographic direction is called glide. When a dislocation moves, or glide, the individual atoms slip in the direction parallel to the Burgers vector; the dislocation itself moves in a direction perpendicular to the dislocation line in the slip plane. Therefore, the glide occurs in the direction of the Burgers vector for the edge dislocation; whereas the glide is perpendicular to the Burgers vector for the screw dislocation. Yet, the total plastic deformation of both edge and screw dislocations is the same, see Fig 2.6. In order to visualize how glide occurs see the Fig:2.5.

The consequence of the glide of many dislocations is a slip, which is the manifestation

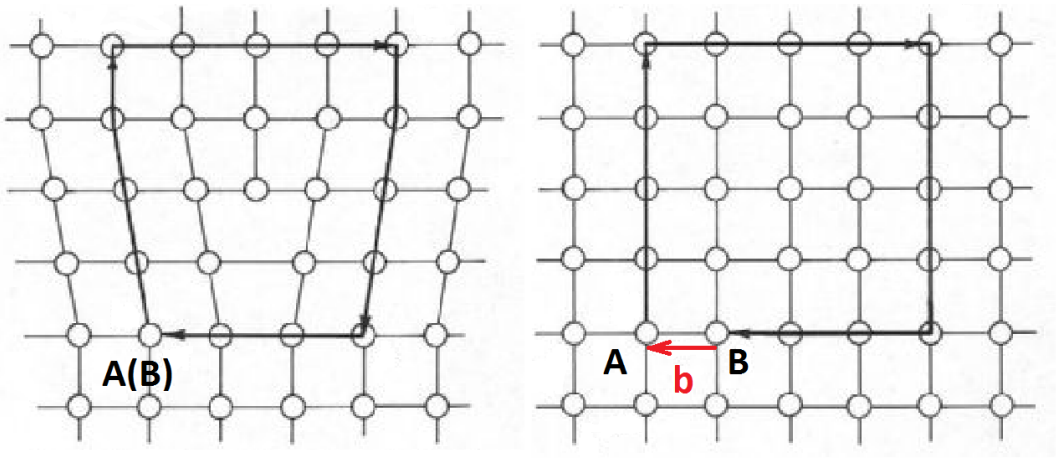

Figure 2.4: A circuit around an edge dislocation [22]. Left: The circuit with matched starting point A and the ending point B. Right: The circuit with mismatched starting point A and the ending point B.

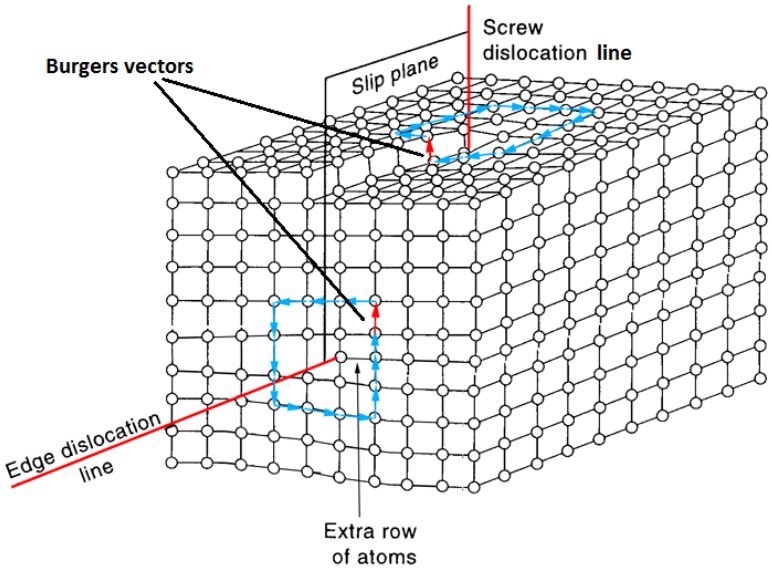

Figure 2.5: Edge and screw dislocations lines. Dislocation slip plane. Burgers vectors. Modified from [25]

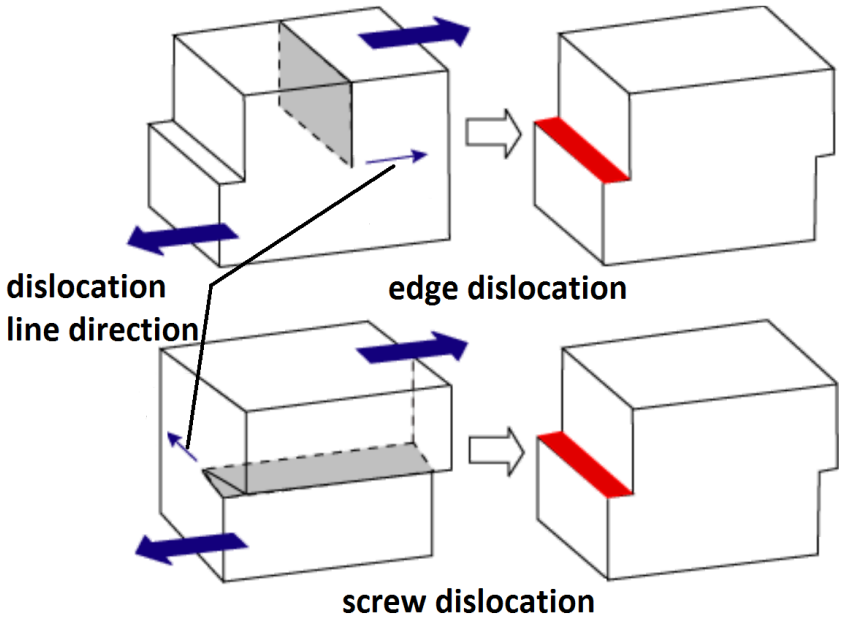

Figure 2.6: An edge and screw dislocations glide. Modified from[22].

of the plastic deformation in crystalline solids. Under loading conditions, dislocations move more easily on specific slip planes that have the most dense atomic packing (the greatest planar density). The slip occurs in the specific directions that are most closely packed with atoms (highest linear density). The combination of slip plane and slip direction is called the slip system. Different crystal structures have different sets of slip systems. For example, in Fig:2.7, one of the preferred slip planes and three slip directions on it are schematically shown for the face centered cubic (FCC) crystal. This crystal has four slip planes with three directions in each, which gives twelve slip systems.

Dislocation glide allows plastic deformation to occur at a much lower stress than would be required to move an entire plane of atoms past another [27]. Calculations confirm the

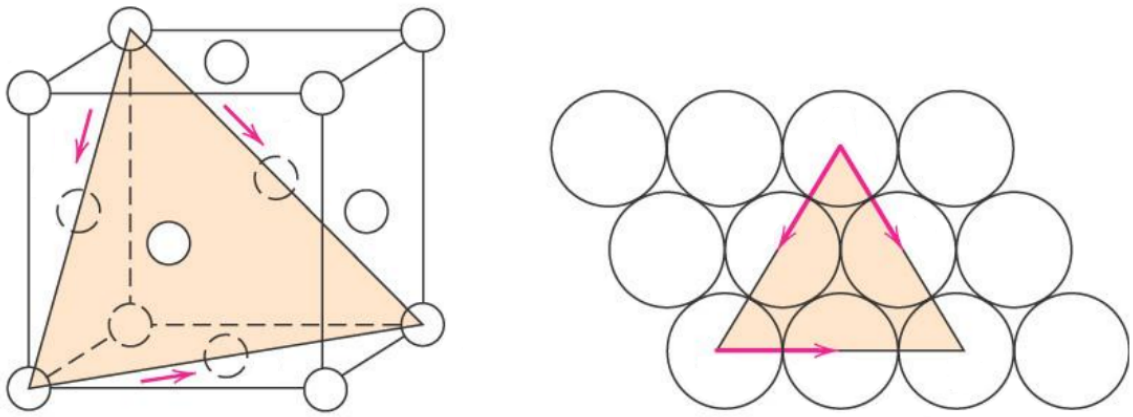

Figure 2.7: Left: slip plane–most dense atomic packing. Right: Slip directions (pink arrows)–highest density of atoms. Modified from [26]

fact that slip is the result of dislocation motion [24]. This enhances the need to study in depth the mechanism of the dislocation motion and its effect of plastic deformation.

It is observed experimentally that slip occurs when resolved the shear stress, τ, acting in the slip direction on the slip plane, reaches some critical value, the critical resolved shear stress, τ_{cr}. This critical shear stress represents the stress required to move dislocations across the slip plane and is a property of the material that determines when yielding occurs. To visually relate the tensile stress, σ, applied to a sample to the resolved shear stress, see the Fig:2.8. The resolved shear stress on the slip plane parallel to the slip direction is therefore given by:

$$\tau = \frac{F}{A} \cos\phi \cos\lambda \tag{2.1}$$

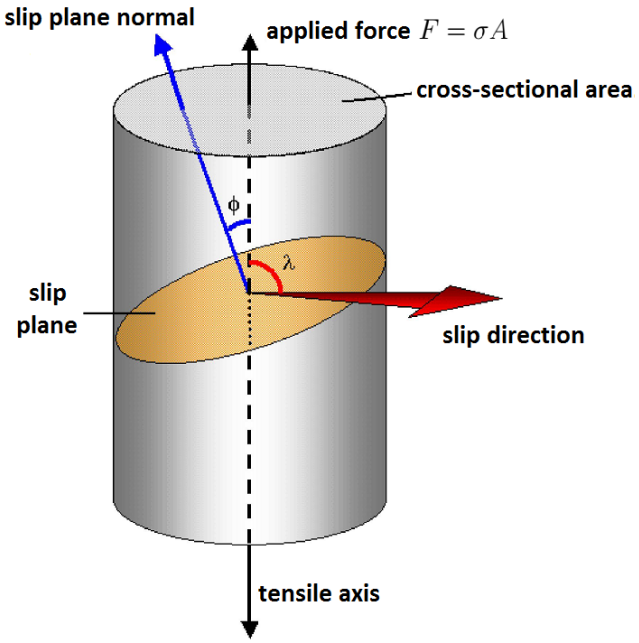

Figure 2.8: Illustration of the geometry of slip. Modified from [22]

where F is the applied force, A is the cross–sectional area, ϕ is the angle between F and the normal to the slip plane, and λ is the angle between F and the slip direction. The Eq.(2.1) is known as the Schmid's law and the quantity $\cos\phi\cos\lambda$ is known as the Schmid factor.

Even though I will not be analyzing this mechanism, it is still pertinent to note that there is an alternative mechanism for dislocation glide that allows the dislocations to move out of their current slip plane. For an edge dislocation this process is called climb, and it is controlled by core diffusion. Dislocation climb allows an edge dislocation to move

perpendicular to its slip plane. Schematically, the climb is shown in Fig:2.9. Due to the fact that deformation process is very fast compared to diffusion, the dislocation climb is neglected in this work. Although dislocation climb is a notable element of dislocation behavior, future research should be completed to also include such a mechanism.

Figure 2.9: Schematic illustration of the dislocation climb. Modified from [28].

2.1.3 Frank–Read source

There are different mechanisms of dislocation generation [19]. However, at present it is not possible to determine which one is more important. Moreover, several mechanisms might operate at the same time. In my thesis, a Frank-Read source is assumed to be the predominant mechanism of dislocation generation [29]. As was described in the previous section, when the shear stress reaches some critical value τ_{cr}, the dislocations glide on specific planes. Thus, the dislocations source must be activated at this τ_{cr} and in those specific planes.

Consider an initial straight dislocation segment of a Frank–Read source in an arbitrary

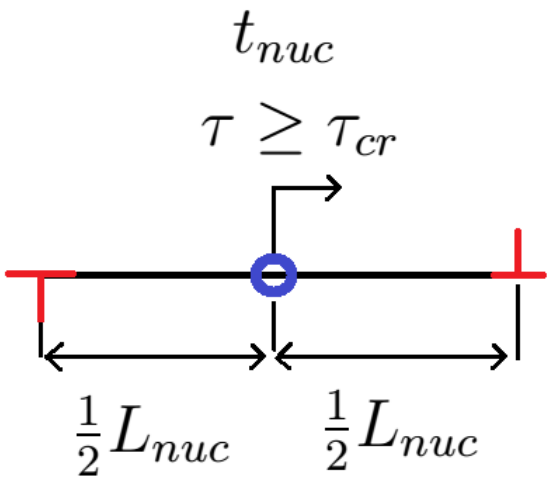

Figure 2.10: A two–dimensional Frank-Read source.

slip plane. With increasing resolved shear stress, τ, the segment of a Frank–Read source bends out until a critical Frank–Read arrangement is formed and leaves behind a duplicate of itself. Thus, the Frank–Read source is defined by a critical resolved shear stress for activation of the mechanism, or nucleation strength, $\tau_{cr} = \tau_{nuc}$, the time to form a critical configuration, t_{nuc}, and the diameter of the generated dislocation loop L_{nuc}, which is a distance between dislocations of the dipole. The two–dimensional Frank–Read source mechanism is displayed in Fig. 2.10 similar to [5]. The dipole consists of two opposite dislocations with the same magnitude, but in opposite directions of the Burgers vector, which is determined by the direction of τ. The distance between two dislocations, L_{nuc}, is taken to be such that the attractive force is balanced by the internal stress.

The values of the nucleation strength, the time to form a critical configuration, and the diameter of the generated dislocation loop depend on the length of initial straight dislocation segment of a Frank–read source, the elastic properties, and the drag coefficient [5]. Dislocation drag is a material property and is related to the interaction between dislocations and lattice vibration. The fact that this parameter is temperature dependent is often neglected when modeling the dislocations dynamics, see Sec.2.5. In this work, a model that accounts for such temperature dependency is developed and described in Ch.4.

2.1.4 Peach–Koehler force

The driving force for dislocation motion is Peach–Koehler force. This force is one of the key aspects when modeling the motion of the dislocations, which is why it is introduced in more detail below.

In 1950 Peach and Koehler developed a general equation for such force, $\mathbf{F}^{\alpha}$, per unit length of a dislocation line and its unit tangent vector is $\boldsymbol{\xi}^{\alpha}$:

$$\mathbf{F}^{\alpha} = \boldsymbol{\xi}^{\alpha} \times (\hat{\boldsymbol{\sigma}} \cdot \mathbf{b}^{\alpha}) \tag{2.2}$$

where $\hat{\boldsymbol{\sigma}}$ is the stress on a dislocation α from all sources, such as surface traction, other dislocations, or any other strain-producing defects except the self-stress of dislocation α. $\mathbf{b}^{\alpha}$ is the Burgers vector of the dislocation [30].

By nature the Peach–Koehler force can be classified as a configurational, or material, force. According to Maugin [31], material forces are generated by a displacement on the

material manifold. In other words, it is generated by a infinitesimal displacement of a dislocation line. The material manifold is the group of material points that build up the body. Thus, material forces may act on an empty set of that group, e.g. singularities, such as dislocations. The material forces can be computed once the standard field equations are solved.

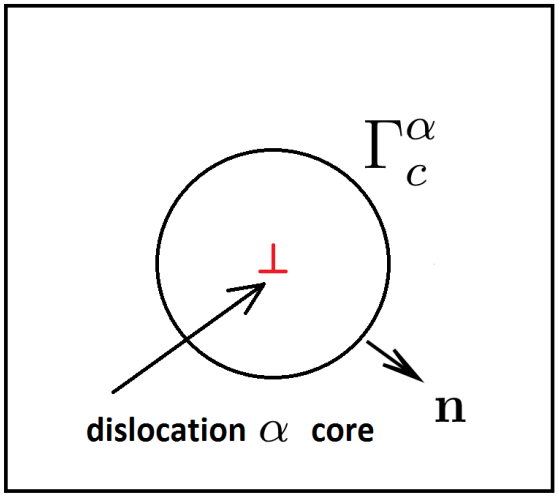

Figure 2.11: Conventions for the calculation of the Peach–Koehler force on a dislocation α using the J–integral

In 1951 Eshelby introduced the force acting on elastic singularities by examining the energies of the system [32]. The singularity in mathematical sense is the point where internal stress is infinite and the derivative of the stress is not defined. The force on a singularity can be calculated by an integral over a surface enclosed in a simple curve. Therefore, the Peach–Koehler force driving the dislocation can be also computed by such

an integral, as an alternative to Eq.(2.2). For the linear case, as proposed by Eshelby, the Peach–Koehler force is

$$F_k = \oint_{\Gamma_c^\alpha} [\frac{1}{2}\sigma_{ij}\varepsilon_{ij}\delta_{lk} - u_{i,l}^{\top}\sigma_{ik}]n_l d\Gamma_c^\alpha \tag{2.3}$$

where Γ_c^α is any closed contour about the dislocation α, $\mathbf{n}$ is the unit outward normal to Γ_c^α, see Fig.2.11; σ_{ij}, ε_{ij}, and $u_{i,l}$ are the components of stress, strain, and displacement respectively. This integral Eq.(2.3) is known as path-independent J-integral in fracture mechanics [33], [34] and is viewed as a configurational force acting on a defect.

2.2 Modeling dislocations

The first model for defects, in general, was proposed by Volterra in 1907 as a mathematical thought experiment [35]. Volterra defined all possible basic deformation cases of a continuum (including crystals) before the concept of crystal defects was ever conceived. In the Volterra model, a cut is made in an elastic solid; two surfaces separated by the cut are moved relative to each other by Burgers vector, permitting elastic deformation of the lattice in the region around the dislocation line. The material is then restored by welding together the cut surfaces. The Volterra model for edge dislocation is illustrated in Fig. 2.12, mainly because this dislocation type is of great interest for the purposes of this paper.

Such a dislocation model is based on the theory of elasticity [21, 19, 23, 36]. Here a dislocation is presented as a line in a continuous medium, while the details of the atomic

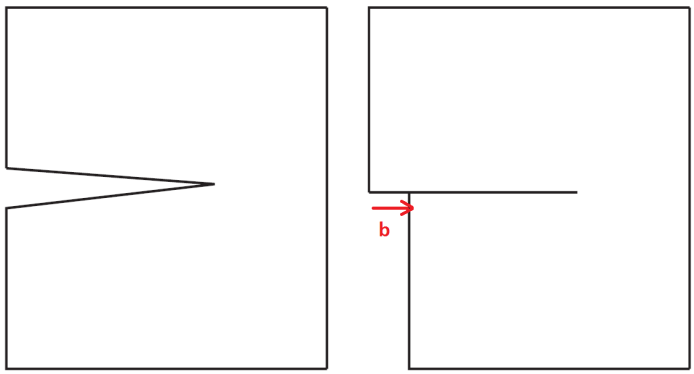

Figure 2.12: Volterra model for a edge dislocation.

structure are overlooked. The strain and stress fields are sufficiently described by the continuum dislocation theory when the dislocation core is more than a few Burgers vectors lengths away. Otherwise, these fields become singular at the core, because the dislocation core is a small region, where the atomic structure is greatly distorted. The elastic energy density diverges at the dislocation itself due to the incompatibility created at the core by continuum theory. Inside the dislocation core, the crystal structure can be best described by atomically informed models [37, 38, 39].In the case of atomically informed models, the main interest switches to discovering properties associated with the core, as opposed to the continuum models. Such properties and their impact on dislocation motion, and thus on plastic deformation, can be adequately understood when the atomic structure is sufficiently accounted for.

Together, the information from atomically informed models can be incorporated into continuum models to improve one another. Such models are called hybrid models [22, 19];

the most well known one being Peierls–Nabarro model [40, 41]. This model incorporates atomic effects into the continuum model, which provides a way to understand the core structure and the dislocation drag. The latter of these two plays an important role when modeling the dislocation dynamics, as will be shown in Ch.4. Peierls [41] obtained a way to determine the critical resolved shear stress, which is an essential parameter in dislocation dynamics modeling. Many other efforts have been made to improve and generalize Peierls–Nabarro model by including more atomic information [38, 42, 43, 44, 45, 46, 47, 48, 49]. Modifications to use the anisotropic elasticity rather than the isotropic one have been also made in [50, 51, 52].

Overall, the atomic and hybrid models bring significant insights into modeling the dislocations in an elastic continuum. In this thesis, continuum models were developed for dislocations based on a discrete dislocation dynamics approach and with a minimal amount of direct atomic input.

2.3 Discrete Dislocation Dynamics (DD)

Much of the current literature on plastic deformation pays particular attention to Discrete Dislocation Dynamics [53, 54, 5, 55, 56, 37]. Discrete Dislocation Dynamics is known as the direct simulation of interactions between and motion of individual dislocations within an elastic continuum. Such simulations average out the atomistic nature of the material and offer insights into crystal plasticity [57, 58] by reproducing the physics of plastic de-

formation at the mesoscale. In Discrete Dislocation Dynamics, the evolution of dislocation configurations takes place through discrete steps: one, the sequence of equilibrium solutions is obtained with evolving dislocations, two, the total stress of the domain is calculated for a given distribution, number and geometry of the dislocations at each step. In order to determine the distribution, number and geometry of the dislocations for the next step in DD, it is necessary to establish the variety of different mechanisms that govern dislocation nucleation, interaction and evolution. The phenomenological equation of motion for each dislocation determines the exact velocity, and therefore, the position of the dislocation for the next step.

Discrete Dislocation Dynamics methods provide an important opportunity to advance the understanding of material plasticity and failure. Modeling material behavior for a large number of dislocations is a computationally intensive task, and it is still in a state of continued improvement due to the ongoing evolution of efficient computational methods and computer technologies. Nevertheless, several dislocation dynamics methods have been developed. Currently, the simulations can be carried out in a system containing a relatively large number of dislocations and one in which the size is of the order of ten microns [59]. The challenges in dislocation dynamics arise from the fact that different physical process are associated with the evolution of dislocation structures. First, the motion and interaction of dislocations depend on long–range interactions between dislocations. These interactions are very complicated and depend on the positions of all dislocation ensembles relative

to each other, as well as the directions of their Burgers vectors. Second, the short–range interactions of dislocations - such as the dislocation nucleation, climb, and annihilation that have an atomic scale nature - have an essential role in the behavior of a dislocation network. As a result, accurate analytical descriptions, the development of numerical approximations, in addition to rules for the analysis of long- and short-range interactions are all pivotal for overcoming the difficulties and advancement of dislocation dynamics modeling. Currently, several dislocation dynamics methods are developed accounting for complicated geometries of the dislocations and simulating the motion and interactions of many dislocations [60, 61, 62, 63, 64, 65].

The existing models for dislocation dynamics can be categorized into three classes: smeared models, models based on superposition, and the eXtended Finite Element Method (XFEM).

2.3.1 Smeared models

This class of dislocation dynamics models can be called smeared models. The smeared model class includes the models based on a phase field description of dislocations, as proposed by Khachaturyan, Wang and co–workers [66]. Phase field methods directly model the dislocation field, but represent the discontinuities of the dislocations by smearing (i.e., regularization). There is no need to track the evolution of dislocation lines and their topology, since the dislocations only appear as a result of post-processing the continuously

evolving phase-fields. The modeling of the dislocations is possible in three dimensions. However, a rather coarse mesh is employed. The elastic interactions of the dislocations are determined using well-established fast Fourier transform methods. In addition, anisotropic crystals can be modeled without considerable loss of computational efficiency. However, in this model the total energy of a dislocation system contains a term not normally present in dislocation theory, but must be included within the phase field model to prevent the dislocation core from expanding. Another weakness of this model is that the model requires the phase field on all mesh nodes to be updated at every step of the simulation, which can result in inefficiency.

In [67], a Level Set Method for dislocation dynamics was proposed by Xiang and co–workers using fast Fourier transform methods. The Level Set Method is a means to model the evolution and complexity of the geometries (such as dislocation structures), which is achieved using a straightforward functional representation [68, 69]. Xiang et.al successfully applied this method to simulate three-dimensional motion of dislocations and to account for dislocation glide, cross-slip and climb. However, due to the fact that both of dislocation dynamics methods of Khachaturyan et. al. and Xiang et.al have limitations for the mesh size, such models could suffer from the loss of resolution and as a result, the Frank-Read sources could remain inactive leading to unrealistic dislocation densities[56]. An alternative method was proposed by Lemarchand [70], which directly approximates the displacement field. The effect of the dislocations in the continuum was introduced through a plastic

strain. The biggest disadvantage of this alternative method is that it has limitations regarding the dimension of the simulated configurations, and the number of the dislocations (although the density of the dislocations can be very high).

2.3.2 Models based on superposition

Another class of dislocation models is based on superposition, where the continuum model solution is obtained by the superposition of infinite domain analytical solutions. In two dimensions, such analytical solutions are known for isotropic materials; however, in three dimensions they take the form of integral equations. The assumption of lattice isotropy is known to lead to errors as large as 20-30% [19] and it is preferred to avoid it in quantitative simulations. Since the material typically has a finite size, there is an interaction between the boundary of the material and the dislocations, which results in the image force on the dislocations. Thus, the boundary conditions are imposed on free surfaces using the concept of stress field superposition corresponding to the dislocations in an infinite elastic domain, and the stress field of the finite domain without dislocations, which is obtained by solving a complementary problem where the corresponding boundary conditions are applied [5, 62]. In other words, the solution on a finite domain is obtained by applying the image traction from the infinite domain solutions of all dislocations to the boundary of the domain, see the Fig:2.13. Although, the image field solutions are quite smooth and do not require high resolution. The complementary problem is typically solved by using the finite element method. The Peach-Koehler force at each dislocation is obtained by adding the

effect of all other dislocations. When dislocations cross the material boundary, the image stress given by the Peach–Koehler formula becomes singular at the intersecting points. In order to deal with singularity, virtual dislocations were introduced outside the material in such a way that the dislocations form closed loops before the complementary problem is solved [62].

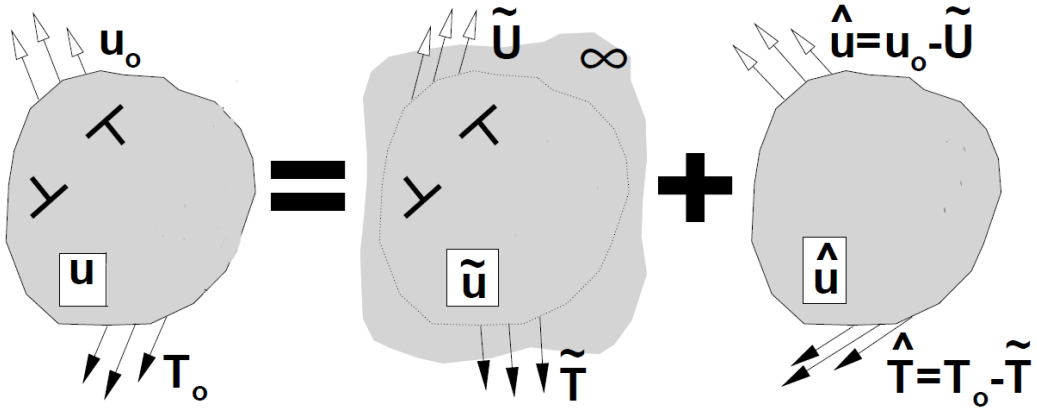

Figure 2.13: Principal of Superposition. Infinite fields are denoted with ˜. Image fields are denoted with ˆ. Modified [5]

One main weaknesses of these type of models is that Green's functions for the complicated geometries, material interfaces and anisotropic materials may not always exist. Another main weakness is the high computational cost typically associated with these type of models. Nevertheless, with the development of the Green's functions the method of superposition is likely to be widely used, due to its relative ease of use. Recently, the simulations incorporating anisotropic elasticity into the model were presented in [71, 72, 73, 74].

2.3.3 The eXtended Finite Element Method

This category of dislocation dynamics models is based on a technique that has been recently developed and is capable to model material anisotropy, arbitrary interfaces and grain boundaries [75]. The eXtended Finite Element Method (XFEM) is the base of this technique. This technique allows for the modeling of the non-smooth solutions independent of the finite element mesh [76, 77]. The non smooth solutions are the functions that do not have derivatives of all orders in the defined domain, and therefore, can include arbitrary discontinuities, high gradients, or singularities of different orders[78]. Moreover, the XFEM methodology can be used to treat the evolution of non smooth features (singularities, discontinuities, etc.) without remeshing. The XFEM was initially developed to deal with linear elastic fracture mechanics [79]. Later, the XFEM was extended to some other problems, e.g. to nonlinear fracture mechanics [80], multi-material[81] and multi-field [82] problems, two–phase flow [83].

The XFEM has been successfully used to model the dislocation dynamics of two–dimensional [75] and three–dimensional materials [84, 85]. This method provides a convenient way to model a dislocation using Volterra's concept described in Sec. 2.1 [75]. The XFEM allows for the modeling of dislocation dynamics without having to refine or reconstruct the finite element mesh [86]. In the classical Finite Element Method (FEM), the mesh has to conform to the discontinuities created by the dislocations. The construction of such meshes is a challenging task, especially, when modeling many dislocations. More so,

the FEM mesh has to be reconstructed when dislocations move, whereas the XFEM mesh is independent of dislocation location and geometry, therefore reconstruction is not needed [78]. The difference in mesh layout has been visualized for the case of grain boundary problem, where the construction of XFEM mesh is highly advantageous (See Fig.2.14).

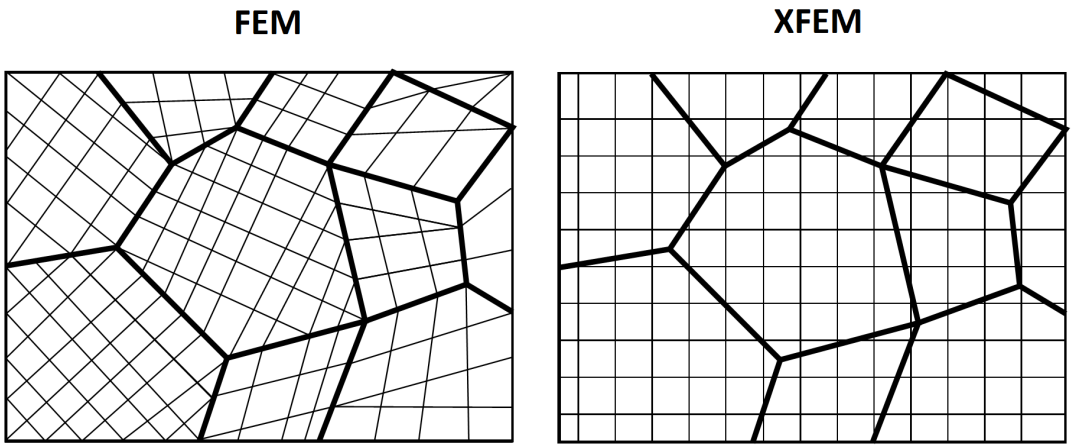

Figure 2.14: FEM(left) and XFEM(right) mesh for the grain boundary problems [87].

The two new dislocation dynamics models (Ch.3) and Ch.4) presented in this thesis are developed based on XFEM, and so this particular type of methodology is presented here with detail greater than any others considered thus far.

The work of Ventura et al. [88] had a particular influence on the development of this method. Their dislocation model is based on the Partition of Unity Method (PUM), that was proposed and proofed to converge by Melenk and Babuška [89]. The functions $\check{N}_i(\mathbf{x})$ form a partition of unity in n-dimensional domain Ω, when:

$$\sum_{i\in\check{S}} \check{N}_i(\mathbf{x}) = 1 \tag{2.4}$$

where $\check{S}$ is the set of mesh nodes. This property is vital for XFEM in terms of convergence and the patch test. The partition of unity empowers the finite element approximation of the solution to reproduce the rigid body motion precisely.

In XFEM, a displacement function $\mathbf{u}(\mathbf{x})$, $\mathbf{x} \in \Omega$ is modeled by adding a so called enrichment, which is accomplished through partition of unity, to the finite element polynomial approximation , i.e.:

$$\mathbf{u}^h(\mathbf{x}) = \sum_{i\in S} N_i(\mathbf{x})\mathbf{u}_i + \sum_{i\in\check{S}} \check{N}_i(\mathbf{x})\psi(\mathbf{x})\mathbf{a}_i \tag{2.5}$$

The first term of the right side of the Eq.(2.5) is the standard finite element approximation. The second term is the enrichment. The function $\psi(\mathbf{x})$ is the enrichment function, that incorporates some knowledge about the physics of the problem (e.g. singularities, jumps, etc.) and information from asymptotic solutions into the approximation space. It was shown in [89] that by partition of unity property, the approximation Eq.(2.5) can represent any enrichment function, $\psi(\mathbf{x})$, exactly. In Eq.(2.5), $N_i(\mathbf{x})$ and $\check{N}_i(\mathbf{x})$ are the standard finite element shape functions, which are often, but not necessarily, chosen to be the same, i.e. $N_i(\mathbf{x}) = \check{N}_i(\mathbf{x})$. The coefficients $\mathbf{u}_i$ are the standard degrees of freedom, $\mathbf{a}_i$ are the additional nodal unknown parameters. The values $\mathbf{a}_i$ adjust the enrichment to its finest approximation. For example, as it will be shown later in Ch.3 and Ch.4, in the displacement approximation without core enrichment, these nodal unknowns are the

Burgers vectors magnitudes of the dislocations, which are prescribed. It is important to

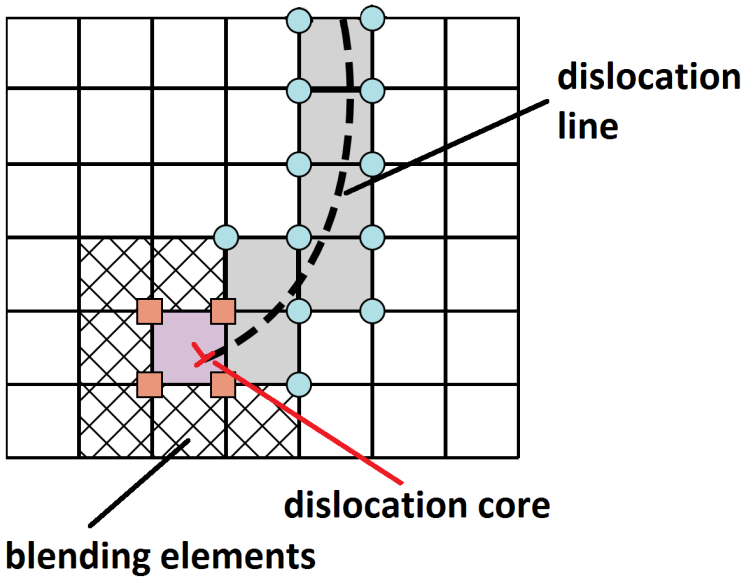

Figure 2.15: An arbitrary dislocation structure with step enriched (gray) and core enriched (purple) elements. The crosshatched elements are the blending elements. Modified from [87]

notice here, that the approximation Eq.(2.5) is enriched locally, i.e. $\check{S} \in S$ (the circled and squared nodes in Fig.2.15), where S is the set of all mesh nodes. This is typical for the XFEM method, since the phenomena, or in our case the dislocations, are usually locally present and it is not computationally efficient to enrich every node of the mesh, i.e. globally. However, there could be some difficulties in the blending elements, which are the elements where only some nodes are enriched [81, 90]. The functions $\check{N}_i(\mathbf{x})$ satisfy the partition of unity property only when all element's nodes are enriched, otherwise the enrichment function, $\psi(\mathbf{x})$, is not guaranteed to be represented exactly. However, different

strategies have been developed to take care of the blending elements and they seemed to work effectively without a significant lost in convergence rate [91, 92, 93]. It should be noted that for piece–wise constant enrichment function there are no problems in blending elements, since the enrichment disappears along its edges. This is particularly important for the current work, which utilizes a Heaviside step enrichment function (defined later in Ch.3) that is used in displacement field approximation. Thus, it is a piece–wise constant function, and so there will be no need in treatment of the blending elements, which could possibly cause the reduction of the optimal XFEM convergence rate. To visualize the enriched and blending elements for the arbitrary dislocation, see Fig.2.15.

Note that in order for the enrichment function to disappear at the edges of all elements, so that $\mathbf{u}^h(\mathbf{x}) = \mathbf{u}_i$, the approximation Eq.(2.5) has to have the property of Kronecker-δ. This can be done by shifting the approximation as was proposed by Belytschko et. al.[77], i.e.

$$\mathbf{u}^h(\mathbf{x}) = \sum_{i \in S} N_i(\mathbf{x})\mathbf{u}_i + \sum_{i \in \check{S}} \check{N}_i(\mathbf{x})[\psi(\mathbf{x}) - \psi(\mathbf{x}_i)]\mathbf{a}_i \tag{2.6}$$

This approximation is still able to reproduce the enrichment function, $\psi(\mathbf{x})$, exactly [78]. When the shifting is performed the essential boundary conditions are met at the very node. At this time, the Eq.(2.6) can be officially called the standard eXtended Finite Element approximation.

Another difficulty that may arise while implementing the XFEM is the quadrature of weak form. The derivation of the weak forms will be given in details for the two multi-

physical dislocation dynamics models in Ch.3 and Ch.4 respectively. Here, it is enough to mention that a weak form is represented by integral equations. So, when the approximation space is enriched, the smoothness of the integrable function can suffer due to the presence of the discontinuities and singularities. Thus, the standard Gauss quadrature method that is usually used in FEM to resolve the integrals can not be easily applied. However, several techniques have been developed to perform the integration accurately without affecting the convergence performance of XFEM [79, 94, 95]. Furthermore, in the case of the step function enrichment in the presented work, a simple mapping into equivalent polynomials is done, which allows the integration to be performed by standard Gauss quadrature method [93].

In the XFEM, the Level Set Method is used to describe the evolving geometry of the dislocations. As it was mentioned in Sec.2.3.1, the level set approach proved to be quite successful when modeling the dislocation dynamics. In addition, this method continues to find its new applications, such as modeling multiphysical phenomenon that are often present during plastic deformation. The detailed theoretical formulations of two such multiphysical models, developed in the current work, are presented in Ch.3 and Ch.4.

2.4 Dislocations in piezoelectric materials

Now that the basic concepts have been introduced and the main existing methods of modeling dislocations and discrete dislocation dynamics have been reviewed, the matter of

multiphysical phenomena can now be discussed.

Because interest in physical properties of piezoelectric materials has become so great, both in terms of their performance and practical application, the need to model the behavior of such materials at each length scale has arisen. Piezoelectric materials are certain solid materials, including crystalline solids (crystals) and ceramics, that exhibit the effect of piezoelectricity, which is defined as the electricity or electrical charge produced by mechanical strain. The cause and effect of this phenomenon is known as the direct piezoelectric effect. It is closely related to the converse (or inverse) effect, where a piezoelectric material becomes strained when electrical charge is applied by the amount proportional to the electrical field. Both effects are manifestations of the same fundamental property of the piezoelectric material [96]. Schematically the direct and converse piezoelectric effects are shown in Fig.2.16 and Fig.2.17 correspondingly.

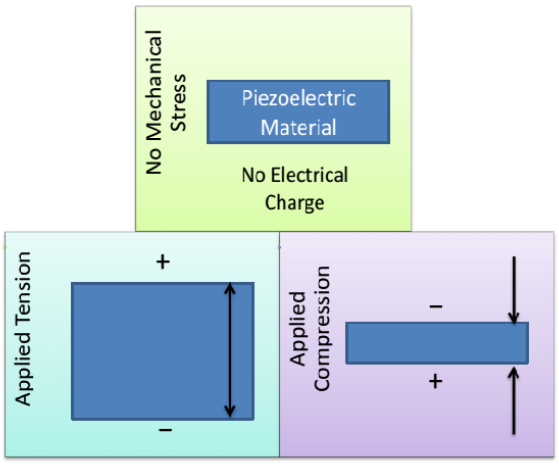

Figure 2.16: Direct piezoelectric effect.

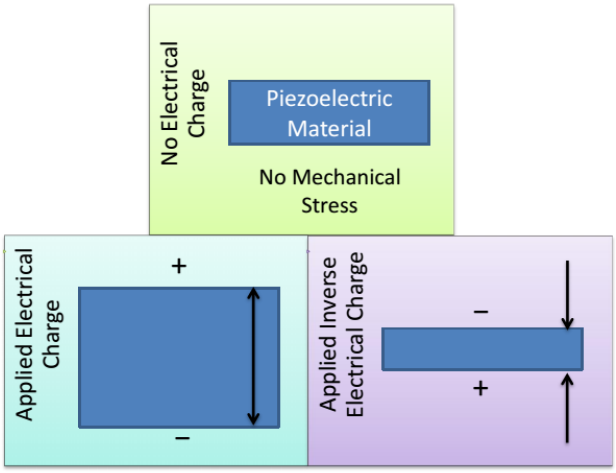

Figure 2.17: Converse piezoelectric effect.

Piezoelectricity was discovered in 1880 by French physicists and brothers Jacques and Pierre Curie. They took the name from the Greek word piezein, which means to squeeze or press. The converse effect was mathematically deduced from fundamental thermodynamic principles by Gabriel Lippmann in 1881. Brothers Curies confirmed the existence of the converse effect and quantitatively proved it. Only noncentrosymmetric crystals exhibit the piezoelectric effect. Noncentrosymmetric crystals have no center of symmetry, i. e., a point through which the crystal structure displays inversion symmetry. When such a crystal is deformed, the noncentrosymmetry results in nonuniform charge distribution within a crystal's unit cells.

A typical noncentrosymmetric crystal structure of an engineered piezoelectric material, for example lead zirconate titanate (PZT), has a net non-zero charge in each unit cell of the crystal, see Fig.2.18. A positive ion is located slightly off-center inside the unit cell,

which creates an electrical polarity, turning the unit cell into an electric dipole. When a mechanical stress is applied, the position of the positive ion changes causing a change in the polarity of the crystal. This is the origin of the direct piezoelectric effect. When the electrical field is applied, the position of the positive ion also changes causing the mechanical distortion of the unit cell, which is the origin of the converse piezoelectric effect.

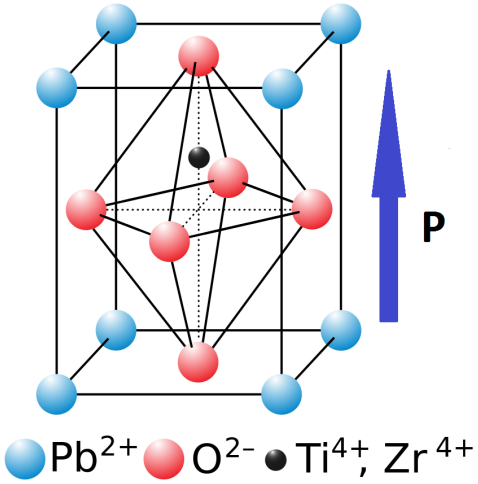

Figure 2.18: Lead zirconate titanate unit cell. Electrical polarity, **P** [97].

In order for an inorganic piezoelectric material to exhibit strong piezoelectric properties, the dipoles in crystalline structure should be more or less oriented in the same direction, which is done by poling it, see Fig.2.19. The direction along which the dipoles align is known as the poling direction. Conventionally, the poling direction is considered to be the the z-axis of the material coordinate system. When the crystal's principal directions are aligned with the material coordinate system, or spatial directions, the material prop-

erties can be used without any changes. However, it is important to take material spatial orientation and poling direction into account in order to correctly interpret the material properties. During poling a strong electric field is applied across the material, which orients all the dipoles in the direction of the field. After poling the orientation of the dipoles becomes roughly the same.

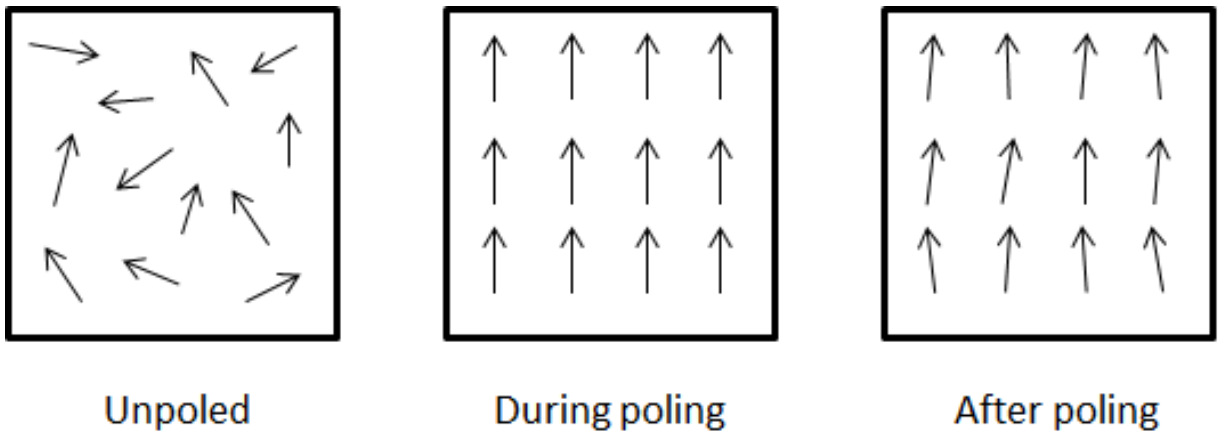

Figure 2.19: Poling. Arrows represent the dipoles [98].

Due to the inherent multiphysical effects that takes place between electric and mechanical fields, piezoelectric materials have been widely used as sensors, transducers, and actuators, which are key components of many very small electronic devices. However, the dislocations become barriers to charge carriers, as schematically shown in Fig. 2.20. This phenomena leads to the change in plastic behavior by creating additional forces that either opposes or drives deformation.

Improving the reliability of electronic devices depends in part on developing a more

in-depth understanding of dislocations. Moreover, it has been found that the electric field influences the grain growth [99], rates of recrystallization (a process by which deformed grains are replaced by a new set of undeformed grains that nucleate and grow until the original grains have been entirely consumed) [100], and even superplasticity (a state in which solid crystalline material is deformed well beyond its usual breaking point) [101]. The aforementioned phenomena belong to crystal plasticity scale, and so modeling mesoscale behavior of piezoelectric materials is an essential tool in providing insights for understanding these phenomena. Ultimately, such modeling is pivotal for the design of any devices subject to both electrical and mechanical loads.

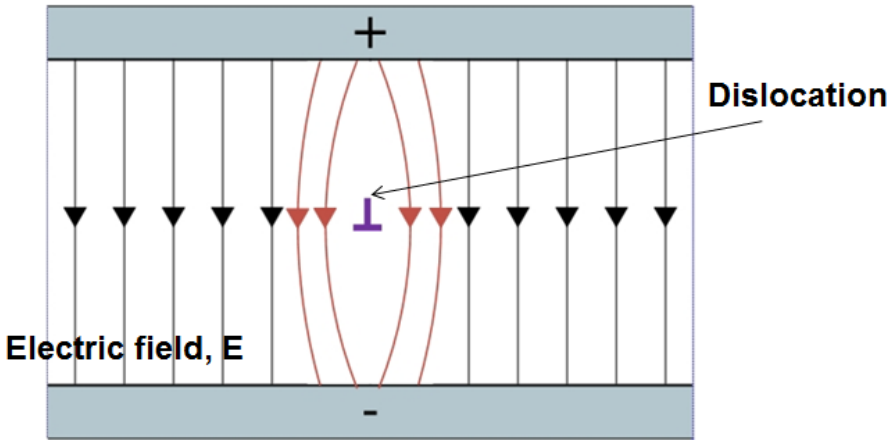

Figure 2.20: Dislocation as a barrier for the electric field.

Merten [102] was the first to investigate the effect of a dislocation on an electric field in piezoelectric materials. However, in his study, the converse piezoelectric effect was neglected and isotropy of the materials was assumed. The first analytical solutions for a

dislocation in an infinite two–dimensional piezoelectric media were developed by Barnett and Lothe in 1975, based on an extension of the Stroh formalism (a mathematical method for analysis of the anisotropic elasticity equations) [103]. For a straight line defect, i.e. dislocation, these solutions require the numerical evaluation of an integral and so are significantly more computationally complex than the isotropic elasticity solutions often used in two-dimensional discrete dislocation dynamics simulations. The problem of a single moving dislocation in an infinite piezoelectric material was studied analytically [104], [105], [106]. A moving edge dislocation in an anisotropic piezoelectric crystal was considered in [107] using Green's theorem and Fourier integral transformations, where the electro-elastic fields were expressed in an integral form. Later, the exact and explicit solutions for a moving screw dislocation and an edge dislocation in hexagonal piezoelectric crystalline solids were derived using eigenstrain theory and Fourier integral transformations ([108]). However, their solutions do not satisfy the jump conditions of the elastic displacement across the slip plane ([106]). It is clear from the literature, that the electromechanical coupling and its inherent anisotropy add significantly to the mathematical difficulties of the problem. The known solutions are very complicated even for simple geometries and isotropic materials and are largely for single material infinite domain systems. This can be contrasted with the finite dimensions, material interfaces and anisotropic materials used in electronic devices. Even though, as was mentioned in Sec.2.3, discrete dislocation dynamics simulations are widely used to model the material behavior at mesoscale, they are purely

mechanical and consider neither direct nor converse piezoelectric effects. The current work proposes a new discrete dislocation dynamics model variant which allows simulation of the anisotropic piezoelectric materials behavior at the mesoscale. This model captures the multiphysical effects between electric and mechanical fields in the presence of many moving dislocations, see Ch.3.

2.5 Dislocation dynamics and thermal effects

The strain rates in discrete dislocation dynamics simulations are typically high, varying from $10^3\ s^{-1}$ to $10^6\ s^{-1}$ [109]. When a large number of dislocations glide under high strain rates, they generate a significant amount of heat. At atomic scale, the heat generation can be explained by relieving the internal strain energy. Plastic deformation, or dislocations movement, stretch and then break the bonds between atoms. The energy gets released and converted into heat, which causes the local heating. Under high strain rate plastic deformation the heat generation rate is much higher than the heat conduction rate, which causes the local heating in the area of high dislocation concentration. In [10], for example, the maximum local temperature of about 1273 K was observed during the dynamic torsion test in titanium alloys. It happened inside shear bands (a narrow zone of intense shearing strain which develops during high strain deformation and characterized by massive collective dislocation activity) that formed just before failure of the materials. In [110], the local temperature effects associated with twinning (crystal deformation mechanism accompa-

nied by intergrowth of two separate crystals) at room temperature were studied. The local temperature rise due to formation and motion of dislocations that accommodate twinning was observed in this study as well.

It was emphasized in [111], that when heat generation during dislocation motion is significant, the equilibrium equations should be solved together with the equation of heat conduction and Fourier law in order to more accurately model high strain rate plasticity. Thus, it is important to consider the energy converted into heat when plastic deformation occurs [112]. The influence of substantial heat generation on the plastic behavior of metals at high rate deformation has been incorporated into some constitutive laws and energy balances [113, 114, 115, 116]. However, in order to gain in–depth knowledge of such thermal phenomena and its effects on material response, it is critical to develop mesoscale models capable of tracking every dislocation and capturing the heat generated when the dislocation moves. Recently, Tang and Marian conducted dislocation dynamics simulations in single crystal of iron at several high strain strain rates and temperatures [109]. The temperature-dependent dislocation mobility relations were used to account for thermal effects. However, the coupling effect between thermal and mechanical fields was not considered. The restraint of the existing dislocation dynamics models is that the thermal effects are accounted only through certain temperature dependent parameters, such as dislocation drag and critical resolved shear stress. Those parameters are calculated at different temperatures, then the purely mechanical simulations are performed considering only corresponding thermal

expansion [117, 118, 119].

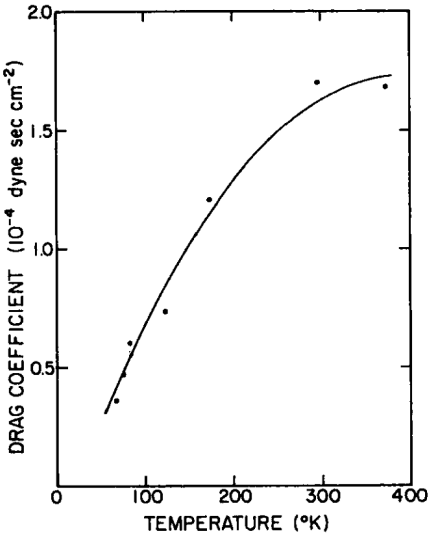

Figure 2.21: Thermal effect on dislocation drag in copper single crystal [120].

The first step in creation of a model for the rate dependent thermoplastic system is to develop discrete dislocation dynamics models which incorporate heat transfer. As it was mentioned in the previous section, existing discrete dislocation dynamics models are purely mechanical. Such mechanical models have several error sources due to their neglect of thermomechanical physics. First, the local elastic stresses are overestimated. For example, for a modest local temperature rise of 500 K, a metal with E=50 GPa and a linear coefficient of thermal expansion of $10 \cdot 10^{-6}\ K^{-1}$ would actually result in a local stress reduction of 250 MPa due to thermal expansion. Second, dislocation drag is underestimated. It has been observed that in most metals, the drag coefficient increases with temperature increase by one order of magnitude over the temperature range 100–700 K [121], [122]. For example

see Fig.2.21, where the dislocation drag increases with temperature up to 400 K for copper single crystal. In addition, the effect of dislocation drag increases with increase of strain rate [123]. The current work proposes a new discrete dislocation dynamics model variant to address these kinds of error sources, capture the heat generation effect, and incorporate heat conduction, see Ch.4.

2.6 Concluding remarks

The literature review on research into the modeling of dislocations was presented. The basic elements of dislocation theory were explained, which included two types of dislocations and their Burgers vectors, different mechanisms of dislocation motion, a Frank–Read source mechanism for dislocation generation, and driving force on a dislocation. The main methods to model a dislocation were described. After that, the main classes of discrete dislocation dynamics models with their major strengths and limitations were reviewed. In particular, attention was given to the eXtended Finite Element Method, which is the method used in the current work. The inherent multiphysical properties of the piezoelectric materials under electrical and mechanical loads were defined. The effect of the dislocation on electric field was discussed. In addition, thermal effects due to dislocation motion under high strain rate deformation were determined. Thus, two main areas for improvement to existing discrete dislocation models were identified respectively. The first area is related to the modeling of plastic piezoelectic material behavior accounting for the inherent multi-

physical phenomena. The second area is related to the modeling of high strain rate plastic deformation of crystalline solids accounting for thermal effects associated with dislocation motion.

Chapter 3

Electromechanical Dislocation Dynamics model

The first fully coupled two-dimensional electromechanical (EM) Discrete Dislocation Dynamics (DD) model is developed in this chapter. The eXtended Finite Element Method (XFEM) is used to develop DD simulations for the coupled electromechanical system. This EM–XFEM–DD model bridges the gap between two scales, atomic- and micro-scale, incorporating the inherent multiphysical effect of piezoelectric materials. The deformation process is assumed to be quasi-static and involves small strains leading to the nucleation, motion, and interactions of the dislocations.

The chapter has the following structure: in the first section, the strong and weak formulations for the EM–XFEM–DD model are developed and the discrete equations are derived. In the second section, the verification of the EM–XFEM–DD model is presented for a single edge dislocation in the middle of a domain. Then, the computation of the

Peach–Koehler force using the J-integral is discussed. The piezoelectric effect on the Peach–Koehler force near a free surface is studied. Thereafter, phenomenological rules for the dislocation dynamics are presented. Next, the nucleation and motion of a network of the dislocations in an anisotropic piezoelectric material under electrical and mechanical loads are simulated. The effect of the electromechanical load on material response is quantitatively presented and discussed. Finally, in the last section, concluding remarks are given. The EM–XFEM–DD model formulation and the results presented in this chapter were published in [124].

3.1 Theoretical formulation of the coupled EM–XFEM–DD model

In this section, the strong and weak forms for a discrete dislocations model are developed and the discrete equations are derived. The strong form consists of the governing equations and the boundary conditions for a physical system. The weak form is an integral form of these equations, which is needed to formulate the eXtended Finite Element Method.

3.1.1 Strong form of the coupled electromechanical system

We start by determining the strong form of the equations for the coupled electromechanical problem in a two-dimensional case. Consider a domain Ω bounded by Γ as shown in Fig.3.1. The domain contains n_d dislocations (surfaces of discontinuity). The boundary Γ

is decomposed into the sets Γ_u,Γ_φ,Γ_t, and $\Gamma_{\hat{q}}$, such that

$$\Gamma_u \cap \Gamma_t = \emptyset \text{ and } \Gamma_u \cup \Gamma_t = \Gamma \tag{3.1}$$

$$\Gamma_\varphi \cap \Gamma_{\hat{q}} = \emptyset \text{ and } \Gamma_\varphi \cup \Gamma_{\hat{q}} = \Gamma \tag{3.2}$$

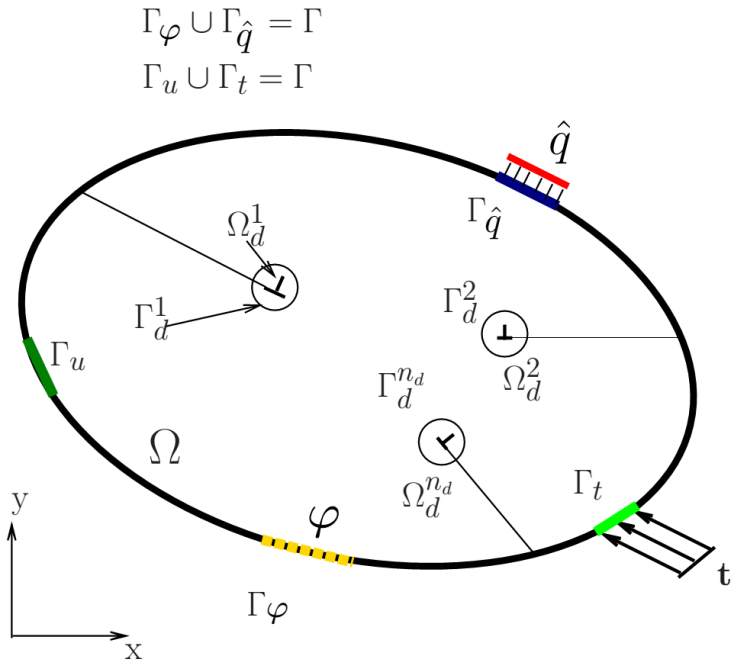

Figure 3.1: Domain definition and notation.

The internal surface of discontinuity α is denoted by Γ_d^α , where α is from 1 to n_d and n_d is the total number of dislocations in the domain. Surfaces Γ_d^α are the active parts of slip planes. We set $\Gamma_d = \cup_\alpha \Gamma_d^\alpha$. Let $\Omega_d = \cup_\alpha \Omega_\alpha^d$. Here, Ω_α^d is the core region, where the strain energy is unbounded; whereas the strain energy in Ω/Γ_d is bounded. Since we are

considering a coupled problem, two sets of governing equations should be solved together; the equilibrium equation and Gauss' law respectively:

$$\nabla \cdot \boldsymbol{\sigma} + \mathbf{g} = \mathbf{0} \tag{3.3}$$

$$\nabla \cdot \mathbf{D} = \rho \tag{3.4}$$

where $\boldsymbol{\sigma}$ is the Cauchy stress, $\mathbf{g}$ is the body force, $\mathbf{D}$ is the electric flux density vector (electric displacement), and ρ is the body charge density.

The constitutive equations for the coupled system are given by

$$\boldsymbol{\sigma} = \mathbf{C} : \boldsymbol{\varepsilon} - \mathbf{e} \cdot \mathbf{E} \tag{3.5}$$

$$\mathbf{D} = \mathbf{e}^{\top} : \boldsymbol{\varepsilon} + \boldsymbol{\epsilon} \cdot \mathbf{E} \tag{3.6}$$

where $\mathbf{C}$ is the tensor of the elastic moduli, or stiffness constants, measured in a constant electric field, $\boldsymbol{\varepsilon}$ is the strain, $\mathbf{e}$ is the piezoelectric tensor, and $\boldsymbol{\epsilon}$ is the dielectric tensor.

The piezoelectric tensor, $\mathbf{e}$, is a third-rank tensor. Recall, certain crystals develop an electric charge when strain is applied. The magnitude of this charge is proportional to the applied stress. This is known as the direct piezoelectric effect. On the other hand, when an electric field is applied in a certain crystals, the shape of the crystal changes. This is known as the converse piezoelectric effect. Its existence is a thermodynamic consequence of the direct piezoelectric effect. The coefficients connecting the electrical field and the strain in converse piezoelectric effect are the same as those connecting the stress and polarization

in the direct piezoelectric effect. They are called piezoelectric moduli and these are what the piezoelectric tensor, $\mathbf{e}$, consist of.

The dielectric tensor, $\boldsymbol{\epsilon}$, is the second-rank tensor. Its components are the ratio of the dielectric permittivity and vacuum permittivity. In other words, it is the ratio of the amount of electrical energy stored in a material by an applied electrical potential difference relative to that stored in a vacuum. In this formulation, the displacement, $\mathbf{u}$, and the electrical potential, φ, are taken to be the independent variables. The strain, $\boldsymbol{\varepsilon}$, and the electric field, $\mathbf{E}$, have the following relations with these variables:

$$\boldsymbol{\varepsilon} = \nabla_s \mathbf{u} \tag{3.7}$$

$$\mathbf{E} = -\nabla\varphi \tag{3.8}$$

where ∇_s is the symmetric part of the gradient matrix operator:

$$\nabla_s = \begin{bmatrix} \partial/\partial x & 1/2(\partial/\partial x + \partial/\partial y) \\ 1/2(\partial/\partial y + \partial/\partial x) & \partial/\partial y \end{bmatrix} \tag{3.9}$$

The coupled problem is complete when appropriate boundary conditions for the differential equations Eq.(3.3) and Eq.(3.4) are stated. The Dirichelet boundary condition, where the displacement $\mathbf{u}$ and the electric potential φ on the corresponding boundaries are known, are:

$$\mathbf{u} = \overline{\mathbf{u}} \text{ on } \Gamma_u \tag{3.10}$$

$$\varphi = \overline{\varphi} \text{ on } \Gamma_\varphi \tag{3.11}$$

The Neumann boundary condition, where the surface traction $\mathbf{t}$ and surface charge $\hat{q}$ are imposed on applicable boundaries, are:

$$\boldsymbol{\sigma} \cdot \mathbf{n} = \mathbf{t} \text{ on } \Gamma_t \tag{3.12}$$

$$\mathbf{D} \cdot \mathbf{n} = -\hat{q} \text{ on } \Gamma_q \tag{3.13}$$

When the domain contains the internal surfaces of discontinuities, the system is also subjected to internal boundary conditions as follows:

$$[|\mathbf{u}|] = \mathbf{b}^\alpha \text{ on } \Gamma_d^\alpha \tag{3.14}$$

where $|\mathbf{u}|$ is the jump in displacement and $\mathbf{b}^\alpha$ is the Burgers vector of dislocation α. This condition comes from the fact that Burgers vector represents the lattice distortion magnitude of the dislocation.

To summarize, the strong form of the boundary value problem comes down to finding $\mathbf{u} \in \mathbf{C}^1(\Omega/\Gamma_d)$ and $\varphi \in \mathbf{C}^1(\Omega)$, such that Eq.(3.3) and Eq.(3.4) are satisfied under the boundary conditions Eqs.(3.11) - (3.14).

In the general case, $\mathbf{C}^r(\Omega)$ denotes the space of continuous functions on Ω that have continuous first $r \in \mathbf{Z}$ derivatives on the same Ω. Space $\mathbf{Z}$ is the set of integers.
Notice that in order for the coupled solution of the strong form equations to exist and to be unique, the corresponding smoothness of the functions is a necessary requirement. However, the integral form of the equations eases the requirements on the solution, and thus is derived below.

3.1.2 Weak form of the coupled electromechanical system

We derive the weak form of the coupled electromechanical system starting with multiplying the equilibrium equation Eq.(3.3) by an arbitrary function $\phi \in \boldsymbol{\Upsilon}$ and integrating over the domain Ω. After integrating by parts, substituting the constitutive model for the stress Eq.(3.5), using Eq.(3.7) and Eq.(3.8) we have:

$$\int_{\Omega} \nabla \boldsymbol{\phi}^{\top} \cdot \mathbf{C} : (\nabla_s \mathbf{u}) d\Omega + \int_{\Omega} \nabla \boldsymbol{\phi}^{\top} \cdot \mathbf{e} \nabla \varphi d\Omega = \int_{\Gamma_t} \boldsymbol{\phi}^{\top} \cdot \mathbf{t} d\Gamma + \int_{\Omega} \boldsymbol{\phi}^{\top} \cdot \mathbf{g} d\Omega, \forall \boldsymbol{\phi} \in \boldsymbol{\Upsilon}, \quad (3.15)$$

where

$$\boldsymbol{\Upsilon} \quad = \quad \left\{ \boldsymbol{\phi} | \boldsymbol{\phi} \in \mathbf{H}^1(\Omega/\Gamma_d \mid \boldsymbol{\phi} = 0 \text{ on } \Gamma_u \right\} \quad (3.16)$$

Next we multiply the governing equation Eq.(3.4) and boundary condition Eq.(3.11) by an arbitrary function $\psi \in \boldsymbol{\Psi}$, where

$$\boldsymbol{\Psi} \quad = \quad \left\{ \psi | \psi \in \mathbf{H}^1(\Omega/\Gamma_d \mid \psi = 0 \text{ on } \Gamma_\varphi \right\} \quad (3.17)$$

Integrating by parts over the domain Ω, substituting the constitutive model for the electric displacement Eq.(3.6), using Eq.(3.7) and Eq.(3.8) we obtain:

$$\int_{\Omega} \nabla \psi^{\top} \cdot \mathbf{e}^{\top} \cdot (\nabla_s \mathbf{u}) d\Omega - \int_{\Omega} \nabla \psi^{\top} \cdot \boldsymbol{\epsilon} \nabla \varphi d\Omega = - \int_{\Gamma_{\hat{q}}} \psi^{\top} \hat{q} d\Gamma - \int_{\Omega} \psi^{\top} \rho d\Omega, \forall v \in \boldsymbol{\Psi} \quad (3.18)$$

The above mentioned Sobolev space $\mathbf{H}^m(\Omega)$ is defined by:

$$\mathbf{H}^m(\Omega) \quad = \quad \left\{ \mathbf{u} : D^{\alpha} \mathbf{u} \in L_2(\Omega); \forall \alpha \text{ such that } |\alpha| \leq m \right\}, \quad (3.19)$$

where $m \in \mathbf{Z}$ and ≥ 1, $D^{\alpha}\mathbf{u}$ denotes the α^{th} derivative of the function $\mathbf{u}$ on Ω. When $m = 0$, $\mathbf{H}^{m}(\Omega) = L_2(\Omega)$. The space L_2 is Lebesgue space. For a real number $p \geq 1$, the p-norm,or L_p norm, of $\mathbf{x} \in \Re^n$ is defined by:

$$||\mathbf{x}||_p = (|x_1|^p + |x_2|^p + ... + |x_n|^p)^{1/p} \tag{3.20}$$

It is important to notice that every strong solution is also a weak solution. However, there may be weak solutions which do not satisfy strong formulation. Therefore, it is important to correctly define the space where we are looking for the existing and unique solution in order for the weak form to be equivalent to the strong form of the equations.

To summarize, the weak form of the coupled system of the equations comes down to finding $\mathbf{u} \in \mathbf{H}^1(\Omega/\Gamma_d)$ and $\varphi \in \mathbf{H}^1(\Omega)$ such that Eqs.(3.15), (3.18) are satisfied under the boundary conditions Eqs.(3.11) - (3.14) for $\forall\phi \in \boldsymbol{\Upsilon}$ and $\psi \in \boldsymbol{\Psi}$.

3.1.3 Discrete form of the coupled electromechanical system

To describe the XFEM approach to dislocation dynamics, we first define the geometry of the dislocations. We consider an edge dislocation, which is described by the location of its core and the orientation and location of its glide plane, as illustrated in Fig. 3.2. The glide plane of dislocation α is represented by the zero contour of the function $f^{\alpha}(\mathbf{x})$, i.e. $f^{\alpha}(\mathbf{x}) = 0$. The function $f^{\alpha}(\mathbf{x})$ is taken as the signed distance to the glide plane. The intersection of the glide plane $f^{\alpha}(\mathbf{x}) = 0$ with another plane $g^{\alpha}(\mathbf{x}) = 0$ defines the location

of core α. The function $g^\alpha(\mathbf{x})$ is defined as the signed distance to the core, such that $f^\alpha(\mathbf{x}) \perp g^\alpha(\mathbf{x})$. The active part of the glide plane is defined by $f^\alpha(\mathbf{x}) = 0,\ g^\alpha(\mathbf{x}) \leq 0$. These definitions may be extended to three dimensions in a straight forward way [84]. Such a way to define the dislocations is called level set description and have been previously used to model dislocations dynamics, but using a different method than the one proposed here [67].

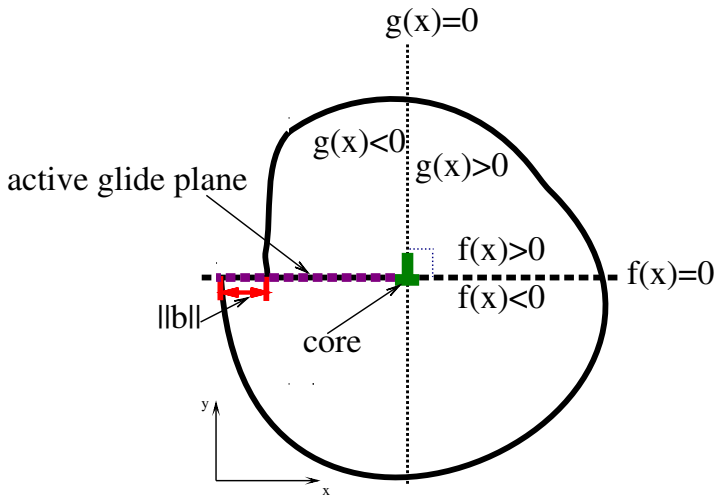

Figure 3.2: Description of an edge dislocation by functions $f(\mathbf{x})$ and $g(\mathbf{x})$. Dashed line represents the glide plane, and the $\mathbf{b}$ is the Burgers vector [124].

The XFEM displacement approximation used here for a domain which contains n_d edge dislocations with Burgers vectors $\mathbf{b}^\alpha$ has the following form:

$$\mathbf{u}^h(\mathbf{x}) = \sum_{I \in S} N_I(\mathbf{x})\mathbf{d}_I + \sum_{\alpha=1}^{n_d} \mathbf{b}^\alpha \sum_{J \in S^\alpha} N_J(\mathbf{x})[H(f^\alpha(\mathbf{x})) - H(f^\alpha(\mathbf{x}_J))],\ \ \forall \mathbf{x} \in \Omega \qquad (3.21)$$

where N_I are the standard finite element shape functions, $\mathbf{d}_I$ are the nodal displacement degrees of freedom, S is the set of all nodes, and S^α is the set of enriched nodes (i.e. nodes

of elements that are completely cut by the glide plane α, as shown in Fig. 3.3) $\mathbf{x}_J$ are the coordinates of enriched node J. The second term in Eq.(3.21) is called an enrichment and introduces the interior discontinuities into displacement field.

The Heaviside step function is given by

$$H(z) = \begin{cases} 1 & \text{if } z > 0 \\ 0 & \text{otherwise} \end{cases} . \tag{3.22}$$

The node with coordinates $\mathbf{x}_J$ is enriched, i.e. belongs to S^α, when $g^\alpha(\mathbf{x}_J) < 0$ and the

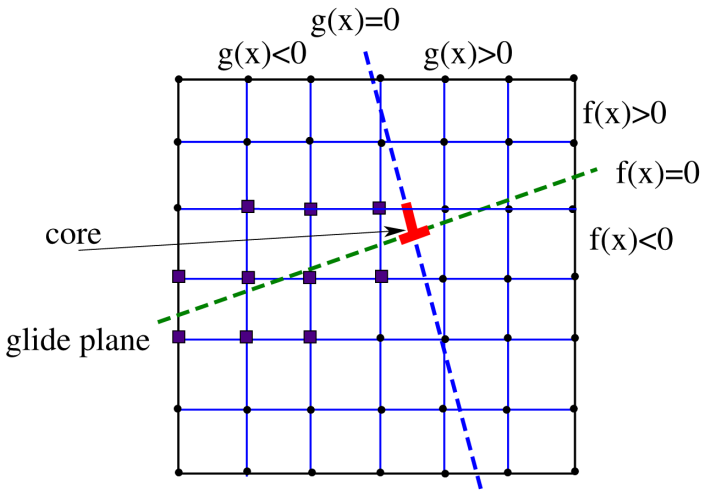

Figure 3.3: Illustration of the enriched nodes. Dark squares represent nodes in the S^α [124].

support of node $\mathbf{x}_J$ is intersected by $f^\alpha(\mathbf{x}) = 0$.

Although the displacement field approximation in Eq.(3.21) is discontinuous, the strain and stress fields are continuous. Thus, it is necessary to consider how the approximation

Eq.(3.21) with the chosen enrichment introduces the discontinuity into displacement field, and so we calculate the jump in the displacements across glide plane α:

$$[|\mathbf{u}(\mathbf{x})|] = \mathbf{u}^+(\mathbf{x}) - \mathbf{u}^-(\mathbf{x}), \quad \mathbf{x} \in \Gamma_d^\alpha \tag{3.23}$$

where $\mathbf{u}^+(\mathbf{x})$ and $\mathbf{u}^-(\mathbf{x})$ are the displacements above and below the glide plane, respectively. Substituting the approximation Eq.(3.21) into Eq.(3.23) and simplifying, we have:

$$[|\mathbf{u}(\mathbf{x})|] = [H^+(\mathbf{x}) - H^-(\mathbf{x})]\mathbf{b}^\alpha \sum_{J \in S^\alpha} N_J(\mathbf{x}), \quad \mathbf{x} \in \Gamma_d^\alpha \tag{3.24}$$

where $H^+(\mathbf{x})$and $H^-(\mathbf{x})$ are the values of the Heaviside step function above and below the glide plane, respectively. Therefore, it follows from Eqs.(3.24), (3.22) and the partition unity property of the $N_J(\mathbf{x})$ that:

$$[|\mathbf{u}(\mathbf{x})|] = \mathbf{b}^\alpha \text{ on } \Gamma_d^\alpha \tag{3.25}$$

The slip across the glide plane is captured with approximation Eq.(3.21) and is equal to $\mathbf{b}^\alpha$; therefore, the internal boundary conditions Eq.(3.14) are satisfied. Taking partial derivatives of Eq.(3.25), it is clear that the strains are continuous across Γ_d^α since $\mathbf{b}^\alpha$ is constant.

The electric potential is approximated by:

$$\phi^h(\mathbf{x}) = \sum_{I \in S} \bar{N}_I(\mathbf{x})\boldsymbol{\phi}_I, \quad \forall \mathbf{x} \in \Omega \tag{3.26}$$

where, $\bar{N}_I$ are standard finite element shape functions, $\boldsymbol{\phi}_I$ are nodal electric potentials . Following Galerkin's method [125], the test functions, $\mathbf{w}(\mathbf{x})$ and $v(\mathbf{x})$, are taken to be the

same form as Eq.(3.21) and Eq.(3.26), respectively, i.e.

$$\mathbf{w}(\mathbf{x}) = \sum_{I \in S} N_I(\mathbf{x}) \mathbf{w}_I + \sum_{\alpha=1}^{n_d} \sum_{J \in S^\alpha} N_J(\mathbf{x}) [H(f^\alpha(\mathbf{x})) - H(f^\alpha(\mathbf{x}_J))] \mathbf{c}^\alpha, \quad \forall \mathbf{x} \in \Omega \tag{3.27}$$

$$v(\mathbf{x}) = \sum_{I \in S} \bar{N}_I(\mathbf{x}) v_I, \quad \forall \mathbf{x} \in \Omega \tag{3.28}$$

Substituting the approximations Eq.(3.21) and Eq.(3.26), and the test functions Eq.(3.27) and Eq.(3.28) into the weak form of the Eq.(3.15) and Eq.(3.18), obtained in the previous Sec.3.1.2, and evoking the arbitrariness of the nodal degrees of freedom $\mathbf{w}_I$, $\mathbf{c}^\alpha$ and v_I the following discrete equations are obtained:

$$\begin{bmatrix} \mathbf{K}^{dd} & \mathbf{K}^{db} & \mathbf{K}^{d\phi} \\ \mathbf{K}^{db\top} & \mathbf{K}^{bb} & \mathbf{K}^{b\phi} \\ \mathbf{K}^{d\phi\top} & \mathbf{K}^{b\phi\top} & \mathbf{K}^{\phi\phi} \end{bmatrix} \begin{Bmatrix} \mathbf{d} \\ \mathbf{b} \\ \boldsymbol{\phi} \end{Bmatrix} = \begin{Bmatrix} \mathbf{f}^{ext} \\ \mathbf{f}_b^{ext} \\ \mathbf{q}^{ext} \end{Bmatrix} \tag{3.29}$$

where $\mathbf{d} = [\mathbf{d}_1^\top, \mathbf{d}_2^\top, ...\mathbf{d}_n^\top]^\top$ are the standard displacement nodal degrees of freedom, $\boldsymbol{\phi} = [\phi_1, \phi_2, ...\phi_n]^\top$ are the degrees of freedom that correspond to the electrical potential at each node, n is the number of nodes. The vector $\mathbf{b} = [\mathbf{b}^{1\top}, \mathbf{b}^{2\top}, ...\mathbf{b}^{n_d\top}]^\top$ consists of the slips along the glide planes, where n_d is the number of dislocations.

Since the slips along the glide planes are known, we can modify and then solve the system of the equations Eq.(3.29) with respect to the unknown nodal displacements $\mathbf{d}$ and nodal electrical potentials $\boldsymbol{\phi}$, as shown:

$$\begin{bmatrix} \mathbf{K}^{dd} & \mathbf{K}^{d\phi} \\ \mathbf{K}^{d\phi\top} & \mathbf{K}^{\phi\phi} \end{bmatrix} \begin{Bmatrix} \mathbf{d} \\ \boldsymbol{\phi} \end{Bmatrix} = \begin{Bmatrix} \mathbf{f}^{ext} - \mathbf{K}^{db}\mathbf{b} \\ \mathbf{q}^{ext} - \mathbf{K}^{b\phi\top}\mathbf{b} \end{Bmatrix} = \begin{Bmatrix} \mathbf{f}^{ext} - \mathbf{f}^{D} \\ \mathbf{q}^{ext} - \mathbf{q}^{D} \end{Bmatrix} \tag{3.30}$$

The submatrices from the system Eq.(3.29) and Eq.(3.30) are

$$\mathbf{K}_{IJ}^{dd} = \int_{\Omega} \mathbf{B}_I^{\top} \mathbf{C} \mathbf{B}_J d\Omega, \quad I, J \in S \tag{3.31}$$

$$\mathbf{K}_{IJ}^{d\phi} = \int_{\Omega} \mathbf{B}_I^{\top} \mathbf{e} \bar{\mathbf{B}}_J d\Omega, \quad I, J \in S \tag{3.32}$$

$$\mathbf{K}_{IJ}^{\phi\phi} = -\int_{\Omega} \bar{\mathbf{B}}_I^{\top} \boldsymbol{\epsilon} \bar{\mathbf{B}}_J d\Omega, \quad I, J \in S \tag{3.33}$$

$$\mathbf{K}_{I\alpha}^{db} = \int_{\Omega} \mathbf{B}_I^{\top} \mathbf{C} \mathcal{B}_{\alpha} d\Omega, \quad I \in S, \ \alpha = 1, 2, ..., n_d \tag{3.34}$$

$$\mathbf{K}_{\alpha\beta}^{bb} = \int_{\Omega} \mathcal{B}_{\alpha}^{\top} \mathbf{C} \mathcal{B}_{\beta} d\Omega, \quad \alpha, \beta = 1, 2, ..., n_d \tag{3.35}$$

$$\mathbf{K}_{I\alpha}^{b\phi} = \int_{\Omega} \bar{\mathbf{B}}_I^{\top} \mathbf{e} \mathcal{B}_{\alpha} d\Omega, \quad I \in S, \quad \alpha = 1, 2, ..., n_d \tag{3.36}$$

$$\mathbf{f}^{ext} = \int_{\Gamma_t} \mathbf{N}^{\top} \mathbf{t} \, d\Gamma - \int_{\Omega} \mathbf{N}^{\top} \mathbf{g} \, d\Omega \tag{3.37}$$

$$\mathbf{q}^{ext} = -\int_{\Gamma_{\hat{q}}} \bar{\mathbf{N}}^{\top} \, \hat{q} \, d\Gamma - \int_{\Omega} \bar{\mathbf{N}}^{\top} \rho \, d\Omega \tag{3.38}$$

$$\mathbf{f}^{D} = \sum_{\alpha=1}^{n_d} \int_{\Omega} \mathbf{B}_I^{\top} \mathbf{C} \mathcal{B}_{\alpha} \mathbf{b}^{\alpha} d\Omega, \quad I \in S \tag{3.39}$$

$$\mathbf{q}^{D} = \sum_{\alpha=1}^{n_d} \int_{\Omega} \bar{\mathbf{B}}_I^{\top} \mathbf{e}^{\top} \mathcal{B}_{\alpha} \mathbf{b}^{\alpha} d\Omega, \quad I \in S \tag{3.40}$$

where

$$\mathbf{B}_I = \begin{bmatrix} N_I(\mathbf{x})_{,x} & 0 \\ 0 & N_I(\mathbf{x})_{,y} \\ N_I(\mathbf{x})_{,y} & N_I(\mathbf{x})_{,x} \end{bmatrix} \tag{3.41}$$

$$\bar{\mathbf{B}}_I = \begin{bmatrix} N_I(\mathbf{x})_{,x} \\ \\ N_I(\mathbf{x})_{,y} \end{bmatrix} \tag{3.42}$$

and

$$\mathcal{B}_\alpha = \sum_{J \in S^\alpha} \begin{bmatrix} N_J(\mathbf{x})_{,x}(H(f^\alpha(\mathbf{x})) - H(f^\alpha(\mathbf{x_J}))) & 0 \\ 0 & N_J(\mathbf{x})_{,y}(H(f^\alpha(\mathbf{x})) - H(f^\alpha(\mathbf{x_J}))) \\ N_J(\mathbf{x})_{,y}(H(f^\alpha(\mathbf{x})) - H(f^\alpha(\mathbf{x_J}))) & N_J(\mathbf{x})_{,x}(H(f^\alpha(\mathbf{x})) - H(f^\alpha(\mathbf{x_J}))) \end{bmatrix} \tag{3.43}$$

$$\mathbf{N} = \begin{bmatrix} N_I(\mathbf{x}) & 0 \\ \\ 0 & N_I(\mathbf{x}) \end{bmatrix} \tag{3.44}$$

$$\bar{\mathbf{N}} = \begin{bmatrix} N_I(\mathbf{x}) \end{bmatrix} \tag{3.45}$$

Note that all terms on the left side of Eqs.(3.30) are independent of dislocations in terms of their location, number and geometry and, therefore, do not change for a given mesh as the dislocations move or as new dislocations are nucleated. If a nonlinear constitutive law was used instead of Eq.(3.5) and Eq.(3.6), this stiffness matrix would depend on the number and location of the dislocations, and so would have to be updated at each step and iteration of the simulations. Importantly, the mechanical effect of the dislocations appears as a force on the right hand side of the equations and is captured with the XFEM dislocation dynamics model.

3.2 Verification of the electromechanical XFEM dislocation model

In this section, we present an example where the electromechanical XFEM model is verified for the problem of a single edge dislocation.

3.2.1 Theoretical formulation of FEM with Lagrange multipliers

In order to verify the XFEM dislocation model, we used another numerical method, namely, the finite element method with Lagrange multipliers. We used Babuška's idea [126], where he applied the Lagrange multipliers to approximate essential boundary conditions in the Dirichlet problem. Below we show the mathematical derivations that are applied to the simple problem of the one edge dislocation in the middle of the domain.

To find the solution of our problem subjected to the internal boundary conditions we define a functional, or so called Lagrangian of the problem, Λ :

$$\Lambda = H(\mathbf{u}, \boldsymbol{\varphi}) + G(\boldsymbol{\lambda}, \mathbf{u}, \boldsymbol{\varphi}) \tag{3.46}$$

The first term of the Lagrangian is the potential energy, $H(\mathbf{u}, \boldsymbol{\varphi})$, that we need to minimize over all functions satisfying the prescribed internal boundary conditions, or so called constraints, $G(\boldsymbol{\lambda}, \mathbf{u}, \boldsymbol{\varphi})$. We do not have internal constraints on potential field, therefore the functional $\mathbf{G}$ does not depend on the variable $\boldsymbol{\varphi}$. However, in order to satisfy the internal boundary condition for the displacement field, 3.14, we construct $\mathbf{G}$ as:

$$G(\boldsymbol{\lambda}, \mathbf{u}) = \int_{\Gamma_d} \Upsilon(\mathbf{x}) \cdot (\mathbf{u}^+(\mathbf{x}) - \mathbf{u}^-(\mathbf{x}) - \mathbf{b}) d\Gamma_d \tag{3.47}$$

$$\Upsilon(\mathbf{x}) = \sum_{L \in \mu} \boldsymbol{\lambda}_L \delta(\mathbf{x} - \mathbf{x}_L), \ \mathbf{x}_L \text{ on } \Gamma_d \tag{3.48}$$

Finding the stationary points for the Lagrangian creates the solution for our initial problem. Above, the displacement function on upper side of the boundary Γ_d is denoted with a "+" and belongs to Γ_d^+; on the lower side with "-" and belongs to Γ_d^-. Fig.3.4 schematically shows the boundaries and the nodes. Index L is the number of Lagrange multipliers $\boldsymbol{\lambda}_L$ that is equal to the number of the nodes of the mesh μ on the glide plane. For each node L there is a pair of displacements $\mathbf{u_I}$ and $\mathbf{u_J}$, where I and J correspond to the upper side of and lower side of the glide plane respectively.

Using the property of the delta function:

$$\int f(t)\delta(t - \tau)dt = f(\tau) \tag{3.49}$$

and substituting (3.48) in (3.47), we get:

$$G(\lambda, \mathbf{u}) = \sum_{L \in \mu} \boldsymbol{\lambda}_L \cdot (\mathbf{u}^+(\mathbf{x}_L) - \mathbf{u}^-(\mathbf{x}_L) - \mathbf{b}) \tag{3.50}$$

The FEM approximation for the displacements on the internal boundary will be the following:

$$\mathbf{u}^+(\mathbf{x}_L) = \sum_I N_I(\mathbf{x}_L)\mathbf{u}_I = u_I \overline{\delta}_{IL} \tag{3.51}$$

$$\mathbf{u}^-(\mathbf{x}_L) = \sum_J N_J(\mathbf{x}_L)\mathbf{u}_J = u_J \overline{\delta}_{JL} \tag{3.52}$$

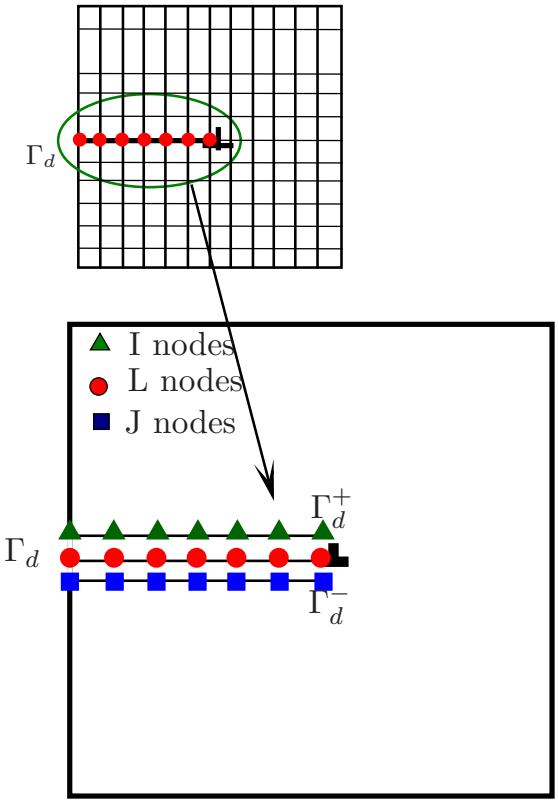

Figure 3.4: Glide planes and the nodes for the approach with Lagrange multipliers.

where

$$\overline{\delta}_{IL} = \begin{cases} 1 & \text{if } I \neq L, \mathbf{x}_I = \mathbf{x}_L \\ 0 & \text{otherwise} \end{cases} \tag{3.53}$$

$$\overline{\delta}_{JL} = \begin{cases} 1 & \text{if } J \neq L, \mathbf{x}_J = \mathbf{x}_L \\ 0 & \text{otherwise} \end{cases} \tag{3.54}$$

Therefore, after substituting (3.53) and (3.54) in (3.50) we have:

$$G(\lambda, \mathbf{u}) = \sum_{L \in \mu} \boldsymbol{\lambda}_L \cdot (\mathbf{u}_J \overline{\delta}_{JL} - \mathbf{u}_J \overline{\delta}_{JL} - \mathbf{b}) \tag{3.55}$$

The solution will be determined by the equations defining the critical points of the Lagrange

functional, namely

$$\left\{ \begin{array}{c} \dfrac{\partial \Lambda}{\partial \mathbf{u}_k} \\ \\ \dfrac{\partial \Lambda}{\partial \boldsymbol{\varphi}_k} \\ \\ \dfrac{\partial \Lambda}{\partial \boldsymbol{\lambda}_L} \end{array} \right\} = 0 \tag{3.56}$$

or

$$\left\{ \begin{array}{c} \dfrac{\partial H}{\partial \mathbf{u}_k} + \dfrac{\partial H}{\partial \boldsymbol{\varphi}_k} + \dfrac{\partial G}{\partial \mathbf{u}_k} \\ \\ \dfrac{\partial G}{\partial \boldsymbol{\lambda}_L} \end{array} \right\} = 0 \tag{3.57}$$

Minimizing the potential energy $H(\mathbf{u}, \boldsymbol{\varphi})$ leads to the weak form of the coupled system (3.15) and (3.18). After applying the standard FEM approximations for the displacement and potential fields the standard discrete equations are obtained:

$$\left[\begin{array}{cc} \mathbf{K}^{dd} & \mathbf{K}^{d\phi} \\ \mathbf{K}^{d\phi\top} & \mathbf{K}^{\phi\phi} \end{array} \right] \left\{ \begin{array}{c} \mathbf{d} \\ \boldsymbol{\phi} \end{array} \right\} = \left\{ \begin{array}{c} \mathbf{f}^{\mathbf{ext}} \\ \mathbf{q}^{\mathbf{ext}} \end{array} \right\} \tag{3.58}$$

However, it is necessary for clarity purposes to present the partial derivatives of $G(\lambda, \mathbf{u})$

here in greater detail, as it is not so obvious:

$$\begin{aligned}\frac{\partial G}{\partial \mathbf{u}_k} &= \frac{\partial}{\partial \mathbf{u}_k}(\sum_{L\in\mu}\boldsymbol{\lambda}_L\cdot(\mathbf{u}_I\overline{\delta}_{JL}-\mathbf{u}_J\overline{\delta}_{JL}-\mathbf{b}))\\ &= \sum_{L\in\mu}\boldsymbol{\lambda}_L\cdot(\frac{\partial \mathbf{u}_I}{\partial \mathbf{u}_k}\overline{\delta}_{IL}-\frac{\partial \mathbf{u}_J}{\partial \mathbf{u}_k}\overline{\delta}_{JL})\\ &= \sum_{L\in\mu}\boldsymbol{\lambda}_L(\delta_{Ik}\overline{\delta}_{IL}-\delta_{Jk}\overline{\delta}_{JL})\\ &= \sum_{L\in\mu}\boldsymbol{\lambda}_L(\overline{\delta}_{IL}-\overline{\delta}_{JL}) \end{aligned} \tag{3.59}$$

Remark 1. Even though I and L are not the same, the physical locations $\mathbf{x}_I$ and $\mathbf{x}_L$ are; J and L are not the same, but the physical locations $\mathbf{x}_J$ and $\mathbf{x}_L$ are;

Remark 2. If node I is on the upper side Γ_d^+ of the boundary Γ_d and $L\in\mu$ then $\overline{\delta}_{IL}=1$ and $\overline{\delta}_{JL}=0$;

Remark 3. If node J is on the lower side Γ_d^- of the boundary Γ_d and $L\in\mu$ then $\overline{\delta}_{JL}=1$ and $\overline{\delta}_{IL}=0$;

Therefore, (3.59) becomes:

$$\frac{\partial G}{\partial \mathbf{u}_k}=\begin{cases}\sum_{L\in\mu}\boldsymbol{\lambda}_L\overline{\delta}_{IL} & I \text{ is on } \Gamma_d^+,\ L\in\mu\\ -\sum_{L\in\mu}\boldsymbol{\lambda}_L\overline{\delta}_{JL} & J \text{ is on } \Gamma_d^-,\ L\in\mu\end{cases} \tag{3.60}$$

In matrix form we can rewrite it as:

$$\frac{\partial G}{\partial \mathbf{u}_k}=[\mathbf{G}_k][\boldsymbol{\lambda}_L] \tag{3.61}$$

The derivative with respect to $\boldsymbol{\lambda}_L$ is straightforward:

$$\begin{aligned}\frac{\partial G}{\partial \boldsymbol{\lambda}_L} &= \frac{\partial}{\partial \boldsymbol{\lambda}_L}(\sum_{L\in\mu}\boldsymbol{\lambda}_L\cdot(\mathbf{u}_I\overline{\delta}_{JL}-\mathbf{u}_J\overline{\delta}_{JL}-\mathbf{b}))\\ &= \sum_{L\in\mu}(\mathbf{u}_I\overline{\delta}_{JL}-\mathbf{u}_J\overline{\delta}_{JL}-\mathbf{b}) \end{aligned} \tag{3.62}$$

Or in matrix form:

$$[\mathbf{G}_k^{\top}][\mathbf{u}_k] = [\mathbf{b}_L] \tag{3.63}$$

Now we can rewrite (3.56) as:

$$\begin{bmatrix} \mathbf{K}^{dd} & \mathbf{K}^{d\phi} & \mathbf{G} \\ \mathbf{K}^{d\phi\top} & \mathbf{K}^{\phi\phi} & \mathbf{0} \\ \mathbf{G}^{\top} & \mathbf{0} & \mathbf{0} \end{bmatrix} \begin{Bmatrix} \mathbf{d} \\ \boldsymbol{\phi} \\ \boldsymbol{\lambda} \end{Bmatrix} = \begin{Bmatrix} \mathbf{f^{ext}} \\ \mathbf{q^{ext}} \\ \mathbf{b}_L \end{Bmatrix} \tag{3.64}$$

The terms of the system Eq.(3.64) were defined in section 3.1.3.

3.2.2 Numerical example

Consider an $1\mu m \times 1\mu m$ simply supported domain containing an edge dislocation in the middle of the domain as shown in Fig.3.5.

The boundary is traction and surface charge free. Defining a two dimensional Cartesian coordinate system (x_1,x_3), the domain is $0 \leqslant x_1 \leqslant 1\mu m$ and $0 \leqslant x_3 \leqslant 1\mu m$. The glide plane is horizontal and follows along the direction of the line defined by $x_3 = 0.5\mu m$. The core is located at $(0.5\mu m, 0.5\mu m)$. The x_3 axis is chosen to be directed along the six fold axis of symmetry of a hexagonal piezoelectric crystal. Slip occurs along the basal plane with Burgers vector $a/3$, where $a = 4\mathring{A}$. Lead Zirconate Titanate(PZT-4) is the material considered for this example, and has the following properties that are taken from [127]; the elastic constants are $c_{11} = 13.9 \times 10^{10} Nm^{-2}, c_{12} = 7.78 \times 10^{10} Nm^{-2}, c_{13} =$

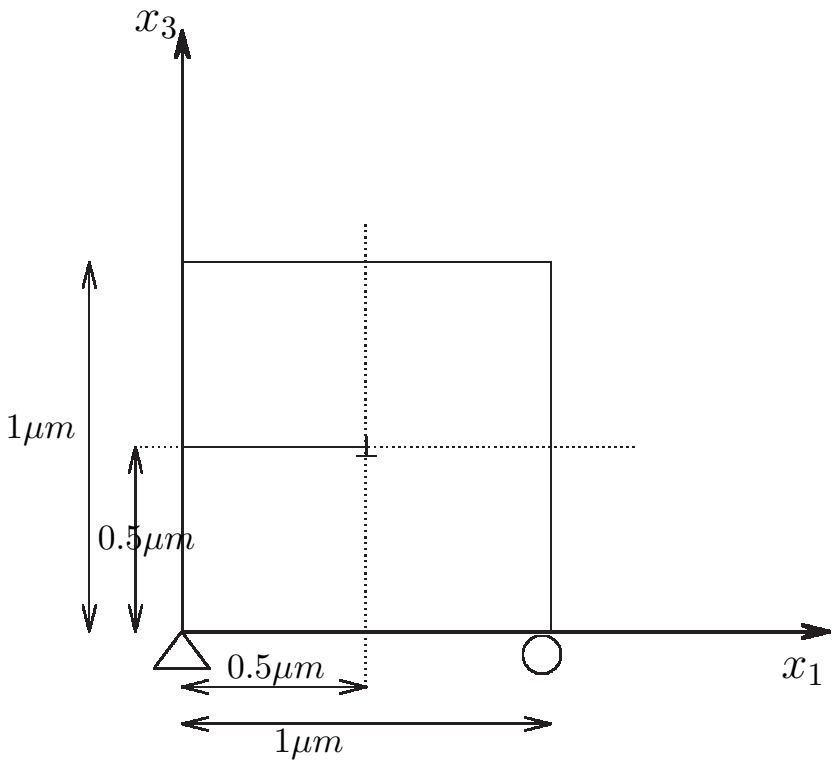

Figure 3.5: Edge dislocation in a simply supported domain [124].

$7.43\times10^{10}Nm^{-2}, c_{33} = 11.5\times10^{10}Nm^{-2}, c_{44} = 2.56\times10^{10}Nm^{-2}$; the piezoelectric constants are $e_{31} = -5.2Cm^{-2}, e_{33} = 15.1Cm^{-2}, e_{15} = 12.7Cm^{-2}$; the dielectric constants are $\varepsilon_{11} = 6.46 \times 10^{-9}FV^{-1}m^{-1}, \varepsilon_{33} = 5.62 \times 10^{-9}FV^{-1}m^{-1}$. The piezoelectric tensor corresponds to the crystal class 26 for which the poling direction was the same as the direction of the third axis, thus forming a positive coordinate system with (x_1,x_3) [96]. A uniform mesh with 100×100 quadrilateral elements is used.

The displacements and potential fields obtained using XFEM are identical to the solution that was obtained using standard FEM with Lagrange Multipliers, enforcing the

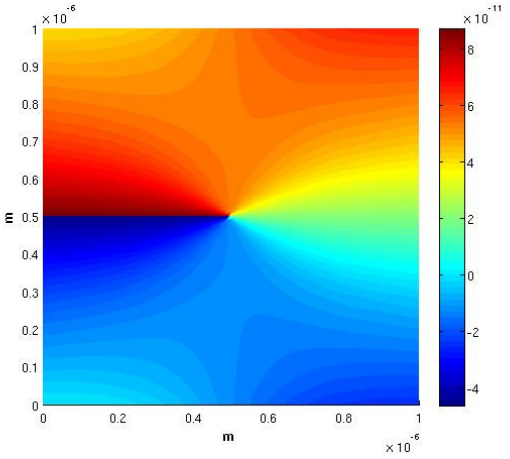

(a) FEM solution for displacement, m

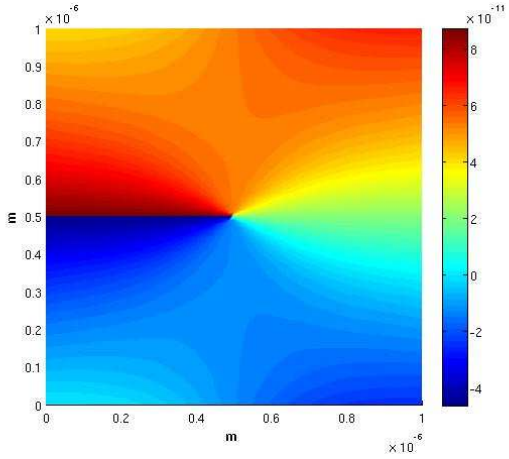

(b) XFEM solution for displacement, m

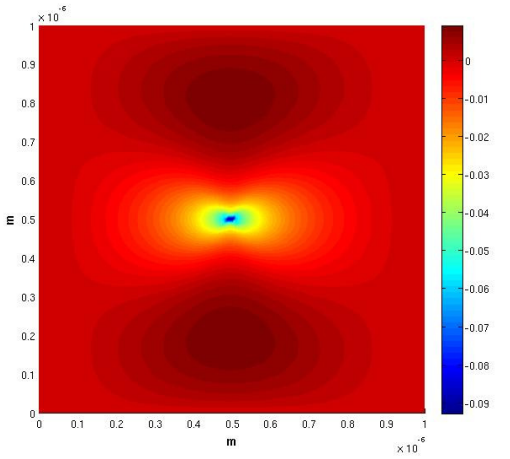

(c) FEM solution for potential, V

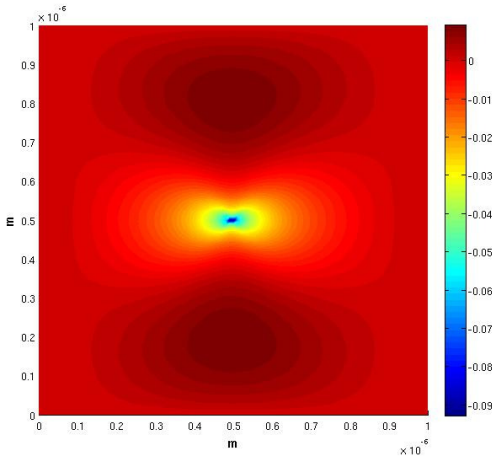

(d) XFEM solution for potential, V

Figure 3.6: Comparison of the FEM and XFEM solutions for a single stationary edge dislocation. a) Displacement in the x_1-direction using FEM. b) Displacement in the x_1-direction using XFEM. c) Potential using FEM. d) Potential using XFEM.

constraint Eq.(3.14) , see Fig.3.6 (a)-(d). In addition, the nodal values for the displacement and electric potential were compared to conclude that the FEM and XFEM solutions are equal. This agreement allows us to rely on the developed method with confidence.

Initial effort to validate the XFEM formulation focused on comparison to the analytical solution given in [128]. It was later discovered that this solution was erroneous and so an alternative method for validation was sought [124].

The FEM solution requires that element edges be aligned with the slip plane. For a single stationary edge dislocation with a horizontal slip plane this is a straight forward task. However, limitations of standard FEM become apparent, when applied to a domain which contains many moving dislocations of multiple slip planes. The standard FEM will become overly complex and computationally expensive, since a new mesh that aligns with all slip planes must be constructed at each step of the analysis. In this respect the XFEM model presented is greatly preferred.

3.3 Peach–Koehler force for the coupled electromechanical model

The next step towards the modeling the motion of the dislocation network is to calculate the driving force on each dislocation, or Peach–Koehler force. This force plays significant role when modeling the motion of the dislocations, since it directly effects the velocity of each dislocation and, therefore, the plastic deformation of the material.

As was previously mentioned in Sec.2.1.4 of Ch.2, the Peach–Koehler force can be calculated by two methods: (1) direct computation using the Peach–Koehler formula Eq.(2.2) and (2) by the contour integral Eq.(2.3). Due to the fact that we use the XFEM, where

the total stress is calculated, it is not possible to try to subtract the self stress and directly apply the Peach–Koehler formula to calculate the driving force on a dislocation [86]. Furthermore, when the singular core enrichment is not included in the displacement approximation as it is in this work, the total stress field becomes singular at the core. Thus, it is impossible to separate the stresses from other dislocations [87], and so the contour integral approach becomes necessary. Hence, we calculate the Peach–Koehler force by the contour integral for the static elastic continuum, as initially proposed by Eshelby Eq.(2.3) [32], and later extended to electrostatics by Pak and Herrmann [129], i.e.:

$$F_k = \oint_{\Gamma_c^\alpha} [H\delta_{jk} - u_{i,k}^\top \sigma_{ik} + D_j E_k] n_j d\Gamma_c^\alpha \tag{3.65}$$

where Γ_c^α is any closed contour about the dislocation α, and $\mathbf{n}$ is the unit outward normal to Γ_c^α. Here the potential energy density function, or so called the electric enthalpy density is [129]:

$$H = \frac{1}{2}\boldsymbol{\varepsilon}^\top : \mathbf{C} : \boldsymbol{\varepsilon} - \frac{1}{2}\mathbf{E}^\top \cdot \boldsymbol{\epsilon} \cdot \mathbf{E} - \boldsymbol{\varepsilon}^\top : \mathbf{e} \cdot \mathbf{E} \tag{3.66}$$

The main limitation of the contour integral is that the integral has to be taken over a domain that does not contain any other dislocation cores. In [86], the minimum radius of this contour is discussed. They showed that in order to obtain accurate Peach–Koehler forces, the mesh size must be smaller than one third of the distance separating two dislocation cores. This imposes a constraint on mesh coarseness and leads to very fine meshes in the vicinity of dislocation core. Constructions of such meshes is relatively straight forward since the mesh can be constructed independently of the location and orientation of the

slip planes. While not discussed in the present work, core enrichments as in [84] can also be introduced to allow for the use of much coarser meshes. However, the core enrichment functions are not always feasible for the anisotropic and nonlinear materials, whereas the enrichment in the form of Eq.(3.21) is applicable for modeling such materials.

3.3.1 Verification of the calculation of the Peach–Koehler force in the absence of electric field

In this section, we compare numerical calculation, referred in Eq.(3.65), with an analytical solution to verify accuracy of Peach–Koehler calculations. In the case of an edge dislocation in a semi-infinite domain near a free surface (see Fig.3.7) in the absence of electric effects ([130]), we have:

$$F = b^2\mu/L(4\pi(\nu - 1)) \tag{3.67}$$

where L is the distance from the dislocation core to the free surface. We adjusted our model for the isotropic material and the case of the plane strain. The following coefficients were used: Poisson's ratio $\nu = 0.34$; Lame coefficient $\mu = E/2(1 + \nu)$; Young's modulus $E = 1214.1$ GPa. The glide plane is parallel to x_1 and perpendicular to the free surface.

A domain of comparison was done for $L = 10h_e$, where $h_e = 10^{-2}\mu m$ is the element size. The difference in numerical calculations and the analytical solution was about 1.3%. It is considered as the convergence of the numerical and analytical results. If needed, the difference in the solutions could be reduced with decrease of element size.

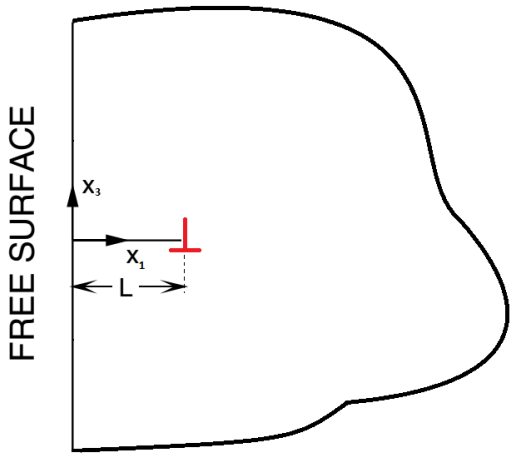

Figure 3.7: An edge dislocation in a semi-infinite domain, near free-surface

3.4 Piezoelectric effect of the Peach–Koehler force on a dislocation near free surface

In this section, we give an example that demonstrates the effect of the piezoelectric constants order on the dislocation driving force near a free-surface. We calculate the Peach–Koehler force by the contour integral Eq.(3.65). To demonstrate the piezoelectric effect on the Peach–Koehler force, we introduce the parameter γ into the constitutive laws. This parameter is a scaling factor used to adjust the magnitude of the piezoelectric tensor, which is coupling term between mechanical and electrical phenomenon. Thus, it is responsible for showing the influence of the electrical field in a coupled model on the stress field and the strain on the electric displacements, and so too on the Peach–Koehler force. To study

this effect we consider a constitutive model of the form

$$\boldsymbol{\sigma} = \mathbf{C} : \boldsymbol{\varepsilon} - \gamma \mathbf{e} \cdot \mathbf{E} \tag{3.68}$$

$$\mathbf{D} = \gamma \mathbf{e}^T : \boldsymbol{\varepsilon} + \boldsymbol{\epsilon} \cdot \mathbf{E} \tag{3.69}$$

In this example we have one edge dislocation and Γ_c^α is a circle of radius $r = 5h_e$, where $h_e = 10^{-2}\mu m$ is the element size.

Lead Zirconate Titanate(PZT-4) crystal is the material chosen to study, since it is often used in MEMS devices. Material size we use here is identical to that previously used to compare XFEM and FEM with Lagrange multipliers in Sec.(3.2.2). The material properties are also given in Sec.(3.2.2). An applied potential difference $\Delta\phi = 1$V is prescribed between the upper and lower surface, of the domain, as shown in Fig.3.8. Such applied voltage is typical for the piezoelectric materials like PZT-4. The electrical stress created by the voltage of such order eliminates the electric fatigue and failure of the sample [131]. A uniform mesh with 100×100 quadrilateral elements is used. The boundary is traction and surface charge free.

The parameter γ is varied from 0 to 1. The results are shown in Fig.3.9. In Fig.3.9(a) the Peach–Koehler force, F, was calculated at different distances, L, from the boundary for three values of parameter γ. The Fig.3.9(b) shows the relative change in the force with respect to the force calculated with no coupling effect, F_0, which corresponds to the parameter $\gamma = 0$. We also calculated the force for a dislocation in the middle of the domain,

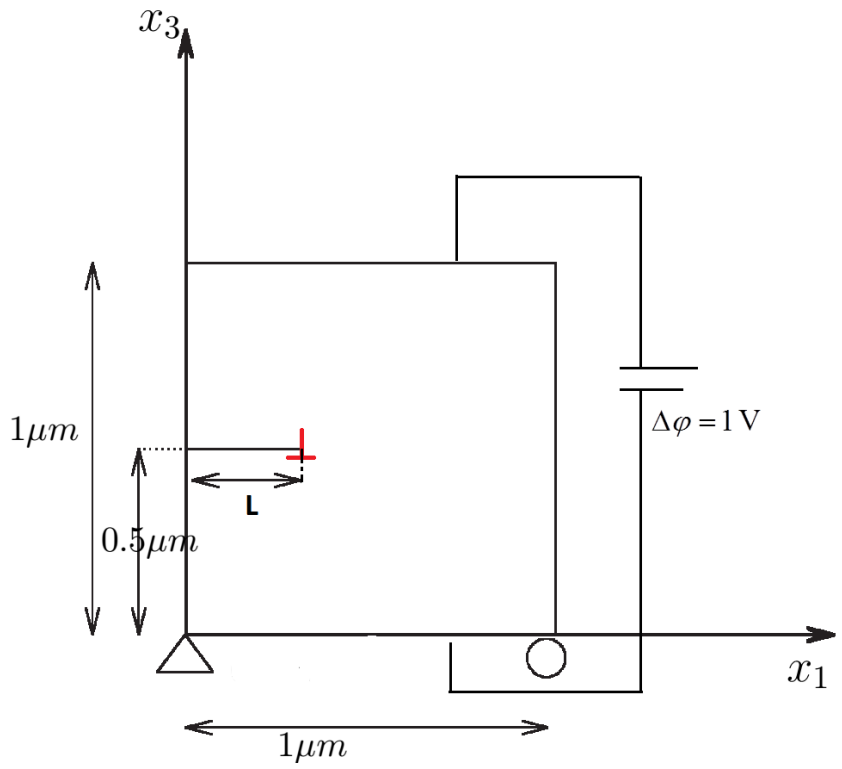

Figure 3.8: Edge dislocation in a simply supported domain under electrical load

where the Peach–Koehler force is expected to be zero, to verify our numerical calculation; it approaches zero as would be expected.

For PZT-4, which is known for its piezoelectric effect, $\gamma = 1$, the difference in the Peach–Koehler force for the coupled model is around 80% when a dislocation is $7h_e = 0.07\mu m$ from the boundary. Obviously, such large changes in Peach–Koehler force will effect the speed of the dislocation significantly. Similar electrical field influences were observed through experiments on the plastic deformation of metals and ceramics ([132]).

Even more interesting is the observation that the Peach–Koehler force changed direc-

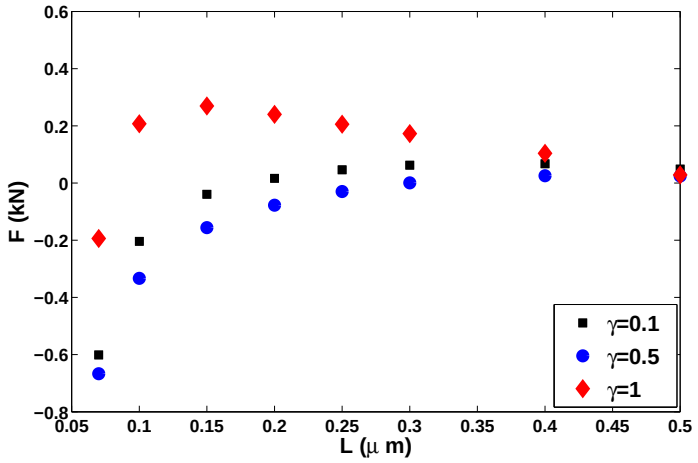

(a) Peach–Koehler Force for different γ

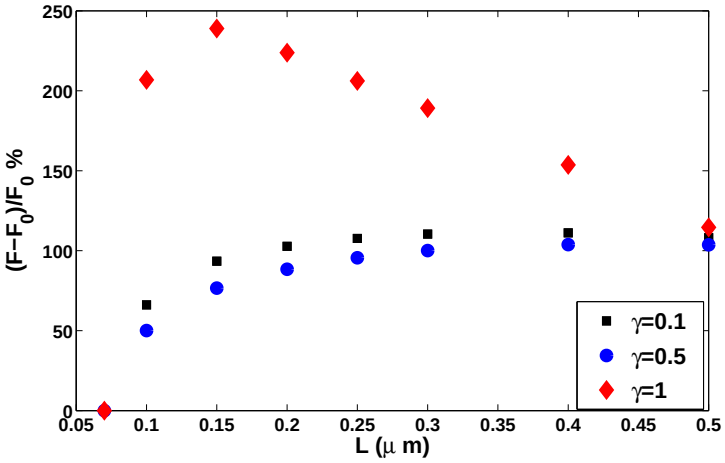

(b) Normalized Peach–Koehler Force for different γ

Figure 3.9: a) Peach–Koehler force for different γ at different distances from the boundary . b) Normalized Peach-Koehler force for different γ at different distances from the boundary [124].

tion when $L > 0.1\mu m$ for $\gamma = 1$. The electric field drives the dislocation towards the center of the domain, whereas the free surface boundary attracts the dislocation. The increasing/decreasing nature of the Peach–Koehler force is caused by the competition between

these processes. This suggests that while surface effects may still dominate dislocation behavior close to a free surface, the electromechanical coupling effect can dominate bulk behavior. In pure mechanical model, the curve would be monotonic. The discovery and quantitative representation of such an effect is very important when applied to the materials that usually are used in microelectrimechanical systems (MEMS). The behavior of these materials in existing theories is predicted by models that ignore coupling. We can see from the example that even in the case of a single dislocation, the effect of the electric field should be taken into account when dealing with materials that are under electrical and mechanical loads.

3.5 Phenomenological rules for the dislocation dynamics

The last step before we can model the motion of the dislocations is to define the rules and set up the laws that govern the dislocation nucleation, motion and evolution. We use a phenomenological equation of motion as in [5]:

$$\mathbf{F}^{\alpha} = \mathbf{B} \cdot \mathbf{v}^{\alpha} \tag{3.70}$$

where $\mathbf{v}^{\alpha}$ is the velocity of the dislocation α. $\mathbf{B}$ is the tensor of the dislocation drag or the inverse of the dislocation mobility tensor. Therefore, the next position of the dislocation α, $\mathbf{x}^{\alpha}_{next}$, can be calculated as:

$$\mathbf{x}^{\alpha}_{next} = \mathbf{x}^{\alpha}_{cur} + \mathbf{v}^{\alpha} dt \tag{3.71}$$

where $\mathbf{x}^{\alpha}_{cur}$ is the position of the dislocation α at the current moment and dt is the increment in time. The selection of dt was informed by the annihilation criterion, as this criterion imposes the strongest constraint on the time increment. Two edge dislocations with opposite Burgers vectors of the same magnitude will annihilate each other when they are within a material-dependent critical distance, L_{an} [19]. They annihilate, or cancel, each other because the distortion of one dislocation is exactly the negative of the other. In order to properly capture the dislocations annihilation, and to also capture when two dislocations pass each other without annihilating, the time increment is limited to

$$dt = \frac{1}{2}\frac{L_{an}}{\mathbf{v}^{\alpha}} \tag{3.72}$$

where $\mathbf{v}^{\alpha}$ is the maximum of all dislocations velocities, L_{an} is the the distance of annihilation.

We will restrict the motion to the glide plane, so $\mathbf{B} = B^{\alpha}\mathbf{b}^{\alpha}\otimes\mathbf{n}$. Here, $\mathbf{b}^{\alpha}$ is the Burgers vector of dislocation α, $\mathbf{n}$ is the normal to the glide plane and B^{α} is the drag coefficient of dislocation α.

New dislocations can be nucleated through the operation of Frank–Read sources. The source is characterized by the critical stress for activation of the Frank-Read mechanism,$\tau_{nuc} = \tau_{cr}$, the time to form a critical configuration, t_{nuc} and the diameter of the generated dislocation loop, L_{nuc}, see Fig.3.10 for the visualization of the nucleation process. The distance between two dislocations is taken to be such, so that the attractive force is balanced by

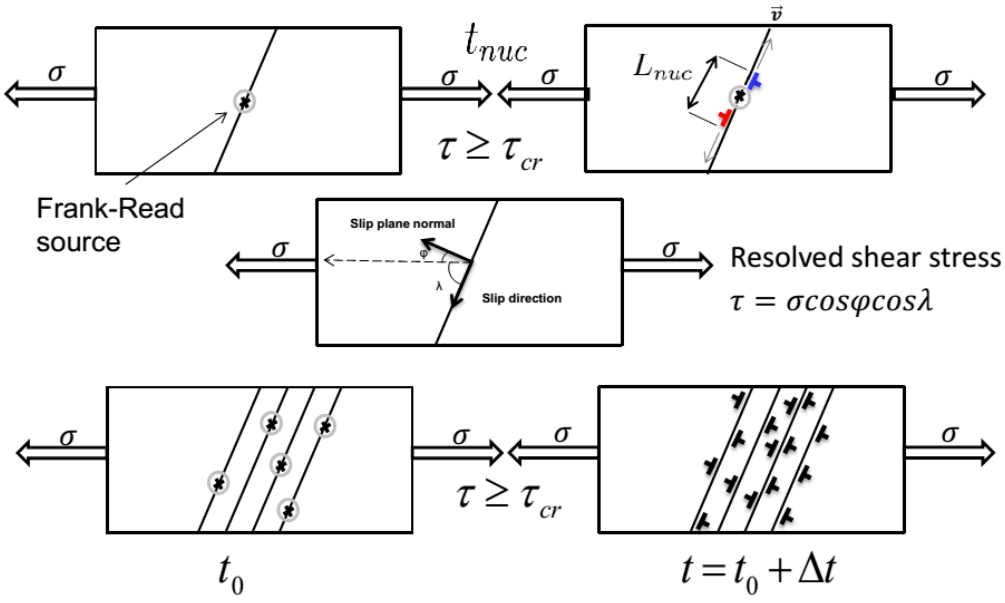

Figure 3.10: Nucleation of the network of the dislocations.

the internal stress in the absence of an electric field:

$$L_{nuc} = \frac{E}{4\pi(1-\nu^2)} \cdot \frac{b}{\tau_{nuc}} \tag{3.73}$$

where ν is Poisson's ratio, E is Young's modulus, and b is the magnitude of the Burgers vector [5]. The obstacles to dislocation motion are implemented through the pinning mechanism. Each obstacle, which could be, for example, a vacancy void or a precipitate, is modeled as a fixed point on a slip plane. When a dislocation reaches the vicinity of an obstacle, it becomes fixed and cannot glide further. Pinned dislocations get released by the obstacles when their Peach-Koehler force exceeds the pinning force of the obstacle, F_{obs} :

$$F_{obs} = \tau_{obs} \cdot b \tag{3.74}$$

where τ_{obs} is the strength of the obstacle.

3.6 Nucleation and motion of many dislocations

In this section, we use the developed coupled electromechanical XFEM model to study the motion of dislocations under electrical and mechanical loads. We demonstrate the importance of accounting for the multiphysical phenomena when modeling the materials in the presence of different nature loads.

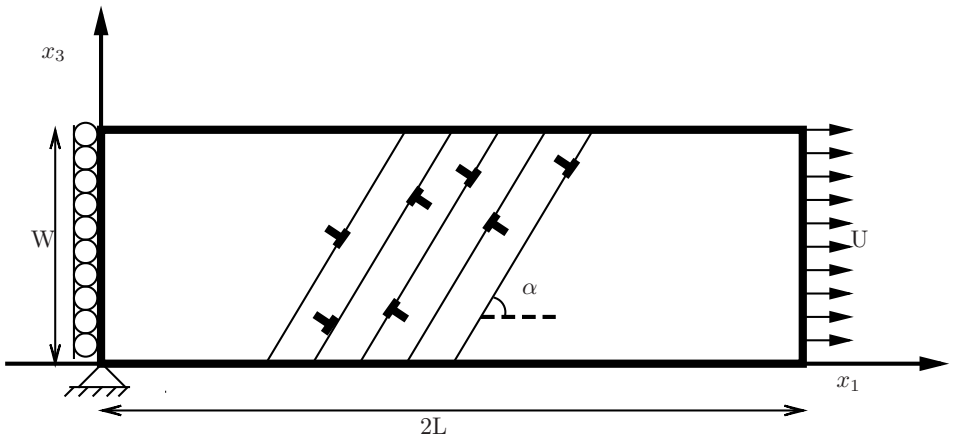

Figure 3.11: Single crystal specimen [124].

The single anisotropic crystal is used in our example to investigate the effect of piezoelectricity on the behavior of the dislocations, i.e. the plastic deformation. The geometry, elastic properties and boundary conditions that we use are similar to those in [133]. Plane strain conditions are assumed in the x_1–x_3 plane. The crystal has the following properties: Poisson's ratio $\nu = 0.33$, Young's modulus $E = 70GPa$; the piezoelectric constants are $e_{31} = -5.3 \times 10^{-3} Cm^{-2}, e_{33} = 15.5 \times 10^{-3} Cm^{-2}, e_{15} = 13.0 \times 10^{-3} Cm^{-2}$; the dielectric

constants are $\varepsilon_{11} = 6.37 \times 10^{-9} FV^{-1}m^{-1}, \varepsilon_{33} = 5.53 \times 10^{-9} FV^{-1}m^{-1}$. In this example, a material with piezoelectric constants similar to a lead zirconate titanate is considered [134]. One slip system at an angle of $\alpha = 60^{\circ}$ to the positive x_1 axis is considered. The slip planes are spaced $100b$ apart, where $b = 0.25nm$ is the magnitude of the Burgers vector of each edge dislocation. As in [135], we located the slip planes in the in the middle of the domain. As we mentioned in the previous Sec.3.5, Frank–Read source mechanism is used to nucleate new dislocations. The sources are randomly distributed on the slip planes with a density $\rho_{source} = 125\mu m^{-2}$. The nucleation strength, τ_{nuc}, is randomly assigned to each source using a Gaussian distribution with an average strength of $50MPa$ and standard deviation of $1MPa$. The nucleation time for the sources, t_{nuc}, is taken to be $2.5ns$. When the resolved shear stress exceeds the critical value, τ_{nuc}, during a time period of t_{nuc} a new dislocation dipole is generated. The obstacles are randomly distributed at the slip planes with a density of $\rho_{obs} = 30\mu m^{-2}$. The obstacle strength is set to be $\tau_{obs} = 150$ MPa [133]. The mobility constant B is $10^{-2} Pa \cdot s$. Annihilation of two dislocations with opposite signs occurs when they are by a distance $L_{an} = 8.5nm$. The crystal is dislocation and stress free at the beginning of simulation. A uniform mesh with 99×33 quadrilateral elements is used.

It is worth emphasizing, that two criteria are used to control the process of nucleation when the shear stress exceeds the critical value. To use only the constraint on nucleation time was not sufficient; the geometry of the dislocations had to be considered as well. The

next dipole is not nucleated unless the previous dipole has a critical distance from the source. We chose this distance to be big enough to accurately calculate the Peach–Koehler force around the dislocation cores, i. e. $4.24nm$.

We consider a specimen with dimensions $2L \times W$ with the tensile axis aligned with the x_1 direction, see Fig.3.11. In this example $L = 0.75\mu m$. Tension is imposed by prescribing displacements at $x_1 = 2L$ to be U and putting rollers along $x_1 = 0$. The loading rate $\dfrac{\dot{U}}{L} = 2000s^{-1}$ was used to obtain a strain of 0.005. To constrain rigid body motion of the specimen we fixed the displacements at the point $(0, 0)$. Applied potential differences $\Delta\phi = 1$V and $\Delta\phi = -1$V were prescribed between the upper and lower surfaces. As mentioned before, such applied voltage is typical for the piezoelectric materials like PZT-4. The electrical stress caused by this voltage prevents the electric fatigue and failure of the sample [131].

Fig.3.12 shows the tensile stress, σ, versus strain, U/L, responses of the specimen under applied potential of $\Delta\phi = -1$ and time step $dt = 0.5ns$ for different meshes. The mesh convergence study was performed to obtain an accurate solution with a mesh that is sufficiently dense and computationally efficient. The linear elastic response is identical for all meshes and is not shown. A 120×40 mesh is found to be sufficiently dense to capture the material response. A coarser mesh was chosen to qualitatively illustrate the effect of the electric field on the material response and dislocation density.

The tensile stress, σ, versus strain, U/L, responses of the specimen under different

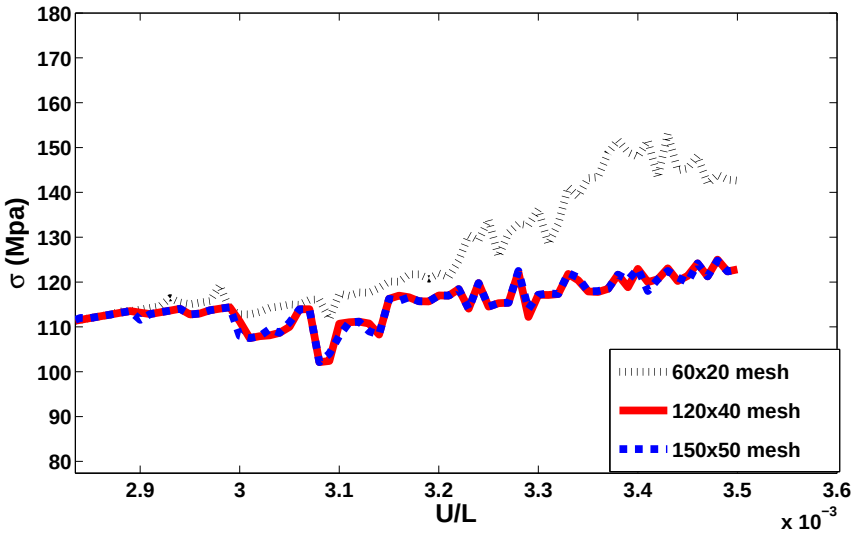

Figure 3.12: Mesh resolution sensitivity analysis

applied potentials are plotted in Fig.3.13(a). Evolution of the dislocation density, ρ_{disl}, with tensile strain is shown on Fig.3.13(b). The dislocation density is calculated as the amount of the dislocations per unit area. Since the slip planes are only located in the middle of the domain like in [135], all dislocation activity occurred in central area of the domain. Therefore, $\rho_{disl} = n_d/((2/3)L \times W)$, where n_d is the amount of dislocations at the current calculation step.

From Fig.3.13(a), we can see how the electrical field effects the response of the specimen. In both figures the linear elastic response is not shown. As we can see, in both cases the first dislocation activity occurs at the stress that is consistent with the critical value of the source strength at a strain of 0.3%. In the beginning of the dislocation activity, we observe a similar response, but with the increasing load the effect of the electric field

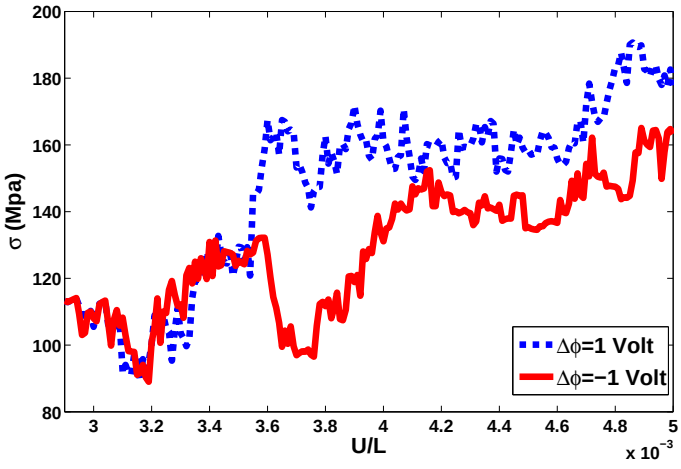

(a) The applied stress versus strain.

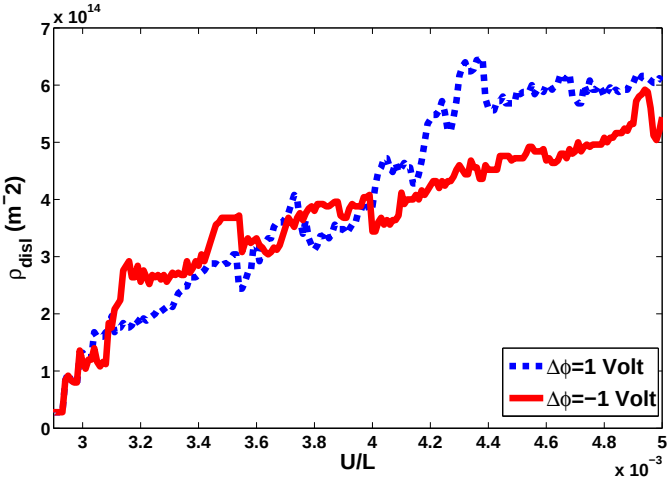

(b) Dislocation density at different tensile strain.

Figure 3.13: Tensile response for different applied electric potential difference [124]. a) The applied stress versus strain. b) Dislocation density at different tensile strain.

becomes clearly visible. The applied stress is generally higher for the case of $\Delta\phi = 1$V, meaning that the applied electric potential acts to oppose plastic deformations, whereas when $\Delta\phi = -1$V, the electric potential acts to drive plastic deformations. The maximum

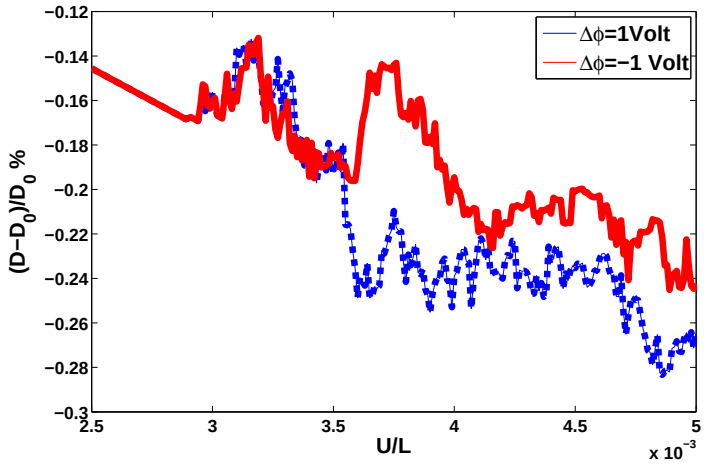

Figure 3.14: Rate of change of applied electric flux density versus applied strain [124]

difference in applied stress for the two considered cases reaches $65MPa$ at a strain of about 0.37%.

In Fig.3.13(b), the evolution of the dislocation density for the same two cases of applied potential difference is shown. We can see that the behavior of the dislocation densities for both cases is quite complex. It is interesting to note, that the point where the two dislocation density curves cross is near to where the difference in applied stress is at a maximum. At a strain of about 0.4%, the two curves depart from one another and do not cross afterwords.

In Fig.3.14, the percent change in the electric flux density, D, through the top surface with respect to initial electric flux density, D_0, is plotted against the applied strain for both cases. Here, we observe a significant change in the flux density for both cases beyond a strain of about 0.35%. The different behavior of a plastic zone is caused by the coupling

effect of this model. The maximum difference in electric flux for two cases is 0.12% and corresponds to the same strain where the maximum difference in the applied stress occurs. It is important to note, that if a material has stronger piezoelectric properties, the electrical effect is expected to be considerably more substantial.

The simulations in this section illustrate that the effect of the electric field on the material response is significant and needs to be carefully considered when dealing with electronic devices. The presented results are dependent on the location of randomly distributed Frank–Read sources and their randomly assigned strength. Differing origins and strengths may lead to slightly different results; however, the overall trends are expected to be unchanged. Such parameters like slip plane directions, the distribution and the number of dislocation sources, the source length, obstacle density and strength, and mobility constant are important when evaluating the performance of electronic small–scale devices ([136], [137], [138]). In the current calculations, we only permit dislocation activity on a single slip system. However, it is known that presence of the other slip system can influence the dislocation evolution on the initial one ([135], [139]). The inertia effects are assumed to be negligible in the presented formulation; however, it is a common assumption when modeling dislocation dynamics. The possible directions for the future improvement of this developed model are recommended in Ch.6.

3.6.1 Electromechanical XFEM-DD algorithm

The main computation steps for solving the coupled electromechanical problem using XFEM-DD are given below:

START:

compute $\mathbf{K}^{dd}$, $\mathbf{K}^{d\phi}$, $\mathbf{K}^{\phi\phi}$ from (3.31–3.33)

for each loading step from n to $nsteps$ **do**

compute $\mathbf{f}^{ext}$ using (3.37)

compute $\mathbf{q}^{ext}$ using (3.38)

compute $\mathbf{f}^{D}$ using (3.39)

compute $\mathbf{q}^{D}$ using (3.40)

compute $\mathbf{d}^{n}$ and $\boldsymbol{\phi}^{n}$ from (3.30)

compute Peach-Koehler force, $\mathbf{F}^{\alpha}$, for each dislocation α, using (3.65)

compute $\mathbf{v}^{\alpha}$ using (3.70)

update the position of each dislocation α on a slip plane

apply DD rules (nucleation, annihilation, pinning/unpinning, removing from the domain)

end for

END.

3.7 Concluding remarks

A discrete dislocation dynamics model based on the eXtended Finite Element Method was developed for a network of the dislocations under mechanical and electrical loads. In order to incorporate the effect of multiphysics, the equilibrium equation is coupled and solved together with Gauss' law. The discontinuity in the displacement field across the glide planes was modeled by introducing additional basis functions into the approximation. The calculation of the driving force on a dislocation was done using the J–integral. In the first example, the XFEM model for a domain with a single edge dislocation was verified by comparing with the solution obtained using the FEM with Lagrange Multipliers. In the second example, we illustrated the piezoelectric effect on the Peach–Koehler force on a dislocation near a free surface. The effect is significant and can affect both the direction and magnitude of the force. Moreover, this effect is seen to be very important in the bulk of a material. Lastly, the motion of many edge dislocations in a small domain under mechanical and electrical loads was simulated. The simulations demonstrated that for piezoelectric materials, the plastic response of the material considerably differs when various electric potential differences are applied and illustrates that the physics of plasticity under electromechanical load is more complex than in purely mechanical systems. The developed framework has great potential to be an important tool to study the behavior of the piezoelectric materials widely used in design of the micro-electro-mechanical system and other electronic devices.

Chapter 4

Thermomechanical dislocation dynamics model for high strain rate plastic deformation

The first fully coupled two–dimensional thermomechanical (TM) Discrete Dislocation Dynamics (DD) model is developed in this chapter. The model is based on the eXtended Finite Element Method (XFEM) and incorporates the equilibrium equations that is coupled with the heat conduction equation. This TM–XFEM–DD model bridges the gap between two scales, atomic- and micro-scale, incorporating thermal effects during high strain rate plastic deformation at the mesoscale.

The chapter has the following structure: in the first section, the strong and weak forms for the TM–XFEM-DD model that captures the heat generation effect and incorporates heat conduction are developed; the discrete equations are derived. In the second section, the calculation of the Peach–Koehler force in the presence of thermal effects is explained;

the temperature dependency of dislocation drag is introduced; the calculation of the body heat source is shown; dislocation dynamics phenomenological rules and computational steps are discussed. In the third section, the examples illustrating different plasticity induced thermal effects, including the effects of boundary condition of the heat equation, dislocation drag, and loading rate on plastic behavior of the DD are given. The chapter ends with concluding remarks in the forth section.

4.1 Theoretical formulation of the coupled TM–XFEM–DD model

In this section, the strong, weak, and discrete forms of the coupled thermomechanical system of the equations are derived.

4.1.1 Strong form of the coupled thermomechanical system

Consider a domain Ω bounded by Γ, as shown in Fig.4.1. The boundary Γ is decomposed into the sets Γ_u, Γ_T, $\Gamma_{\mathbf{t}}$, and Γ_h, such that:

$$\Gamma_u \cap \Gamma_{\mathbf{t}} = \emptyset \text{ and } \Gamma_u \cup \Gamma_{\mathbf{t}} = \Gamma \tag{4.1}$$

$$\Gamma_T \cap \Gamma_h = \emptyset \text{ and } \Gamma_T \cup \Gamma_h = \Gamma \tag{4.2}$$

The body Ω contains n_d dislocations. Let the active part of the slip plane of dislocation α be denoted by Γ_d^α. The core region Ω_d^α is the region where the strain energy is unbounded.

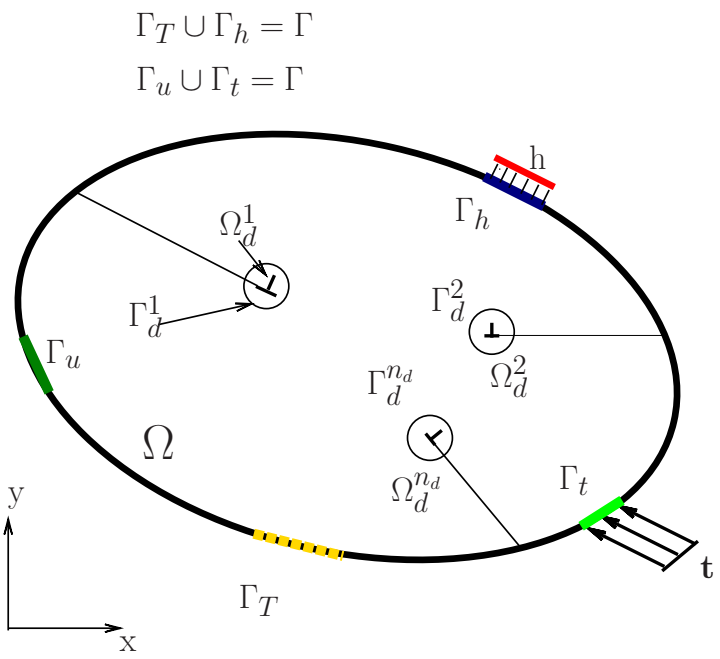

Figure 4.1: Domain definition and notation.

We denote $\Gamma_d = \cup_\alpha \Gamma_d^\alpha$ and $\Omega_d = \cup_\alpha \Omega_d^\alpha$, where α is from 1 to n_d. The strain energy in Ω/Ω_d is bounded.

The differential equations that govern the coupled thermomechanical dislocation dynamics model are the equilibrium equation and heat equation:

$$\nabla \cdot \boldsymbol{\sigma} + \mathbf{g} = 0 \tag{4.3}$$

$$C_p \rho \dot{\Theta} + \nabla \cdot \mathbf{q} = S \tag{4.4}$$

where $\boldsymbol{\sigma}$ is the Cauchy stress tensor, $\mathbf{g}$ is the body force vector, $\mathbf{q}$ is the heat flux density, $S = S(\mathbf{x}, t)$ is the body heat source, and $\Theta = \Theta(\mathbf{x}, t)$ is the absolute temperature change from the stress free reference temperature Θ_0 at the point $\mathbf{x} \in \Omega$ at the moment t. The

strain, $\boldsymbol{\varepsilon}$, can be expressed in terms of displacements $\mathbf{u}$ as:

$$\boldsymbol{\varepsilon} = \nabla_s \mathbf{u} \tag{4.5}$$

where ∇_s is the symmetric part of the gradient operator, see Eq.(3.9). The specific heat capacity and mass density are denoted by $C_p > 0$, and $\rho > 0$ respectively. The superposed dot denotes the material time derivative. The heat equation equation Eq.(4.4) is classified as a parabolic equation. The equilibrium equation Eq.(4.3) is classified as elliptical. However, the classification might not be important when the coupling through different constitutive dependencies is involved, as well as when dealing with numerical method of solving the partial differential equations.

The constitutive equation for the stress is:

$$\boldsymbol{\sigma} = \mathbf{C} : \boldsymbol{\varepsilon} - \boldsymbol{\lambda}\Theta \tag{4.6}$$

where $\mathbf{C}$ is the tensor of the elastic moduli, $\boldsymbol{\lambda} = \mathbf{C} : \boldsymbol{\gamma}$, and $\boldsymbol{\gamma}$ is the tensor of the coefficients of thermal expansion.

The constitutive equation for the heat flux, $\mathbf{q}$, is Fourier's law that was formulated empirically in 1822:

$$\mathbf{q} = -\mathbf{k}\nabla\Theta(\mathbf{x}, t) \tag{4.7}$$

where $\mathbf{k}$ is a symmetric tensor of the coefficients of thermal conductivity.

One unique feature of our thermomechanical dislocation dynamics model is the origin of the body heat source, $S(\mathbf{x}, t)$, in Eq.(4.4). This function is defined over the domain Ω, varies with time and coordinates, and represents the heat generated by the motion of the dislocations in the domain. Each dislocation acts as moving heat source. Thus, $S(\mathbf{x}, t)$ is a linear combination of dirac-delta functions:

$$S(\mathbf{x}, t) = \sum_{\alpha=1}^{nd} s_\alpha(t)\delta(\mathbf{x} - \mathbf{x}_\alpha(t)) \tag{4.8}$$

where $s_\alpha(t)$ is the heat generated by the motion of dislocation α at time t. The position, $\mathbf{x}_d^\alpha(t)$, is the position of dislocation α. The calculation of $s_\alpha(t)$ is discussed at greater length in Sec. (4.2). The coupled problem will be completed when appropriate boundary conditions are stated. The Dirichelet and initial boundary conditions are:

$$\mathbf{u} = \overline{\mathbf{u}} \text{ on } \Gamma_u \tag{4.9}$$

$$\Theta(\mathbf{x}, t) = \overline{\Theta} \text{ on } \Gamma_T \tag{4.10}$$

$$\Theta(\mathbf{x}, t_0) = T_0 \text{ in } \Omega \tag{4.11}$$

The Neumann conditions, where the surface traction $\mathbf{t}$ and heat flux h are imposed on applicable boundaries, are:

$$\boldsymbol{\sigma} \cdot \mathbf{n} = \mathbf{t} \text{ on } \Gamma_{\mathbf{t}} \tag{4.12}$$

$$\mathbf{q} \cdot \mathbf{n} = h \text{ on } \Gamma_h \tag{4.13}$$

In addition to the conditions above, the system is also subjected to the internal boundary

conditions:

$$[|\mathbf{u}|] = \mathbf{b}^{\alpha} \text{ on } \Gamma_d^{\alpha} \tag{4.14}$$

where $|\mathbf{u}|$ is the jump in the displacement across Γ_d^{α} and $\mathbf{b}^{\alpha}$ is Burgers vector of the dislocation α. The internal conditions come from the fact that Burgers vector represents the magnitude of a lattice distortion in the presence of the dislocation.

To summarize, the strong form of the coupled thermomechanical problem is:
find $\mathbf{u} \in \mathbf{C}^1(\Omega/\Gamma_d)$ and $\boldsymbol{\Theta}(\mathbf{x}, t) \in \mathbf{C}^1(\Omega) \cap \mathbf{C}^0(0 < t < \tau)$ such that equations (4.3) and (4.4) are satisfied under the conditions Eqs.(4.9)-(4.14).

Thus, the strong form of the coupled thermomechanical problem is stated by Eqs.(4.3)-(4.14).

4.1.2 Weak form of the coupled thermomechanical system

The weak form of the coupled thermomechanical system is derived from the strong form by following the standard procedure. We start by multiplying the governing equation (4.3) by an arbitrary function $\boldsymbol{\varsigma} \in \boldsymbol{\Sigma}$ and integrating over the domain Ω.

$$\int_{\Omega} \boldsymbol{\varsigma} \cdot \nabla \cdot \boldsymbol{\sigma} d\Omega + \int_{\Omega} \boldsymbol{\varsigma} \cdot \mathbf{g} d\Omega = 0, \forall \boldsymbol{\varsigma} \in \boldsymbol{\Sigma} \tag{4.15}$$

where

$$\boldsymbol{\Sigma} \;=\; \left\{ \boldsymbol{\varsigma} | \boldsymbol{\varsigma} \in \mathbf{H^1}(\Omega/\Gamma_d) \mid \boldsymbol{\varsigma} = 0 \text{ on } \Gamma_u \right\} \tag{4.16}$$

After integrating by parts, substituting the constitutive model for the stress (4.6), using (4.5) and boundary condition Eq.(4.12) we get:

$$\begin{aligned}&\int_{\Omega} \nabla \boldsymbol{\varsigma}^{\top} \cdot \mathbf{C} : (\nabla_s \mathbf{u}) d\Omega - \int_{\Omega} \nabla \boldsymbol{\varsigma}^{\top} \cdot \boldsymbol{\lambda} \Theta d\Omega = \\ &\int_{\Gamma_t} \boldsymbol{\varsigma}^{\top} \cdot \mathbf{t} d\Gamma + \int_{\Omega} \boldsymbol{\varsigma}^{\top} \cdot \mathbf{g} d\Omega, \forall \boldsymbol{\varsigma} \in \boldsymbol{\Sigma}\end{aligned} \tag{4.17}$$

Next, we choose an arbitrary weight function $\hat{v} \in \hat{\mathbf{V}}$, then we multiply the heat transfer equation (4.4) by it and integrate over the domain Ω:

$$\int_{\Omega} \hat{v} C_p \rho \dot{\Theta}(\mathbf{x}, t) d\Omega = \int_{\Omega} \hat{v} \mathbf{k} \nabla \Theta(\mathbf{x}, t) d\Omega + \int_{\Omega} \hat{v} S(\mathbf{x}, t) d\Omega, \forall \hat{v} \in \mathbf{W} \tag{4.18}$$

where

$$\hat{\mathbf{V}} \quad = \quad \left\{ \hat{v} | \hat{v} \in \mathbf{H^1}(\boldsymbol{\Omega}) | \hat{v} = 0 \text{ on } \Gamma_T \right\} \tag{4.19}$$

Further, integrating by parts and using the (4.13) give us:

$$\begin{aligned}&\int_{\Omega} w C_p \rho \dot{\Theta}(\mathbf{x}, t) d\Omega + \int_{\Omega} \nabla w \mathbf{k} \nabla \Theta(\mathbf{x}, t) d\Omega = \\ &\int_{\Omega} w S(\mathbf{x}, t) d\Omega - \int_{\Gamma_q} w h d\Gamma, \forall w \in \mathbf{W}\end{aligned} \tag{4.20}$$

Therefore, the weak form of the coupled thermomechancal problem is to find $\mathbf{u} \in \mathbf{H}^1(\Omega/\Gamma_d)$ and $\boldsymbol{\Theta}(\mathbf{x}, t) \in \mathbf{H}^1(\Omega) \cap \mathbf{H}^0(0 < t < \tau)$ such that the equations Eq.(4.17) and Eq.(4.20) are satisfied under the conditions Eqs. (4.9)-(4.14) for $\forall \boldsymbol{\varsigma} \in \boldsymbol{\Sigma}$ and $w \in \mathbf{W}$.

We defined the Sobolev space $\mathbf{H}^m$, where $m \in \mathbf{Z}$ by the Eq.(3.19) in Sec.3.1.2.

4.1.3 Discrete form of the coupled thermomechanical system

As we saw in Sec. 3.1.3, in the XFEM approach to dislocations dynamics, a standard local displacement approximation is extended by the discontinuities that dislocations create. We use level set functions to describe the locations of the active part of each slip plane like in [140, 84]. Edge dislocations are considered in our model. Each dislocation is described by the location of its core and the orientation and location of its glide plane. We define the glide plane of dislocation α by affine function $f^\alpha(\mathbf{x}) = 0$. The function is taken as the signed distance to the glide plane, i.e., $f^\alpha(\mathbf{x}) = \alpha_0 + \alpha_i \mathbf{x_i}$. The intersections of the glide plane $f^\alpha(\mathbf{x}) = 0$ with another plane $g^\alpha(\mathbf{x}) = 0$, defines the location of the core α. The affine function $g^\alpha(\mathbf{x}) = \beta_0 + \beta_i \mathbf{x_i}$ is defined as the signed distance to the core, such that $f^\alpha(\mathbf{x}) \perp g^\alpha(\mathbf{x})$. The active part of the glide plane is defined by $f^\alpha(\mathbf{x}) = 0,\ g^\alpha(\mathbf{x}) \leq 0$. See Fig.3.2 to visualize the level set definition of edge dislocation, since we used it in Sec. 3.1.3

The XFEM displacement approximation for a domain with n_d edge dislocations and Burgers vectors $\mathbf{b}^\alpha$ is:

$$\begin{aligned} \mathbf{u}^h(\mathbf{x}) = &\sum_{I \in S} N_I^u(\mathbf{x}) \mathbf{d}_I + \\ &\sum_{\alpha=1}^{n_d} \mathbf{b}^\alpha \sum_{J \in S^\alpha} N_J^u(\mathbf{x}) [H(f^\alpha(\mathbf{x})) - H(f^\alpha(\mathbf{x}_J))], \quad \forall \mathbf{x} \in \Omega / \Omega_d \end{aligned} \tag{4.21}$$

where N_I^u are the standard finite element shape functions, $\mathbf{d}_I$ are the nodal degrees of freedom, and $\mathbf{x}_J$ are the coordinates of node J. We denote S as the set of all nodes, and S^α as the set of enriched nodes. The enriched nodes are the nodes of the elements that

are completely cut by the active part of the glide plane as shown in Fig.4.2. The second term in Eq. (4.21) is called an enrichment and introduces the jump across the glide plane with magnitude and direction of the Burgers vector [141]. Though the displacement field approximation in (4.21) is discontinuous, the strain and stress fields are continuous, except at the dislocation core, see [142]. In Sec. 3.1.3 we showed how the slip across the glide plane is captured with such approximation Eq. (4.21). This slip is equal to the Burger's vector and is constant, which assures the continuity of the stress and strain fields across the glide plane.

The Heaviside step function is given by:

$$H(z) = \begin{cases} 1 & \text{if } z > 0 \\ \\ 0 & \text{otherwise} \end{cases} . \tag{4.22}$$

The temperature field is discretized over the domain Ω as follows:

$$\Theta^h(\mathbf{x}, t) = \sum_{I \in S} N_I^{\Theta}(\mathbf{x}) \Theta_I(t), \quad \forall \mathbf{x} \in \Omega \tag{4.23}$$

where N_I^{Θ} are the standard finite element shape functions and $\Theta_I(t)$ are time-dependent nodal temperature change.

Following Galerkin's method [125], the test functions, $\boldsymbol{\varsigma}(\mathbf{x})$ and $\hat{v}(\mathbf{x})$, are taken to be the same form as Eq.(4.21) and Eq.(4.23), respectively, i.e.:

$$\boldsymbol{\varsigma}(\mathbf{x}) = \sum_{I \in S} N_I^u(\mathbf{x}) \boldsymbol{\varsigma}_I + \sum_{\alpha=1}^{n_d} \sum_{J \in S^\alpha} N_J^u(\mathbf{x}) [H(f^\alpha(\mathbf{x})) - H(f^\alpha(\mathbf{x}_J))] \mathbf{a}^\alpha, \quad \forall \mathbf{x} \in \Omega \tag{4.24}$$

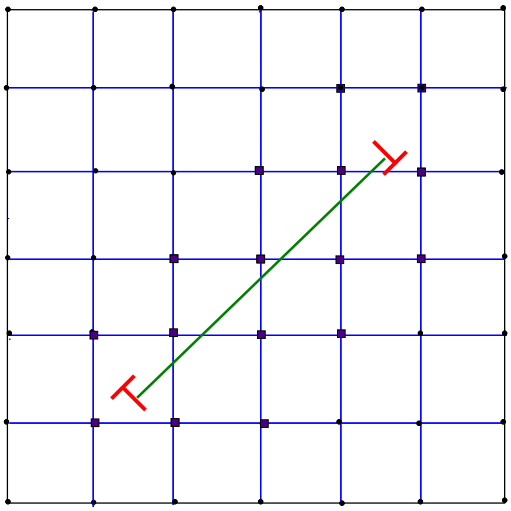

Figure 4.2: Illustration of the enriched nodes. Dark squares represent nodes in the S^α.

$$\hat{v}(\mathbf{x}) = \sum_{I \in S} \bar{N}_I^\Theta(\mathbf{x}) \hat{v}_I, \quad \forall \mathbf{x} \in \Omega \tag{4.25}$$

After substituting the approximations Eq.(4.21) and Eq.(4.23) and the corresponding approximations of the Galerkin's test functions Eq.(4.24)and Eq.(4.25) into the weak forms Eq.(4.17) and Eq.(4.20), recalling the arbitrariness of the nodal degrees of freedom $\boldsymbol{\varsigma}_I$, $\mathbf{a}^\alpha$, and $\hat{v}_I$, we obtain the following semi–discrete system of equations:

$$\begin{aligned} &\begin{bmatrix} 0 & 0 \\ 0 & \mathbf{C}^\Theta \end{bmatrix} \begin{bmatrix} \dot{\mathbf{d}} \\ \dot{\boldsymbol{\Theta}} \end{bmatrix} + \begin{bmatrix} \mathbf{K}^{dd} & \mathbf{K}^{d\Theta} \\ 0 & \mathbf{K}^{\Theta\Theta} \end{bmatrix} \begin{bmatrix} \mathbf{d} \\ \boldsymbol{\Theta} \end{bmatrix} = \\ &\begin{bmatrix} \mathbf{f}^{\mathbf{ext}} \\ \mathbf{q}^{\mathbf{ext}} \end{bmatrix} - \begin{bmatrix} \mathbf{f}^{\mathbf{D}} \\ \mathbf{q}^{\mathbf{TM}} \end{bmatrix} \end{aligned} \tag{4.26}$$

where $\mathbf{d} = [\mathbf{d}_1^\top, \mathbf{d}_2^\top, ...\mathbf{d}_n^\top]^\top$ are the standard displacement nodal degrees of freedom, $\boldsymbol{\Theta} =$

$[\Theta_1, \Theta_2, ...\Theta_n]^\top$ are the degrees of freedom that correspond to the time–dependent nodal temperature changes, and n is the number of the nodes. The vector $\mathbf{b} = [\mathbf{b}^{1\top}, \mathbf{b}^{2\top}, ...\mathbf{b}^{n_d\top}]^\top$ consists of a vector of Burgers, and n_d is the number of dislocations. In the DD model, the Burgers vectors are known at every step of the simulation.

The submatrices from the system of the equations Eq.(4.26) are:

$$\mathbf{K}_{IJ}^{dd} = \int_\Omega \mathbf{B}_I^{u\top} \mathbf{C} \mathbf{B}_J d\Omega, \quad I, J \in S \tag{4.27}$$

$$\mathbf{K}_{IJ}^{d\Theta} = \int_\Omega \mathbf{B}_I^{u\top} \boldsymbol{\lambda} \mathbf{N}_J^{\Theta} d\Omega, \quad I, J \in S \tag{4.28}$$

$$\mathbf{K}_{IJ}^{\Theta\Theta} = \int_\Omega \mathbf{B}_I^{\Theta\top} \mathbf{k} \mathbf{B}_J^{\Theta} d\Omega, \quad I, J \in S \tag{4.29}$$

$$\mathbf{C}_{IJ}^{\Theta} = \int_\Omega C_p \rho \mathbf{N}_I^{\Theta\top} \mathbf{N}_J^{\Theta} d\Omega, \quad I, J \in S \tag{4.30}$$

$$\mathbf{f}^{ext} = \int_{\Gamma_t} \mathbf{N}^{u\top} \mathbf{t} \, d\Gamma - \int_\Omega \mathbf{N}^{u\top} \mathbf{g} \, d\Omega \tag{4.31}$$

$$\mathbf{q}^{ext} = - \int_{\Gamma_h} \mathbf{N}^{\Theta\top} \, h \, d\Gamma \tag{4.32}$$

$$\mathbf{f}^D = \sum_{\alpha=1}^{n_d} \int_\Omega \mathbf{B}_I^{u\top} \mathbf{C} \mathcal{B}_\alpha^u \mathbf{b}^\alpha d\Omega, \quad I \in S \tag{4.33}$$

$$\mathbf{q}^{TM} = \int_\Omega \mathbf{N}^{\Theta\top} S(\mathbf{x}, t) \, d\Omega \tag{4.34}$$

where

$$\mathbf{B}_I^u = \begin{bmatrix} N_I^u(\mathbf{x})_{,x} & 0 \\ 0 & N_I^u(\mathbf{x})_{,y} \\ N_I^u(\mathbf{x})_{,y} & N_I^u(\mathbf{x})_{,x} \end{bmatrix} \tag{4.35}$$

$$\mathbf{B}_I^\theta = \begin{bmatrix} N_I^\Theta(\mathbf{x})_{,x} \\ N_I^\Theta(\mathbf{x})_{,y} \end{bmatrix} \tag{4.36}$$

$$\mathcal{B}_\alpha^u = \sum_{J \in S^\alpha} \begin{bmatrix} N_J^u(\mathbf{x})_{,x}\mathcal{H}_J^\alpha & 0 \\ 0 & N_J^u(\mathbf{x})_{,y}\mathcal{H}_J^\alpha \\ N_J^u(\mathbf{x})_{,y}\mathcal{H}_J^\alpha & N_J^u(\mathbf{x})_{,x}\mathcal{H}_J^\alpha \end{bmatrix} \tag{4.37}$$

and

$$\mathcal{H}_J^\alpha = H(f^\alpha(\mathbf{x})) - H(f^\alpha(\mathbf{x_J})) \tag{4.38}$$

Notice, that $\mathbf{K}^{dd}$, $\mathbf{K}^{d\Theta}$, $\mathbf{K}^{TT}$ and $\mathbf{C}^\Theta$ are independent of the location, number and geometry of the dislocations and, therefore, do not change for a given mesh as dislocations evolve.

The developed model captures the mechanical effect of the dislocations through $\mathbf{f}^D$ and the thermal effect of the dislocations with $\mathbf{q}^{TM}$.

4.1.4 Time integration scheme

We integrate Eq.(4.26) using the Crank-Nicolson sheme [143]. This algorithm has proven to be unconditionally stable for the heat equation [144]. In order to discretize the transient

term in (4.26), Taylor series are used, neglecting the second- and higher–order terms, which gives the first order accuracy in time approximation:

$$(\frac{\partial \mathbf{\Theta}^n}{\partial t}) \approx \frac{\mathbf{\Theta}^{n+1} - \mathbf{\Theta}^n}{\Delta t} + O(\Delta t) \tag{4.39}$$

where $n \in \{0, 1, ...N\}$, N is the total number of time steps, $\Delta t = \tau/N$. Isolating the time dependent variables from Eq.(4.26), we get:

$$\mathbf{C}^{\Theta}\dot{\mathbf{\Theta}} + \mathbf{K}^{\Theta\Theta}\mathbf{\Theta} = \mathbf{q}^{\mathbf{ext}} - \mathbf{q}^{\mathbf{TM}} \tag{4.40}$$

Now we introduce the parameter ϑ such that:

$$\mathbf{\Theta}^{n+\vartheta} = \vartheta\mathbf{\Theta}^{n+1} + (1-\vartheta)\mathbf{\Theta}^n \tag{4.41}$$

Substituting Eg.(4.41) into Eq.(4.40), using Eq.(4.39) and rearranging, we obtain:

$$\begin{gathered}(\mathbf{C}^{\Theta} + \vartheta\Delta t\mathbf{K}^{\Theta\Theta})\mathbf{\Theta}^{n+1} = (\mathbf{C}^{\Theta} - (1-\vartheta)\Delta t\mathbf{K}^{\Theta\Theta})\mathbf{\Theta}^n + \\ \Delta t(\vartheta(\mathbf{q}^{\mathbf{ext}} - \mathbf{q}^{\mathbf{TM}})_{\mathbf{n+1}} + (1-\vartheta)(\mathbf{q}^{\mathbf{ext}} - \mathbf{q}^{\mathbf{TM}})_{\mathbf{n}}\end{gathered} \tag{4.42}$$

The equation (4.42) gives the nodal values of the temperature change at the $n+1$ time level, using the n time level values. Both the $n+1$ and n time level values of the forcing vector $(\mathbf{q}^{\mathbf{ext}} - \mathbf{q}^{\mathbf{TM}})$ have to be known. By varying the parameter ϑ, different numerical schemes can be constructed. We chose parameter $\vartheta = 1/2$ which corresponds to the Crank-Nicolson sheme.

4.2 Thermomehcanical Dislocation Dynamics

In this section, the thermomechanical behavior of moving dislocations is described.

4.2.1 Peach–Koehler force

The Peach–Koehler force determines dislocation motion and, as we deliberated in Sec.3.3, in the case when the singular core enrichments are not included in the displacement approximation, should be calculated by a contour integral. The contour integral for the Peach–Koehler force has been extended to the case of two–dimensional thermoelasticity by Kishimoto and coworkers [145] and is given by:

$$F_k = \oint_{\Gamma_c^\alpha} [W - u_{i,k}^{\top} \sigma_{ik}] n_k d\Gamma_c^\alpha + \int_A \gamma_1 \sigma_{jj} \Theta_{,k} dA \tag{4.43}$$

where Γ_c^α is any closed contour about dislocation α, $\mathbf{n}$ is the unit outward normal to Γ_c^α, and A is the area bounded by Γ_c^α. For plane stress problems $\gamma_1 = \gamma$, whereas in case of plane strain $\gamma_1 = (1+\nu)\gamma$, where ν is Poisson's ratio. The elastic energy density W is defined by:

$$W = \frac{1}{2}(\sigma_{ij}(\varepsilon_{ij} - \delta_{ij}\gamma_1\Theta)) \tag{4.44}$$

The Peach–Koehler force represents the energy release rate. In the case of thermocoupling it consist of two integrals; an integral taken along a closed contour and a domain integral for the thermal contributions. The main limitation of the contour integral is that it has to be

taken over a domain that does not contain any other dislocation cores. In [86] the minimum radius of this contour is proposed. It was shown that in order to obtain accurate Peach–Koehler forces, the mesh size must be smaller than one third of the distance separating two dislocation cores. Even though this imposes a constraint on mesh coarseness in the vicinity of dislocation cores, it is not difficult to construct such meshes. This is due to the fact that in XFEM the mesh can be built independently of the location and orientation of the slip planes. However, as it was already discussed in Sec. 3.3, it is possible to use coarser meshes if core enrichments are introduced in displacement approximation like in [84].

4.2.2 Dislocation velocity and dislocation drag

We calculate the velocity $\mathbf{v}^\alpha$ of dislocation α from a phenomenological equation of motion

$$\mathbf{F}^\alpha = \mathbf{B} \cdot \mathbf{v}^\alpha \tag{4.45}$$

where $\mathbf{F}^\alpha$ is the Peach–Koehler force acting on dislocation α, and $\mathbf{B}$ is the tensor of the dislocation drag. The next position of each dislocation α, $\mathbf{x}^\alpha_{next}$ is determined using the Eq.(3.71) from Sec. 3.5. We will restrict the motion to the glide plane, so that $\mathbf{B} = B\mathbf{b}\otimes\mathbf{n}$. Here, $\mathbf{n}$ is the normal to the glide plane and B is the drag coefficient.

In order to incorporate the effect of mobility change with temperature, we represent the drag coefficient of each dislocation α as

$$B_\alpha = B_1\Theta_\alpha(t) + B_0;\ B_1 > 0 \tag{4.46}$$

where $\Theta_\alpha(t)$ is the temperature rise from the reference temperature Θ_0 at the location of the dislocation α at the moment t, and B_0 is the drag of the dislocation corresponding to the reference temperature. The parameter B_1 determines the rate at which the drag coefficient of each dislocation grows with increase of the temperature. It is the first time when such linear approximation of the dislocation drag is incorporated in dislocation dynamics. By varying B_1 we can study the effect of the temperature through the drag coefficient on material response. In general each dislocation in our model will be subject to a different drag.

We based the suggestion of Eq.(4.46) on the phonon drag mechanism, where the drag coefficient, B, is linearly proportional to temperature, T [121]. This mechanism is considered as dominant, except at very low temperatures, and takes the form [121]:

$$B \cong (kT/\mathbf{\Omega} \cdot \omega_a) \tag{4.47}$$

where k is the coefficient of thermal conductivity, ω_a is the atomic frequency, and $\mathbf{\Omega}$ is the atomic volume.

Several studies have been made validating such an assumption. It was experimentally confirmed that the drag increase with temperature can be well approximated by a linear function when the temperature is above 250 K [120, 146]. In addition to experimental works, such linear dependency was observed in recently conducted DD simulations (Fig.1 of [109]). With temperature rises attributable to shear bands, the drag coefficient can double in magnitude [147]. However, when the velocities of the dislocations exceed the

speed of sound, dislocation-phonon interactions become more complex and a different drag mechanism is involved [148].

4.2.3 Heat source calculation

In order to calculate the heat, $s_\alpha(t)$, generated by each moving dislocation α, we calculate the rate of work done by the Peach–Koehler force on the dislocation, i.e.:

$$s_\alpha(t) = \beta \left(\mathbf{F}^\alpha(t) \cdot \mathbf{v}^\alpha(t)\right) = \beta \, \frac{\mathbf{F}^\alpha(t) \cdot \mathbf{F}^\alpha(t)}{B_\alpha(\Theta_\alpha(t))} \tag{4.48}$$

where $\mathbf{F}^\alpha$ is the Peach–Koehler force on dislocation α, $\mathbf{v}^\alpha$ is the velocity of the dislocation α, and B_α is the drag of dislocation α. We assume that at the initial moment of the simulations, the rate of work is zero due to the absence of the dislocation motion.

The coefficient β is introduced to represent the fraction of the work that is converted into heat. There are studies using continuum models where the amount of plastic work converted into heat is found to be dependent on strain and strain rate [115]. However, it is more common to use a constant ratio of plastic work converted into heat to be a constant between 0.8 and 1, which is independent of strain and strain rate[149, 150]. Values of β, $0 \leq \beta \leq 1$ may be introduced to discount the heat generated by a moving dislocation, due to the emission of phonons or other physical phenomena not incorporated directly into the XFEM-DD model.

4.2.4 Nucleation, annihilation and pinning of the dislocations

We use the same phenomenological rules for the dislocation dynamics like in Sec. 3.5. A two dimensional Frank–Read sources mechanism to create a new dislocation dipole, similar to [5]. The source is defined by a critical resolved shear stress, or nucleation strength, τ_{nuc}^{FR}, for activation of the mechanism, the length of the dislocation loop, L_{nuc}^{FR}, which is a distance between dislocations of the dipole, and the time to form a critical configuration, t_{nuc}.

The pinning mechanism is implemented through the obstacles to dislocation motion. Obstacles release pinned dislocations if the Peach–Koehler force on it surpasses the pinning force of the obstacle, F_{obs}.

4.2.5 Thermomechanical XFEM-DD algorithm

The main computation steps for solving the coupled thermomechanical problem using XFEM-DD are given below:

START:

compute $\mathbf{K}^{dd}$, $\mathbf{K}^{d\Theta}$, $\mathbf{K}^{TT}$ and $\mathbf{C}^{\Theta}$ from (4.27–4.30)

enforce Initial Conditions Eq.(4.11) and calculate $\boldsymbol{\Theta_0}$

for each time step from n to $nsteps$ **do**

compute $\mathbf{q}^{ext}$ using (4.32)

compute $\mathbf{f}^{ext}$ using (4.31)

compute $\mathbf{f}^{D}$ using (4.33)

compute $\mathbf{q}^{TM}$ using (4.34)

compute $\mathbf{\Theta}^n$ and $\mathbf{d}^n$ from (4.26)

compute $\mathbf{F}^\alpha$ using (4.43)

update B^α using (4.46) given $\mathbf{\Theta}^n$

compute $s_\alpha(t)^n$ using (4.48) given $\mathbf{F}^\alpha$ and B^α

compute $\mathbf{v}^\alpha$ using (4.45)

compute updated position of each dislocation, $\mathbf{x}_\alpha^n$

apply DD rules (nucleation, annihilation, pinning/unpinning, removing from the domain)

end for

END.

4.3 Simulation results and parametric studies

Consider a two–dimensional specimen with dimensions $L \times W$ with the tensile axis aligned with the x_1 direction, see Fig.4.3. In this example $L = 1.5\mu m$ and $W = 0.5\mu m$. Tension is imposed by prescribing the load on the boundary $x_1 = L$ in the x_1 direction. A time step $12.5ns$ was used. To constrain rigid body motion of the specimen, we fixed the displacements at the point $(0, 0)$ and put rollers along $x_1 = 0$. Initial change in temperature is $T_0 = 0$ K. Plane strain conditions are assumed. We chose to model the face–centered cubic crystal of copper-like material with the following well known properties: thermal

conductivity, k = 385 $W/(m \cdot K)$; material density, ρ = 8960 kg/m^3; mass specific heat capacity: C_p = 385 J/(kg K); elastic modulus, E =$117 \cdot 10^9$ Pa; Poisson's ratio: ν= 0.36; coefficients of the linear thermal expansion, $\gamma = 17 \cdot 10^{-6}$ 1/K.

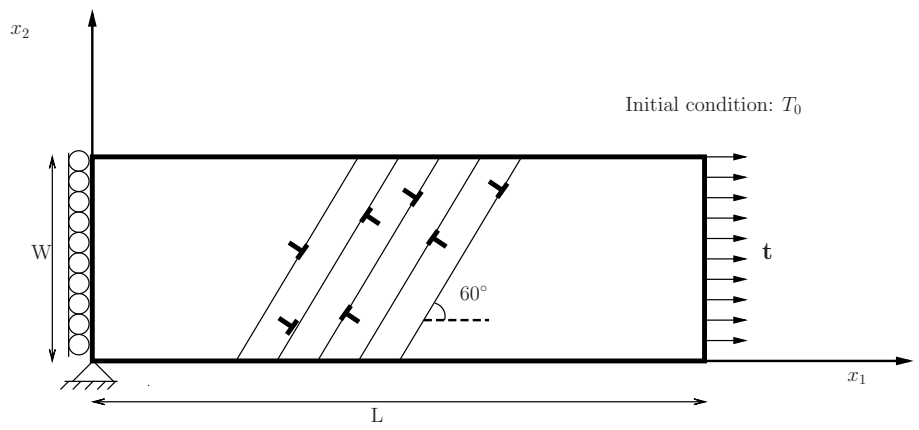

Figure 4.3: Single crystal specimen and boundary conditions

For simplicity, we only consider one slip system orientated at an angle of $\alpha = 60°$ to the positive x_1 axis, as in [135]. The Frank–Read sources are randomly distributed on slip planes with a density of $\rho_{src} = 125\mu m^{-2}$. The slip planes are spaced $100b$ apart, where $b = 0.25nm$ is the magnitude of the Burgers vector. The nucleation strength, τ_{nuc}^{FR}, is randomly assigned to each source using a Gaussian distribution with an average strength of 50 MPa and standard deviation of 1 MPa. The nucleation time, t_{nuc}, for a new dislocation dipole to be generated by a source is $62.5ns$. The length of the dislocation loop, L_{nuc}^{FR}, is approximated by:

$$L_{nuc}^{FR} = \frac{E}{4\pi(1-\nu^2)} \cdot \frac{b}{\tau_{nuc}^{FR}} \tag{4.49}$$

which neglects thermal effects [5]. The obstacles are randomly distributed at the slip planes with a density of $\rho_{obs} = 30\mu m^{-2}$. The obstacle strength is set to be $\tau_{obs} = 150$ MPa [133]. When the Peach–Koehler force on obstacle exceeds $\tau_{obs}b$ the dislocation becomes mobile again. Annihilation of two dislocations with opposite signs occurs when they are separated by a distance $L_{an} = 8.5nm$.

Fig.4.4 shows the stress-strain curve at loading rate $0.12MPa \cdot ns^{-1}$ and time step $dt = 12.5ns$ for different meshes. The dislocation drag is taken to be constant and equal to $10^{-4}\ Pa \cdot s$. This mesh convergence study was performed to obtain an accurate solution with a mesh that is sufficiently dense and computationally efficient. A 60×20 mesh is found to be a mesh when the results converge, as shown in Fig.4.4. The selection of time step was informed by the annihilation criterion, as this criterion imposes the strongest constraint on the time increment, dt. The Eq.(3.5) was used to calculate dt. The Crank–Nicholson scheme was used to integrate the heat equation in time. This scheme is unconditionally stable; therefore, no additional requirements were imposed on the time increment.

4.3.1 Effect of boundary conditions

In this section, the effects of the boundary conditions of the heat equation on plastic behavior of the DD model are studied. Two types of boundary conditions are considered (a) flux free boundary or adiabatic and (b) no temperature change on the boundary, corresponding to $\mathbf{q} \cdot \mathbf{n} = 0$ and $\Theta(\mathbf{x}, t) = 0$ on Γ respectively. We imposed tension $\mathbf{t} = \boldsymbol{\sigma} \cdot \mathbf{n}$, such that

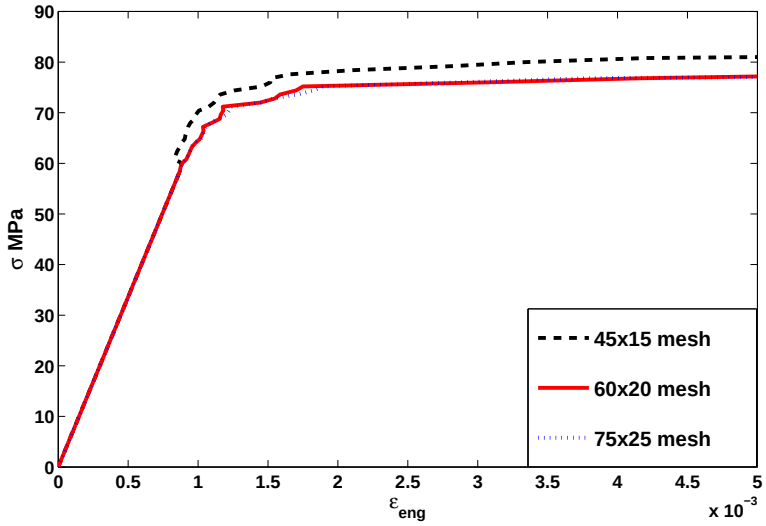

Figure 4.4: Mesh resolution sensitivity analysis.

$\dot{\sigma} = 0.24$ MPa$\cdot ns^{-1}$.

The temperature distributions for the boundary conditions (a) and (b) at a strain of 0.002 are given in Fig.4.5 and Fig.4.6, respectively. In the case of zero heat flux on the boundary, we observe close to a uniform temperature distribution over the domain. The high conductivity of the material enhances this behavior of the temperature field. In the case of no temperature change on the boundary, the heated zone is localized in middle of the domain where high dislocation activity occurs. In both cases, the temperature rise is significant and reaches up to 600 K at the reported strain value.

The corresponding stress-strain curves are shown in Fig.4.7. The response of the material, neglecting thermal effects, is shown for comparison in the same figure. Evidently,

neglecting thermal effects leads to underestimating the softening in the plastic zone by at least 50 MPa. Such significant softening due to rapid heat generation remains underestimated by existing thermally modified theories [151]. The stress–strain behavior of the adiabatic simulations is softer that that of the no temperature change on the boundary $\bar{\Theta} = 0$ simulation. Much of the difference in the stress-strain behavior comes from difference in the amount of thermal expansion between the two cases. Similar softening behavior due to increase in thermal expansion was reported by Tang et. al. [109].

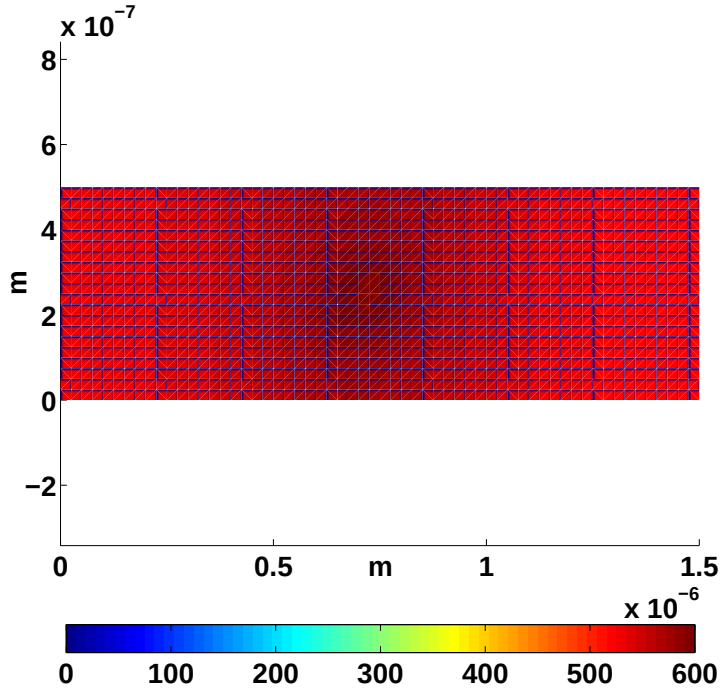

Figure 4.5: Temperature rise distribution in K over the domain under Neumann conditions.

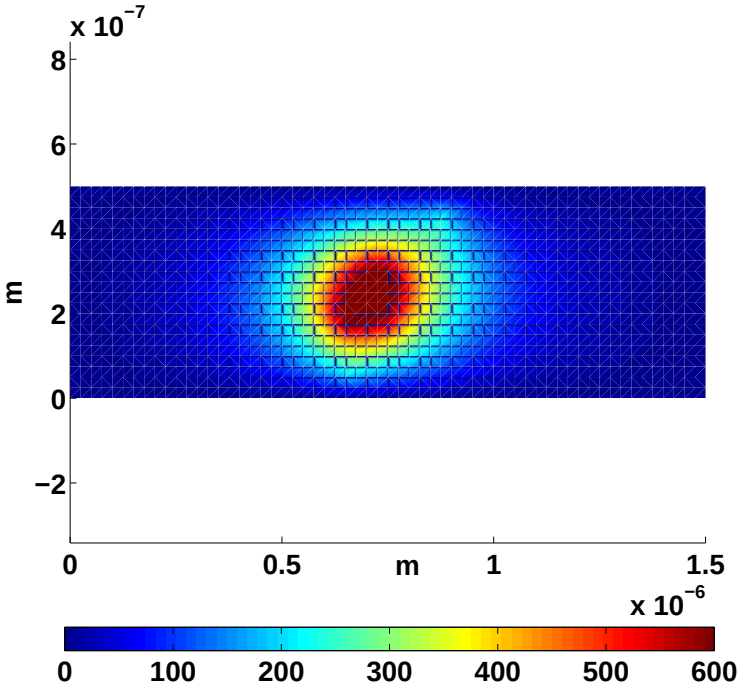

Figure 4.6: Temperature rise distribution in K over the domain under Dirichlet conditions.

4.3.2 Effect of dislocation drag

In this section, the effect of the parameter B_1 is studied. B_0 is set to 10^{-4} $Pa \cdot s$ [5]. To study the role of the temperature dependence of the dislocation drag coefficient, B_1 in (4.46) was taken to be 0, $0.5 \cdot 10^{-7}$, 10^{-7} $(Pa \cdot s)/K$. We based the choice of B_1 range values on the results of two experimental works, Fig.7 in [120] and Fig.5 in [148], where dislocation drag was measured as a function of temperature. Two sets of simulations were performed at different loading rates, one at a loading rate of $\dot{\sigma} = 0.12$ MPa$\cdot ns^{-1}$ (yielding a strain rate of $\dot{\varepsilon} = 5.6 \cdot 10^3 s^{-1}$ at $\boldsymbol{\varepsilon} = 0.002$) and one at $\dot{\sigma} = 0.24$ MPa$\cdot ns^{-1}$ ($\dot{\varepsilon} = 1.1 \cdot 10^4 s^{-1}$ at

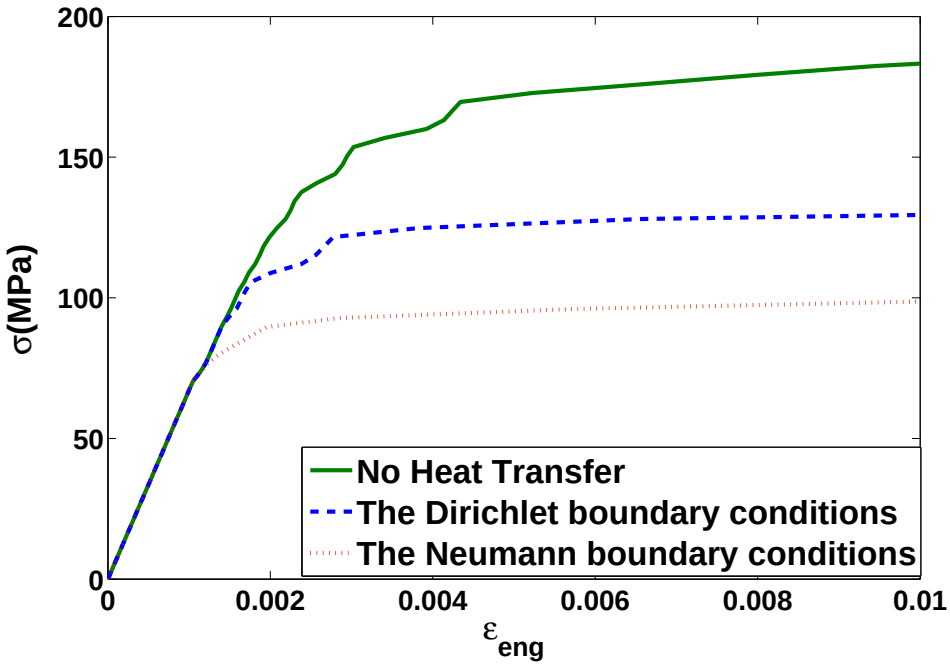

Figure 4.7: Stress vs. Strain for different boundary conditions on the heat equation.

$\varepsilon = 0.002$). The results are presented in Fig. 4.8 and Fig.4.9. The response of the material without thermocoupling is also shown in both figures to demonstrate the softening behavior in the presence of thermal effects. The temperature change on the boundary was fixed to $\bar{\Theta} = 0$ K for all the simulations here and in the following section.

The temperature dependence of dislocation drag does not have a significant effect on the stress-strain response of the specimen at a lower loading rate. However, B_1 has a noticeable effect in the case of the higher loading rate. The increase of dislocation drag with temperature causes thermal hardening. The larger B_1, the more drag a dislocation will experience at a given temperature, leading to lower dislocation velocities. When

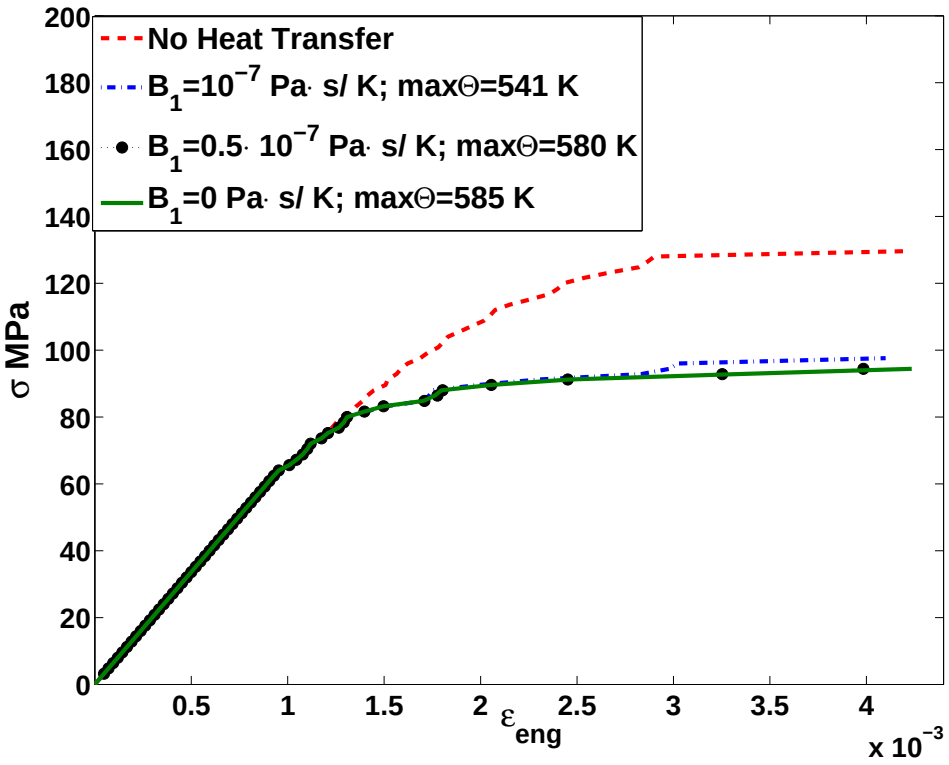

Figure 4.8: The stress-strain curve for the initial drag $B_0 = 10^{-4} Pa \cdot s$ at the loading rate $\dot{\sigma}$=0.12 MPa $\cdot ns^{-1}$.

dislocation velocities are lower, then less heat is generated for the same Peach–Koehler force. The maximum temperature rise for each simulation is also reported in Fig. 4.8 and Fig.4.9, where it can be observed that increasing B_1 leads to more hardening and a lower maximum temperatures.

We observe the most softening when $B_1 = 0$, which corresponds to the simulation with the most generated heat. Our model is in qualitative agreement with the results obtained by Zirelli et al. in [123], where they showed that the effect of constant dislocation drag is

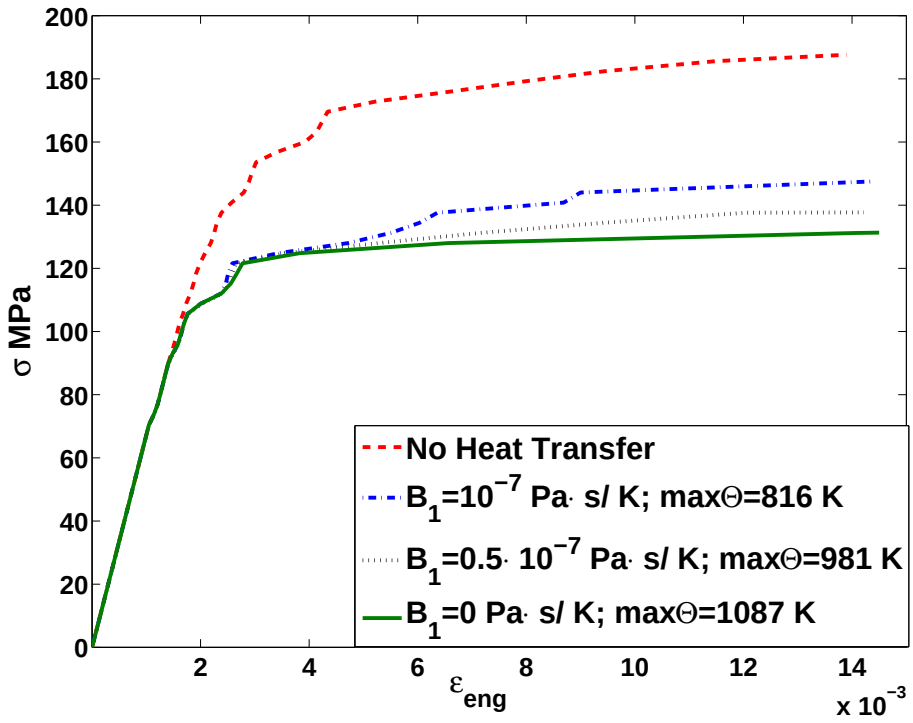

Figure 4.9: The stress-strain curve for the initial $B_0 = 10^{-4} Pa \cdot s$ at the loading rate $\dot{\sigma}$=0.24 MPa $\cdot ns^{-1}$.

negligible at strain rate of $10^3 s^{-1}$ and is significant at a strain rate of $2 \cdot 10^3 s^{-1}$.

4.3.3 Effect of loading rate

In this section, the effect of the loading rate on plastic deformation is studied, both with and without thermomechanical coupling. Loading rates of $0.06 MPa \cdot ns^{-1}$, $0.12 MPa \cdot ns^{-1}$, $0.24 MPa \cdot ns^{-1}$, and $0.32 MPa \cdot ns^{-1}$ are studied. The strain rate at strain of $2 \cdot 10^{-3}$ is given for the corresponding loading rate in Table 4.1.

The former case is shown in Fig.4.10, and demonstrates how an increase in the loading

Loading rate, $\dot{\sigma}$ (MPa$\cdot ns^{-1}$)	Strain rate, $\dot{\varepsilon}$ (s^{-1})
0.06	$9.1 \cdot 10^2$
0.12	$5.6 \cdot 10^3$
0.24	$1.1 \cdot 10^4$
0.32	$4.8 \cdot 10^4$

Table 4.1: The strain rates at strain $\epsilon = 2 \cdot 10^{-3}$ for the corresponding loading rates.

rate leads to an increase in the flow stress, as observed in experiments [152]. This trend is also consistent with effect of the Zener-Hollomon parameter on copper experimentally studied in [153]. The latter case is shown in Fig.4.11 where the flow stress increases with increasing loading rate, but the overall response is softer. Furthermore, we observe that the loading rate significantly influences the magnitude of the localized temperature rise. The maximum temperature rise is reported in Fig.4.11 and varies from 489K for a loading rate of $0.06 MPa \cdot ns^{-1}$ to 1131K for a loading rate of $0.32 MPa \cdot ns^{-1}$. The temperature rises observed in these simulations are of the same order as those reported in experimental studies of high strain rate plasticity [110, 154]. The observed response is attributed to the increase deformation rate, thus causing an increase in the rate of heat generation that exceeds the rate of increase in heat conduction.

The developed DD model targets high strain rate plastic deformations; however, we have neglected inertial forces in our governing equations, which is a common assumption in DD. Such limitation was recently discussed in a dislocation dynamics study, where it was pointed out to have only limited impact when the dynamics are governed by dislocation

generation and annihilation [109]. However, at high loading rates this assumption may be invalid and requires further investigation before it can be considered conclusive.

The presented results are dependent on location of randomly distributed Frank–Read sources and their randomly assigned strength which means that a different distribution of the sources and their strength may lead to slightly different results. Nonetheless, the overall trends are expected to be unchanged.

Simulations were carried out with strain rates which are commonly used in DD, whereas the typical experimental strain rates are of the order of 10^{-3} to $10^{-4}\,s^{-1}$; which makes the direct comparison with simulations challenging. However, the observed softening behavior and temperatures rises are consistent with the expected trends and observations from other DD studies [10, 109, 155].

4.4 Concluding remarks

The first fully coupled two–dimensional thermomechanical dislocation dynamics model based on eXtended Finite Element Method was developed. The distinct feature of this model is that the equilibrium equations are coupled with the heat equation, where the heat source is a function of the work done by the motion of dislocations. The work done by each moving dislocation is calculated using the Peach–Koehler force and dislocation velocity at every step of the simulation. The results of our simulations showed that during high rate deformation, common in DD, the significant local heating is present. Further-

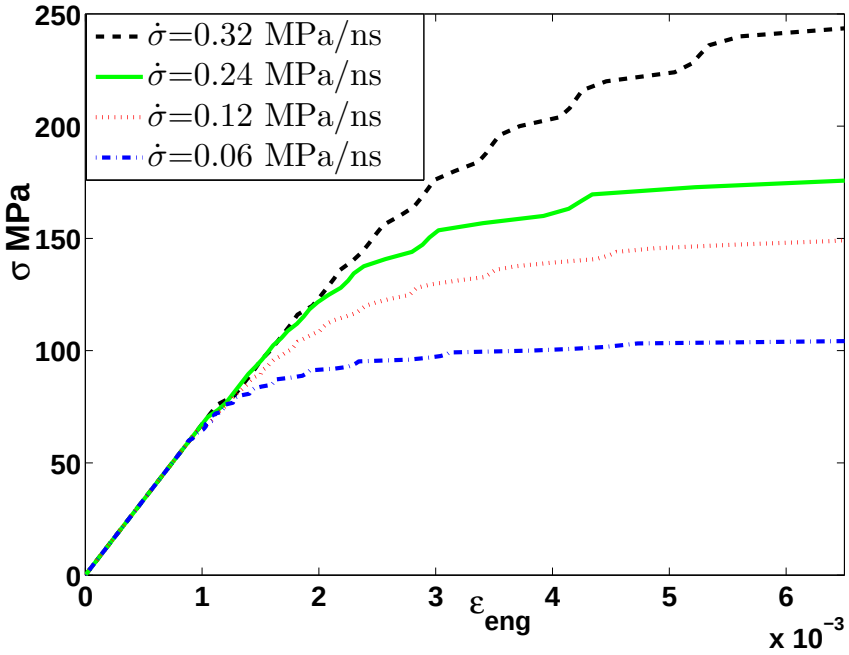

Figure 4.10: The stress-strain curve at the different loading rates without thermocoupling.

more, the heat equation should be incorporated into DD models to avoid overestimation of the stresses. The hardening of the material was observed due to temperature dependent dislocation drag. The simulations showed that the effect of temperature dependent drag increases with deformation rate. The softening effect was found to be stronger in the case of the adiabatic heating versus isothermal conditions on boundary of the domain. It was also observed that higher deformation rates resulted in both higher flow stresses and higher temperature rises. The proposed two–dimensional coupled thermomechanical discrete dislocation dynamics model provides a framework for further investigation of multiphysical phenomena of plastic deformation. It takes a first step in addressing concerns related to

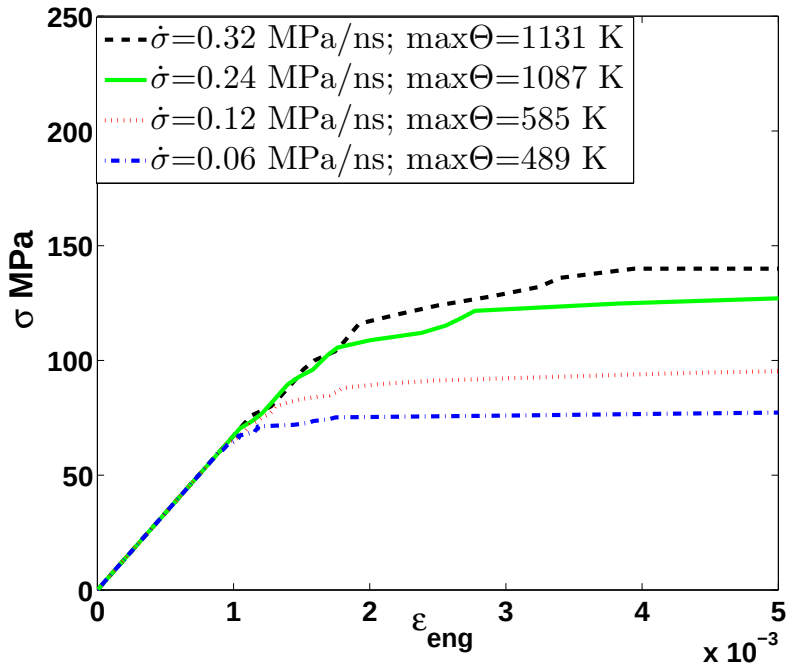

Figure 4.11: The stress-strain curve at the different loading rates.

the underestimation of thermal softening effects at high strain rates as well as the induced inter-play of temperature, dislocation drag, and hardening.

Chapter 5

Conclusions

Two new Discrete Dislocation Dynamics (DD) models that incorporate the effect of multiphysics were developed based on the eXtended Finite Element Method (XFEM). The discontinuities in the displacement field across the glide planes created by the dislocations were modeled by introducing additional basis functions into the approximation. The driving force on a dislocation, or Peach–Koehler force, in both models was calculated using the J-integral. The main contributions of this thesis are:

- ◇ The first fully coupled two-dimensional electromechanical (EM) Discrete Dislocation Dynamics model for the plastic deformation of anisotropic piezoelectric crystalline solids was developed.
    - The piezoelectric effect on the Peach–Koehler force is found to be significant and can affect both the direction and magnitude of the force. As a result, it was discovered that the piezoelectric effect is important when modeling the plastic

behavior of piezoelectric materials in the presence of electrical and mechanical fields.

- The simulations of the motion of many edge dislocations in a small domain demonstrated that, for piezoelectric materials, the plastic response of the material differs considerably when various electric potential differences are applied, illustrating that the physics of plasticity under electromechanical load is more complex than in purely mechanical systems.
- The developed EM–XFEM–DD model has great potential as a tool to study the behavior of the piezoelectric materials.

◇ The first two–dimensional fully coupled thermomechanical (TM) Discrete Dislocation Dynamics model for high strain rate plastic deformation of crystalline solids was developed.

- The TM–XFEM-DD model is able to simulate the heat generated by the motion of the dislocations under the high strain rate plastic deformation.
- The TM–XFEM–DD model takes the temperature dependency of dislocation drag into account. As a result, the simulations showed that the effect of temperature dependent drag increases with deformation rate.
- The softening effect predicted by TM–XFEM–DD is stronger in the case of adiabatic heating versus fixed temperature change on the boundary of the domain.

- The simulations showed that higher deformation rates resulted in both higher flow stresses and higher temperature rises.
- The developed TM–XFEM–DD is the first model to address concerns related to the underestimation of thermal softening effects at high strain rates at the mesoscale.

The thesis has qualitatively shown that when modeling plastic deformation of piezoelectric materials at the dislocation dynamics level, the coupling effects between electric and mechanical fields should be taken into account. The developed EM–XFEM–DD model is the first DD model that is able to account for such electromechanical coupling effects. I have also shown that when modeling the high strain rate plastic deformation of crystalline solids on dislocation dynamics level, the thermal effects can not be neglected. The performance of the crystalline solids under a high rate of strain is different than the performance under quasi-static conditions. The developed TM-XFEM-DD model is the first DD model which incorporates thermal effects, including heating induced by dislocation motion, and can be used to more effectively study the plastic behavior of metals under high strain rate deformation than the previous DD models.

To summarize, the goal of this thesis was achieved with the development of the EM–XFEM–DD and TM–XFEM–DD models. These new DD models bridge the gap between two scales, atomic- and micro-scale, by incorporating the effect of multiphysics, enabling the analysis of plastic phenomena in crystalline solids at the mesoscale, which was previously

not possible.

Chapter 6

Future work

In this chapter the recommendations are given regarding a future work for the extension of the developed fully coupled electromechanical (EM) and thermomechanical (TM) Discrete Dislocation Dynamics (DD) models, based on the eXtended Finite Element Method (XFEM):

- In the current calculations for both models, dislocation activity is only permitted on a single slip system. However, it is known that presence of another slip system can influence the dislocation evolution on the initial slip system [135, 139]. Such additional slip systems could be accounted for in the models to better represent the material behavior.
- The developed TM–XFEM–DD model assumes a constant critical resolved shear. In general, the critical resolved shear stress decreases with increases in temperature [119, 156]. In addition, the temperature dependence varies with the strain rate and

slip system [156, 157]. In the future, such data could be incorporated in the model in a straight-forward manner through a non-constant critical resolved shear stress.

- The TM–XFEM-DD model assumes that the thermal conductivity and specific heat of the material are constant. Given the large temperature changes observed in the simulations, the impact of this assumption should be revisited in order to ensure the accuracy of plastic material behavior analyses.

- The biggest limitation of the presented EM-XFEM-DD and TM-XFEM-DD models is that they are currently only implemented in two dimensions. Thus, the development of a three-dimensional EM-XFEM-DD and TM-XFEM-DD models is greatly desired.

Bibliography

[1] E. B. Tadmor and R. E. Miller. *Modeling materials: Continuum, Atomistic and Multiscale Techniques*. Cambridge University Press, 2011.

[2] E. Orowan. Theory of the fatigue of metals. *Proceedings of the Royal Society of London. Series A. Mathematical and Physical Sciences*, 171(944):79–106, 1939.

[3] S. Turteltaub. Time scales in plasticity: A few comments for a workshop discussion. Lorentz Center, 2009. Workshop discussion.

[4] E. Van der Giessen. Plasticity in the 21st century. In *Mechanics for a New Mellennium*, pages 413–428. Springer, 2002.

[5] E. Van der Giessen and A. Needleman. Discrete dislocation plasticity: a simple planar model. *Modelling and Simulation in Materials Science and Engineering*, 3(5):689–735, 1995.

[6] O. Kraft, LB Freund, R. Phillips, and E. Arzt. Dislocation plasticity in thin metal films. *MRS bulletin*, 27(1):30–37, 2002.

[7] J.L. Farvacque, J.C. Douehan, U. Von Alpen, and E. Gmelin. Screw-dislocation-induced scattering processes and acceptor states in te. *Physica Status Solidi (b)*, 79(2):763–773, 1977.

[8] K.A. Hartley, J. Duffy, and R.H. Hawley. Measurement of the temperature profile during shear band formation in steels deforming at high strain rates. *Journal of the Mechanics and Physics of Solids*, 35(3):283–301, 1987.

[9] S. N. Medyanik, W. K. Liu, and S. Li. On criteria for dynamic adiabatic shear band propagation. *Journal of the Mechanics and Physics of Solids*, 55(7):1439–1461, 2007.

[10] N. Ranc, L Taravella, V. Pina, and P. Herve. Temperature field measurement in titanium alloy during high strain rate loading adiabatic shear bands phenomenon. *Mechanics of Materials*, 40(4):255–270, 2008.

[11] G. R. Johnson and W. H. Cook. A constitutive model and data for metals subjected to large strains, high strain rates and high temperatures. In *Proceedings of the 7th International Symposium on Ballistics*, volume 21, pages 541–547. The Netherlands, 1983.

[12] J. R. Hook and H. E. Hall. *Solid State Physics (The Manchester Physics Series)*. John Wiley and Sons Ltd, 2000.

[13] G.I. Taylor. The mechanism of plastic deformation of crystals. Part II. Comparison with observations. *Proceedings of the Royal Society of London. Series A, Containing Papers of a Mathematical and Physical Character*, pages 388–404, 1934.

[14] M. Polanyi. Über eine art gitterstörung, die einen kristall plastisch machen könnte. *Zeitschrift für Physik A Hadrons and Nuclei*, 89(9–10):660–640, 1934.

[15] E. Orowan. Zur kristallplastizität. i: Tieftemperaturplastizität und beckersche formel. *Zeitschrift für Physik A Hadrons and Nuclei*, 89(9–10):605–613, 1934.

[16] E. Orowan. Zur kristallplastizität. ii: Die dynamische auffassung der kristallplastizität. *Zeitschrift für Physik A Hadrons and Nuclei*, 89(9–10):614–633, 1934.

[17] E. Orowan. Zur kristallplastizität. iii: Über den mechanismus des gleitvorganges. *Zeitschrift für Physik A Hadrons and Nuclei*, 89(9–10):634–659, 1934.

[18] C. R. Weinberger and W. Cai. Surface-controlled dislocation multiplication in metal micropillars. *Proceedings of the National Academy of Sciences*, 105(38):14304–14307, 2008.

[19] J. Lothe J.P. Hirth. *Theory of Dislocations*. McGraw-hill,Inc, 1968.

[20] H. Kuhlmann-Wilsdorf and G.F. Wilsdorf. Dislocation movements in metals. *Science*, pages 17–25., 1964.

[21] L.D. Landau and E.M. Lifshitz. *Theory of Elasticity*. Butterworth-Heinemann, Oxford, 3 edition, 1986.

[22] D. Hull and D.J. Bacon. *Introduction to Dislocations*. Butterworth-Heinemann, Oxford, 4 edition, 2001.

[23] R.W. Lardner. *Mathematical Theory of Dislocations and Fracture*. University of Toronto Press, Toronto and Buffalo, 1974.

[24] J. Weertman and J.R. Weertman. *Elementary Dislocation Theory*. Oxford University Press, New York, 1992.

[25] M. Jessell, P. Bons, and P. Rey. *Microstructures*. Online, 2011.

[26] R. Abbaschian and R. Reed-Hill. *Physical metallurgy principles*. Cengage Learning, 2008.

[27] J. Frenkel. Zur theorie der elastizitätsgrenze und der festigkeit kristallinischer körper. *Zeitschrift für Physik A Hadrons and Nuclei*, 37(7–8):572–609, 1926.

[28] A. Powell. Deformation by dislocations: Dislocation glide. MIT OpenCourseWare, 2005.

[29] W.T. Read F.C. Frank. Symposium on Plastic Deformation of Crystalline Solids. Carnegie Institute of Technology, 1950. Pittsburgh, PA.

[30] M. Peach and J.S. Koehler. The forces exerted on dislocations and the stress fields produced by them. *Physical Review*, 80(3):436, 1950.

[31] G. A. Maugin. Material forces: Concepts and applications. *Applied Mechanics Reviews*, 48(5):213–245, 1995.

[32] J.D. Eshelby. The force on an elastic singularity. *Philosophical Transactions of the Royal Society of London. Series A, Mathematical and Physical Sciences*, 244(877):87, 1951.

[33] G. P. Cherepanov. Crack propagation in continuous media. *Journal of Applied Mathematics and Mechanics*, 31(3):503–512, 1967.

[34] J. Rice. A path independent integral and the approximate analysis of strain concentration by notches and cracks. *Journal of applied mechanics*, 35(2):379–386, 1968.

[35] V. Volterra. Sur lequilibre des corps elastiques multiplement connexes. *Annales scientifiques de l'cole normale suprieure*, 3(24):401–517, 1907.

[36] F.R.N. Nabarro. *Theory of Crystal Dislocations*. Clarendon, Oxford, 3 edition, 1967.

[37] V.V. Bulatov and W. Cai. *Computer Simulation of Dislocations*. Oxford University Press, 2006.

[38] V. Vitek. *Handbook of Materials Modeling*, volume II, chapter Dislocation Cores and Unconventional Properties of Plastic Behavior, pages 2883–2896. Springer,2005, 1992.

[39] V. V. Bulatov and E. Kaxiras. Semi-discrete variational peierls framework for dislocation core properties. *Phys. Rev. Lett.*, 78:4221, 1997.

[40] F.R.N. Nabarro. Dislocations in a simple cubic lattice. *Proceedings of the Physical Society*, 59(2):256, 1947.

[41] R. Peierls. The size of a dislocation. *Proceedings of the Physical Society*, 52(1):34, 1940.

[42] V. Vitek, L. Lejček, and D.K. Bowen. On the factors controlling the structure of dislocation cores in BCC crystals. In *Interatomic Potentials and Simulation of Lattice Defects*, pages 493–508. Springer, 1972.

[43] V. Vitek. Intrinsic stacking faults in body-centred cubic crystals. *Philosophical Magazine*, 18(154):773–786, 1968.

[44] W. Ngan. A generalized Peierls-Nabarro model for non-planar screw dislocation cores. *Mech. Phys. Solids*, 45(6):903–921, 1997.

[45] M.S. Duesbery E. Kaxiras. Free–energies of generalized stacking faults in Si and implications for the brittle-ductile transition. *Phys. Rev. Lett.*, 70:3752, 1993.

[46] N.I. Medvedeva, O.N. Mryasov, Y. N. Gornostyrev, D.L. Novikov, and A.J. Freeman. First-principles total-energy calculations for planar shear and cleavage decohesion processes in b2-ordered nial and feal. *Physical Review B*, 54(19):13506, 1996.

[47] M. Koning, W. Cai, and V.V. Bulatov. Anomalous dislocation multiplication in FCC metals. *Phys Rev Letter*, 91(2), 2003.

[48] G. Lu, N. Kioussis, V. V. Bulatov, and E. Kaxiras. Generalized-stacking-fault energy surface and dislocation properties of aluminum. *Physical Review B*, 62(5):3099, 2000.

[49] A. Metsue, P. Carrez, C. Denoual, D. Mainprice, and P. Cordier. Peierls–Nabarro modelling of dislocations in diopside. *Physics and Chemistry of Minerals*, 37(10):711–720, 2010.

[50] G. Schöeck. The core energy of dislocations. *Acta Metallurgica et Materialia*, 43(10):3679–3684, 1995.

[51] J.D. Eshelby. Edge dislocations in anisotropic materials. *Phil. Mag*, 40:903–912, 1949.

[52] G. Schöeck A. Seeger. Die aufspaltung von versetzungen in metallen dichtester kugelpackung / the splitting of dislocations in metals with close-packed lattices. *Acta Metallurgica*, 1(5):519–530, 1953.

[53] R.J. Amodeo and N.M. Ghoniem. Dislocation dynamics. I. A proposed methodology for deformation micromechanics. *Physical Review B*, 41(10):6958, 1990.

[54] A.N. Gulluoglu and C.S. Hartley. Simulation of dislocation microstructures in two dimensions. I. Relaxed structures. *Modelling and Simulation in Materials Science and Engineering*, 1:1, 1992.

[55] B. Devincre, L.P. Kubin, C. Lemarchand, and R. Madec. Mesoscopic simulations of plastic deformation. *Materials Science and Engineering: A*, 309:211–219, 2001.

[56] V. V. Bulatov. Current developments and trends in dislocation dynamics. *Journal of computer-aided materials design*, 9(2):133–144, 2002.

[57] N. Ahmed and A. Hartmaier. A two-dimensional dislocation dynamics model of the plastic deformation of polycrystalline metals. *Journal of the Mechanics and Physics of Solids*, 58(12):2054–2064, 2010.

[58] S. Puri, A. Das, and A. Acharya. Mechanical response of multicrystalline thin films in mesoscale field dislocation mechanics. *Journal of the Mechanics and Physics of Solids*, 59:2000–2017, 2011.

[59] Y. Xiang. Modeling dislocations at different scales. *Communications in Computational Physics*, 1(3):383–424, 2006.

[60] H. M. Zbib, M. Rhee, and J. P. Hirth. On plastic deformation and the dynamics of 3D dislocations. *International Journal of Mechanical Sciences*, 40(2):113–127, 1998.

[61] V. Pontikis, Y. Bréchet, G.R. Canova, B. Devincre, M. Condat, and L.B. Kubin. 3D simulation of dislocation motion on a lattice: Application to the yield surface of single crystals. *Solid State Phenomena*, 35:101–106, 1993.

[62] E. Van der Giessen D. Weygand, L.H. Friedman and A. Needleman. Discrete dislocation modelling in three dimensional confined volumes. *Materials Science and Engineering*, A309-310:420–424, 2001.

[63] A. Needleman and E. Van der Giessen. Discrete dislocation and continuum descriptions of plastic flow. *Materials Science and Engineering*, A309-310:1–13, 2001.

[64] K.W. Schwarz. Simulations of dislocations on mesoscopic scale. I. Methods and examples. *Journal of Applied Physics*, 85(1):108–119, 1999.

[65] K.W. Schwarz. Simulation of dislocations on the mesoscopic scale. II. Application to strained-layer relaxation. *Journal of Applied Physics*, 85(1):120–129, 1999.

[66] Y. U. Wang, Y.M. Jin, A.M. Cuitino, and A.G. Khachaturyan. Nanoscale phase field microelasticity theory of dislocations: Model and 3D simulations. *Acta Materialia*, 49(10):1847–1857, 2001.

[67] Y. Xiang, L. Cheng, D. J. Srolovitz, and Weinan E. A level set method for dislocation dynamics. *Acta Materialia*, 51(18):5499–5518, 2003.

[68] R. Fedkiw and S. Osher. Level set methods and dynamic implicit surfaces. *Surfaces*, 44:77, 2002.

[69] J. A. Sethian. *Level set methods and fast marching methods: Evolving interfaces in computational geometry, fluid mechanics, computer vision, and materials science*, volume 3. Cambridge university press, 1999.

[70] L.P. Kubin C. Lemarchand, B. Devincre. Homogenization method for a discrete-continuum simulation of dislocation dynamics. *Journal of the Mechanics and Physics of Solids*, 49(9):19691982, 2001.

[71] N. Ghoniem X. Han. Stress field and interaction forces of dislocations in anisotropic multilayer thin films. *Philosophical Magazine*, 85(11):12051225, 2005.

[72] N. Ghoniem X. Han. Dislocation motion in anisotropic multilayer materials. *Philosophical Magazine*, 85(24):2809–2830, 2005.

[73] Z. Wang X. Han, N. M. Ghoniem. Parametric dislocation dynamics of anisotropic crystals. *Philosophical Magazine*, 83:31–34, 2004.

[74] M. Rhee, J. S. Stolken, V. V. Bulatov, T. D. de la Rubia, H. M. Zbib, and J. P. Hirth. Dislocation stress fields for dynamic codes using anisotropic elasticity: Methodology and analysis. *Materials Science and Engineering: A*, 309:288–293, 2001.

[75] R. Gracie, G. Ventura, and T. Belytschko. A new fast finite element method for dislocations based on interior discontinuities. *International Journal for Numerical Methods in Engineering*, 69(2):423–441, 2007.

[76] T. Belytschko and T. Black. Elastic crack growth in finite elements with minimal remeshing. *International Journal for Numerical Methods in Engineering*, 45(5):601–620, 1999.

[77] T. Belytschko, N. Moës, S. Usui, and C. Parimi. Arbitrary discontinuities in finite elements. *International Journal for Numerical Methods in Engineering*, 50(4):993–1013, 2001.

[78] T.-P. Fries and T. Belytschko. The extended/generalized finite element method: An overview of the method and its applications. *International Journal for Numerical Methods in Engineering*, 84(3):253–304, 2010.

[79] N. Moës, J. Dolbow, and T. Belytschko. A finite element method for crack growth without remeshing. *International Journal for Numerical Methods in Engineering*, 46:131–150, 1999.

[80] N. Moës and T. Belytschko. Extended finite element method for cohesive crack growth. *Engineering fracture mechanics*, 69(7):813–833, 2002.

[81] N. Sukumar, D. L. Chopp, N. Moës, and T. Belytschko. Modeling holes and inclusions by level sets in the extended finite-element method. *Computer methods in applied mechanics and engineering*, 190(46):6183–6200, 2001.

[82] A. Zilian and A. Legay. The enriched space–time finite element method (EST) for simultaneous solution of fluid–structure interaction. *International Journal for Numerical Methods in Engineering*, 75(3):305–334, 2008.

[83] J. Chessa and T. Belytschko. An extended finite element method for two-phase fluids. *Journal of Applied Mechanics*, 70(1):10–17, 2003.

[84] R. Gracie, J. Oswald, and T. Belytschko. On a new extended finite element method for dislocations: Core enrichment and nonlinear formulation. *Journal of the Mechanics and Physics of Solids*, 56(1):200–214, 2008.

[85] J. Oswald, R. Gracie, R. Khare, and T. Belytschko. An extended finite element method for dislocations in complex geometries: Thin films and nanotubes. *Computer Methods in Applied Mechanics and Engineering*, 198(21):1872–1886, 2009.

[86] T. Belytschko and R. Gracie. On XFEM applications to dislocations and interfaces. *International Journal of Plasticity*, 23(10-11):1721–1738, 2007.

[87] T. Belytschko, R. Gracie, and G. Ventura. A review of extended/generalized finite element methods for material modeling. *Modelling and Simulation in Materials Science and Engineering*, 17:043001, 2009.

[88] G. Ventura, B. Moran, and T. Belytschko. Dislocations by partition of unity. *International Journal for Numerical Methods in Engineering*, 62(11):1463–1487, 2005.

[89] J. M. Melenk and I. Babuška. The partition of unity finite element method: Basic theory and applications. *Computer methods in applied mechanics and engineering*, 139(1):289–314, 1996.

[90] J. Chessa, H. Wang, and T. Belytschko. On the construction of blending elements for local partition of unity enriched finite elements. *International Journal for Numerical Methods in Engineering*, 57(7):1015–1038, 2003.

[91] T.-P. Fries. A corrected XFEM approximation without problems in blending elements. *International Journal for Numerical Methods in Engineering*, 75(5):503–532, 2008.

[92] R. Gracie, H. Wang, and T. Belytschko. Blending in the extended finite element method by discontinuous Galerkin and assumed strain methods. *International Journal for Numerical Methods in Engineering*, 74(11):1645–1669, 2008.

[93] G. Ventura, R. Gracie, and T. Belytschko. Fast integration and weight function blending in the extended finite element method. *International Journal for Numerical Methods in Engineering*, 77(1):1–29, 2009.

[94] T. Strouboulis, K. Copps, and I. Babuška. The generalized finite element method: An example of its implementation and illustration of its performance. *International Journal for Numerical Methods in Engineering*, 47(8):1401–1417, 2000.

[95] T. Strouboulis, I. Babuška, and K. Copps. The design and analysis of the generalized finite element method. *Computer methods in applied mechanics and engineering*, 181(1):43–69, 2000.

[96] W. G. Cady. *Piezoelectricity*. McGraw-Hill, 1946.

[97] A. Pinin. Perovskite structure of pzt. Online, 2010.

[98] D. Supratik. Piezoelectric materials: Crystal orientation and poling direction. COMSOL, Online, 2014.

[99] H. Conrad, Z. Guo, and A.F. Sprecher. Effect of an electric field on the recovery and recrystallization of Al and Cu. *Scripta metallurgica*, 23(6):821–823, 1989.

[100] N. Karam H. Conrad and S. Mannan. Electroelastic fields of moving dislocations and disclinations in piezoelectric crystals. *Scripta Met.*, 18:275, 1984.

[101] H. Conrad, W.D. Cao, X.P. Lu, and A.F. Sprecher. Effect of an electric field on the superplasticity of 7475 Al. *Scripta metallurgica*, 23(5):697–702, 1989.

[102] L. Merten. Modell einer schraubenversetzung in piezoelektrischen kristallen. i allgemeine theorie elektrisches feld bei ladungsfreiheit ladungsverteilung bei feldfreiheit. *Zeitschrift für Physik B Condensed Matter*, 2(1):53–65, 1964.

[103] D. M. Barnett and J. Lothe. Dislocations and line charges in anisotropic piezoelectric insulators. *Physica Status Solidi (b)*, 67:105–111, 1975.

[104] S. Minagawa. Mechanical, electrical, and thermal fields produced by moving dislocations and disclinations in thermo-piezoelectric continua. *Physica Status Solidi (b)*, 124(2):565–571, 1984.

[105] S. K. Khannanov. Electroelastic fields of moving dislocations and disclinations in piezoelectric crystals. *Physics of the Solid State*, 41(1102), 1999.

[106] A. K. Soh, J. Liu, K. L. Lee, and D. Fang. Moving dislocations in general anisotropic piezoelectric solids. *Physica Status Solidi (b)*, 242(4):842–853, 2005.

[107] K. Shintani and S. Minagawa. Dislocation dynamics in anisotropic piezoelectric crystals. III. Elliptical dislocation loop. *Philosophical Magazine A*, 62(3):275–282, 1990.

[108] Y. Y. Tang and K. Xu. Exact solutions of piezoelectric materials with moving screw and edge dislocations. *International Journal of Engineering Science*, 32(10):1579–1591, 1994.

[109] M. Tang and J. Marian. Temperature and high strain rate dependence of tensile deformation behavior in single-crystal iron from dislocation dynamics simulations. *Acta Materialia*, 70:123–129, 2014.

[110] A. Eisenlohr, I. Gutierrez-Urrutia, and D. Raabe. Adiabatic temperature increase associated with deformation twinning and dislocation plasticity. *Acta Materialia*, 60(9):3994–4004, 2012.

[111] N. Ghoniem, S.-H. Tong, and L.Z. Sun. Parametric dislocation dynamics: A thermodynamics-based approach to investigations of mesoscopic plastic deformation. *Physical Review B*, 61(2):913, 2000.

[112] R. Kapoor and S. Nemat-Nasser. Determination of temperature rise during high strain rate deformation. *Mechanics of Materials*, 27(1):1–12, 1998.

[113] T. Belytschko, B. Moran, and M. Kulkarni. On the crucial role of imperfections in quasi-static viscoplastic solutions. *Journal of Applied Mechanics*, 58(3):658–665, 1991.

[114] M. Zhou, G. Ravichandran, and A.J. Rosakis. Dynamically propagating shear bands in impact-loaded prenotched platesii. numerical simulations. *Journal of the Mechanics and Physics of Solids*, 44(6):1007–1032, 1996.

[115] P. Rosakis, A.J. Rosakis, G. Ravichandran, and J. Hodowany. A thermodynamic internal variable model for the partition of plastic work into heat and stored energy in metals. *Journal of the Mechanics and Physics of Solids*, 48(3):581–607, 2000.

[116] G. Po and N. Ghoniem. A variational formulation of constrained dislocation dynamics coupled with heat and vacancy diffusion. *Journal of the Mechanics and Physics of Solids*, 66:103–116, 2014.

[117] M. Tang, B. Devincre, and L.P. Kubin. Simulation and modelling of forest hardening in body centre cubic crystals at low temperature. *Modelling and Simulation in Materials Science and Engineering*, 7(5):893, 1999.

[118] S. Naamane, G. Monnet, and B. Devincre. Low temperature deformation in iron studied with dislocation dynamics simulations. *International Journal of Plasticity*, 26(1):84–92, 2010.

[119] C.N. Beyerlein, I.J .and Tomé. A dislocation-based constitutive law for pure zr including temperature effects. *International Journal of Plasticity*, 24(5):867–895, 2008.

[120] K. M. Jassby and T. Vreeland Jr. An experimental study of the mobility of edge dislocations in pure copper single crystals. *Philosophical Magazine*, 21(174):1147–1168, 1970.

[121] U.F. Kocks, A.S. Argon, and M.F. Ashby. Progress in materials science. *Pergamon Press: Oxford*, 19:1–129, 1975.

[122] D. Klahn, A.K. Mukherjee, and J.E. Dorn. Proceedings of the second international conference on the strength of metals and alloys. *Journal of Composite Materials*, 1970.

[123] F.J. Zerilli and R.W. Armstrong. The effect of dislocation drag on the stress-strain behavior of fcc metals. *Acta Metallurgica et Materialia*, 40(8):1803–1808, 1992.

[124] O. Skiba, R. Gracie, and S. Potapenko. Electromechanical simulations of dislocations. *Modelling and Simulation in Materials Science and Engineering*, 21(3):035003, 2013.

[125] B.G. Galerkin. On electrical circuits for the approximate solution of the laplace equation. *Vestnik Inzhenerov (In Russian)*, 19:897908, 1915.

[126] I. Babuška. The finite element method with Lagrangian multipliers. *Numerische Mathematik*, 20(3):179–192, 1973.

[127] D.R. Curran D.A. Berlincourt and H.Jaffe. *Physical Acoustics*, volume 1Part A, chapter Piezoelectric and Piezomagnetic Materials and Their Function in Transducers, pages 169–270. Academic Press, New York, 1964.

[128] R. Rajapakse. Closed-form solutions for edge dislocations in piezoelectric solids. *Mechanics of Advanced Materials and Structures*, 6(2):97–115, 1999.

[129] G. Herrmann Y.E. Pak. Conservation laws and the material momentum tensor for the elastic dielectric. *International Journal of Engineering Science*, 24(8):1365–1374, 1986.

[130] J. Dundurs and G.P. Sendeckyj. Behavior of an edge dislocation near a bimetallic interface. *Journal of Applied Physics*, 36:3353, 1965.

[131] M. C. Ehmke, F. H. Schader, K. G. Webber, J. Rödel, J. E. Blendell, and K. J. Bowman. Stress, temperature and electric field effects in the lead-free (Ba, Ca)(Ti, Zr) O3 piezoelectric system. *Acta Materialia*, 78:37–45, 2014.

[132] H. Conrad. Some effects of an electric field on the plastic deformation of metals and ceramics. *Materials Research Innovations*, 2(1):1–8, 1998.

[133] D.S. Balint, V.S. Deshpande, A. Needleman, and E. Van der Giessen. Size effects in uniaxial deformation of single and polycrystals: A discrete dislocation plasticity analysis. *Modelling and Simulation in Materials Science and Engineering*, 14:409, 2006.

[134] E. Dieulesaint and D.J. Royer. *Elastic waves in solids*. Springer, 1980.

[135] V.S. Deshpande, A. Needleman, and E. Van der Giessen. Plasticity size effects in tension and compression of single crystals. *Journal of the Mechanics and Physics of Solids*, 53(12):2661–2691, 2005.

[136] M. Conti and G. Corda. Influence of slip plane dislocations on electrical perfomances of n-p-n planar transistors. *IEEE Transactions on electron Dvices*, 18(12):1148–1150, 1971.

[137] S.S. Shishvan and E. Van der Giessen. Distribution of dislocation source length and the size dependent yield strength in freestanding thin films. *Journal of the Mechanics and Physics of Solids*, 58(5):678–695, 2010.

[138] L.B. Zuev, V.E. Gromov, and L.I. Gurevich. The effect of electric current pulses on the dislocation mobility in zinc single crystals. *Physica Status Solidi (a)*, 121(2):437–443, 1990.

[139] M.D. Uchic, D.M. Dimiduk, J.N. Florando, and W.D. Nix. Sample dimensions influence strength and crystal plasticity. *Science*, 305(5686):986, 2004.

[140] T. Belytschko, N. Moës, S. Usui, and C. Parimi. Arbitrary discontinuities in finite elements. *International Journal for Numerical Methods in Engineering*, 50(4):993–1013, 2001.

[141] R. Gracie, G. Ventura, and T. Belytschko. A new fast finite element method for dislocations based on interior discontinuities. *International Journal for Numerical Methods in Engineering*, 69(2):423–441, 2007.

[142] R. Gracie and T. Belytschko. Concurrently coupled atomistic and XFEM models for dislocations and cracks. *International Journal for Numerical Methods in Engineering*, 78(3):354–378, 2009.

[143] J. Crank and P. Nicolson. A practical method for numerical evaluation of solutions of partial differential equations of the heat-conduction type. In *Mathematical Proceedings of the Cambridge Philosophical Society*, volume 43, pages 50–67. Cambridge Univ Press, 1947.

[144] T. Jr. Hughes. Unconditionally stable algorithms for nonlinear heat conduction. *Computer Methods in Applied Mechanics and Engineering*, 10(2):135–139, 1977.

[145] K. Kishimoto, S. Aoki, and M. Sakata. On the path independent integral-j. *Engineering Fracture Mechanics*, 13(4):841–850, 1980.

[146] L. Kubin. *Dislocations, mesoscale simulations and plastic flow*, volume 5. Oxford University Press, 2013.

[147] G. Regazzoni, U.F. Kocks, and P.S. Follansbee. Dislocation kinetics at high strain rates. *Acta metallurgica*, 35(12):2865–2875, 1987.

[148] A. Kumar, F.E. Hauser, and J.E. Dorn. Viscous drag on dislocations in aluminum at high strain rates. *Acta Metallurgica*, 16(9):1189–1197, 1968.

[149] A. Needleman and V. Tvergaard. Analysis of a brittle-ductile transition under dynamic shear loading. *International Journal of Solids and Structures*, 32(17-18):2571–2590, 1995.

[150] R. Kapoor and S. Nemat-Nasser. Determination of temperature rise during high strain rate deformation. *Mechanics of Materials*, 27(1):1–12, 1998.

[151] J.S. Langer, E. Bouchbinder, and T. Lookman. Thermodynamic theory of dislocation-mediated plasticity. *Acta Materialia*, 58(10):3718–3732, 2010.

[152] P.S. Follansbee, G. Regazzoni, and U.F. Kocks. High-strain-rate measurements of dislocation mobility. *The Mechanics of Dislocations, American Society for Metals, Metals Park, OH*, 237, 1985.

[153] Y. Li, Y. Zhang, N. Tao, and K. Lu. Effect of the zener–hollomon parameter on the microstructures and mechanical properties of cu subjected to plastic deformation. *Acta Materialia*, 57(3):761–772, 2009.

[154] U. Andrade, M.A. Meyers, K.S. Vecchio, and A. H. Chokshi. Dynamic recrystallization in high-strain, high-strain-rate plastic deformation of copper. *Acta metallurgica et materialia*, 42(9):3183–3195, 1994.

[155] I. Ryu, W. D. Nix, and W. Cai. Plasticity of bcc micropillars controlled by competition between dislocation multiplication and depletion. *Acta Materialia*, 61(9):3233–3241, 2013.

[156] G. Monnet, L. Vincent, and B. Devincre. Dislocation-dynamics based crystal plasticity law for the low-and high-temperature deformation regimes of bcc crystal. *Acta Materialia*, 61(16):6178–6190, 2013.

[157] H. Zhou, L. Zhang, and S. Qu. Temperature effect on critical shear stress for twin boundary migration. *Computational Materials Science*, 60:231–233, 2012.